

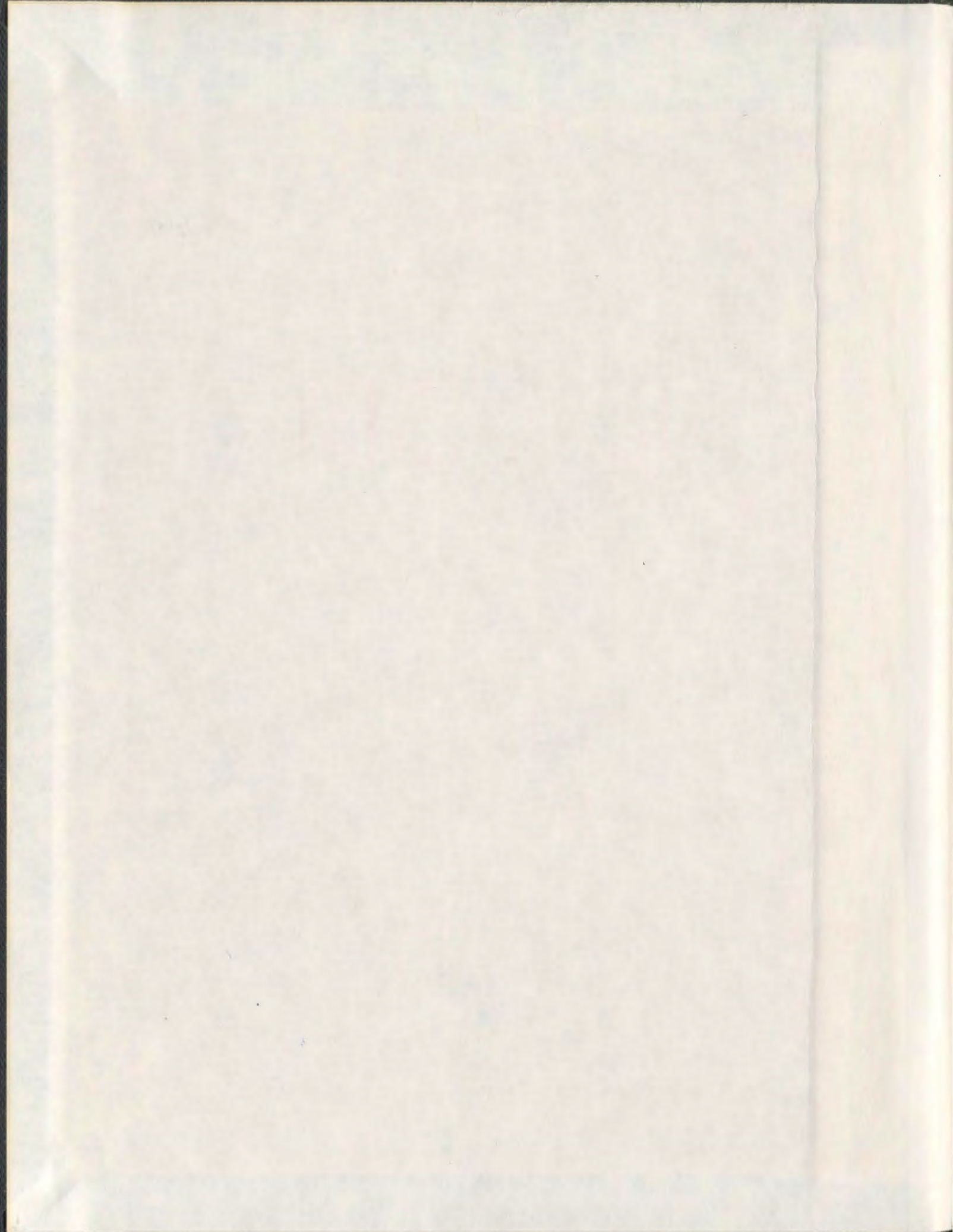
**BRILLOUIN SCATTERING STUDIES OF ROTATION-TRANSLATION
COUPLING EFFECTS IN SOME SIMPLE MOLECULAR CRYSTALS**

CENTRE FOR NEWFOUNDLAND STUDIES

**TOTAL OF 10 PAGES ONLY
MAY BE XEROXED**

(Without Author's Permission)

VAHID ASKARPOUR, B.Sc.(Hons), M.Sc.



**Brillouin Scattering Studies of
Rotation-Translation Coupling Effects in Some
Simple Molecular Crystals**

by

Vahid Askarpour, B. Sc. (Hons), M. Sc.

A thesis submitted to the School of Graduate
Studies in partial fulfillment of the
requirements for the degree of
Doctor of Philosophy

Department of Physics
Memorial University of Newfoundland
April, 1991

St. John's

Newfoundland

Abstract

The role of rotation-translation (RT) coupling was studied in large single crystals of α -carbon monoxide, γ -oxygen, cyclooctane I and methane I by observing the behaviour of acoustic phonons as a function of temperature particularly as the order-disorder phase transition is approached. To this end the adiabatic elastic constants were determined by the technique of high resolution Brillouin spectroscopy.

Large single crystals of α -carbon monoxide, γ -oxygen, methane I and cyclooctane I were grown and cooled in a low temperature cryostat. The quality of the crystals and the orientation of their crystal axes were determined by analyzing x-ray Laue diffraction photographs. Laser light of 5145 Å was incident along the axis of the cell and the scattered light was analyzed at 90° by a Brillouin spectrometer.

The adiabatic elastic constants of α -CO at 60.9 K were determined. RT coupling appeared not to be significant in the $q = 0$ wavevector regime and the α -CO crystals effectively behaved like a rare gas solid in this regime. The orientations of the fcc and hcp phases were correlated.

The adiabatic elastic constants of γ -O₂ were determined at 49.0 K, 46.5 K, 45.6 K and 44.0 K. The spectrum, close to the triple point temperature, exhibited unusually strong elastic isotropy and transverse component intensity. Cyclooctane I was studied for comparison to γ -oxygen since it had the same structure and RT coupling was known to be strong in this solid. The Brillouin spectra were recorded at 284.2 K, 274.2 K, 254.2 K, 234.2 K and 224.2 K. Cyclooctane I was also very isotropic and only

one transverse component was ever observed for all the orientations and temperatures studied in this experiment. It was therefore concluded that the unusual features in the Brillouin spectra of γ -oxygen and cyclooctane I are caused by strong RT coupling in their peculiar structure.

The elastic constants of methane I single crystals were determined at 72.8 K, 50.9 K, 38.5 K and 25.0 K. It was noted that RT coupling effects become less significant as the rotational ordering is approached and methane I behaves like a rare gas solid at temperatures below 70 K. Reduction in the value of C_{12} was observed at 25.0 K which appeared to indicate the onset of the phase transition.

Acknowledgements

I wish to express my sincere appreciation and lasting gratitude to my supervisors Dr. H. Kiefte and Dr. M. J. Clouter for their constant support and guidance throughout this project. I would like to further thank Dr. H. Kiefte for several reviewings of this thesis in a short period of time. I am thankful to Dr. J. Zuk for his collaboration on cyclooctane studies, and to Mr. R. Kelly for his assistance with methane studies.

I am grateful to Mr. R. Bradley for making prints of several photographs, to Mr. R. Guest for careful drafting of several figures, to Mr. W. Holley for providing a continuous supply of cryogenic liquids and to Mr. T. Andrews for orienting a single crystal of β - O_2 . I would like to thank my friends Dr. R. J. J. Goulding and Mr. H. Luo for their helpful discussions.

In the past three years I was supported by Natural Sciences and Engineering Research of Canada Scholarship and Memorial University Fellowship which I gratefully acknowledge.

Contents

Abstract	ii
Acknowledgements	iv
Table of Contents	v
List of Figures	ix
List of Tables	x
1 Introduction	1
1.1 Plastic crystals and order-disorder phase transitions	1
1.2 Rotation-translation coupling: literature review	3
2 Systems under investigation	17
2.1 Introduction	17
2.2 Carbon monoxide	18
2.3 Oxygen	22
2.4 Cyclooctane	27

2.5	Methane	28
3	Background theory	32
3.1	Stress, strain and elastic constants	32
3.2	Propagation of elastic waves in cubic crystals	34
3.3	Rotation-translation coupling	39
3.4	Euler angles	43
4	Experimental arrangements and procedure	45
4.1	Experimental setup	45
4.2	Laser	45
4.3	The Brillouin spectrometer	46
4.3.1	Fabry-Perot interferometer	46
4.3.2	Data aquisition and stabilization system	48
4.3.3	Optical setup and alignment	50
4.4	Cryostat, cell and temperature control	54
4.4.1	Liquid helium cryostat	55
4.4.2	Thermoelectric cryostat	61
4.5	Single crystal growth and cooling	66
4.6	X-ray crystal orientation procedure	68
4.7	Analysis of the Brillouin spectrum	71
4.8	Determination of the elastic constants	74
4.9	Application of magnetic field	75

5	Experimental results	77
5.1	Results for α -carbon monoxide	77
5.1.1	The Brillouin spectrum of α -CO	77
5.1.2	Elastic constants of α -CO	78
5.1.3	α - β phase transition in CO	80
5.2	Results for γ -oxygen	85
5.2.1	The Brillouin spectrum of γ -O ₂	85
5.2.2	Elastic constants of γ -O ₂	87
5.2.3	Magnetic field results	94
5.2.4	γ - β phase transition in O ₂	97
5.3	Results for cyclooctane I	100
5.3.1	Brillouin spectrum of cyclooctane I	100
5.3.2	Elastic constants of cyclooctane I	101
5.4	Results for methane I	111
5.4.1	Brillouin spectrum of methane I	111
5.4.2	Elastic constants of methane I	113
6	Discussion	123
6.1	α -carbon monoxide	123
6.2	Comparison of γ -oxygen and cyclooctane I	126
6.3	Methane I	134
6.4	Concluding remarks	138

List of Figures

2.1	Phase diagrams of solid solutions with various components	2
2.2	Phase diagrams of pure Q_2	11
2.3	Diagram of $Q_2 - Q_1$	16
3.1	The crystal structure of Q_2	22
4.2	The top and the tail bands of the spectrum	34
4.3	The crystal cell	34
4.4	Crystal and the cell structure	35
5.5	Diagram of the Raman spectrum	42
6.1	Low diffraction pattern of the Q_2 phase of arsenic	50
6.2	Low diffraction pattern of the Q_1 phase of arsenic	50
6.3	The Σ point structure of Q_2 at 100°C	50
6.4	Temperature dependence of the Raman spectrum of Q_2	50
6.5	Low diffraction photograph of the Q_2 phase of Q_2	50
6.6	Temperature dependence of the Raman spectrum of arsenic	50
6.7	The Raman spectrum of arsenic at 273°K	112
6.8	Temperature dependence of the Raman spectrum of arsenic	122

List of Figures

2.1	Phase diagrams of solid nitrogen and carbon monoxide.	19
2.2	Phase diagram of solid O_2	23
2.3	Structure of $\gamma-O_2$	24
4.1	The optical arrangement	52
4.2	The top and the tail section of the cryostat	58
4.3	The sample cell	59
4.4	Cryostat and the cell assembly	63
4.5	Stick-diagram of the Brillouin spectrum.	72
5.1	Laue diffraction pattern of the β phase of crystal I.	82
5.2	Laue diffraction pattern of the α phase of crystal I.	83
5.3	The Brillouin spectrum of $\gamma-O_2$ at 44.0 K.	86
5.4	Temperature dependence of the elastic constants of $\gamma-O_2$	96
5.5	Laue diffraction photograph of the beta phase of O_2	99
5.6	Temperature dependence of elastic constants of cyclooctane I	110
5.7	The Brillouin spectrum of methane I at 25.0 K.	112
5.8	Temperature dependence of the elastic constants of methane I	122

List of Tables

1.1	Ratios of acoustic velocities in high symmetry directions of several cubic crystals close to their triple point temperatures.	12
2.1	Ratio of acoustic velocities in β - N_2 , β - CO and $Ar_{94\%}(O_2)_{6\%}$ near their respective triple points	20
5.1	Brillouin scattering data for single crystals of α - CO at 60.9 K.	79
5.2	Brillouin scattering data for single crystals of γ - O_2 at 49.0 K.	88
5.3	Brillouin scattering data for single crystals of γ - O_2 at 46.5 K.	89
5.4	Brillouin scattering data for single crystals of γ - O_2 at 45.6 K.	90
5.5	Brillouin scattering data for single crystals of γ - O_2 at 44.0 K.	91
5.6	Temperature dependent data for γ - O_2	95
5.7	Elasto-optic ratios and constants for γ - O_2	95
5.8	Brillouin scattering data for single crystals of cyclooctane I at 284.2 K.	102
5.9	Brillouin scattering data for single crystals of cyclooctane I at 274.2 K.	104
5.10	Brillouin scattering data for single crystals of cyclooctane I at 254.2 K.	105
5.11	Brillouin scattering data for single crystals of cyclooctane I at 234.2 K.	106
5.12	Brillouin scattering data for single crystals of cyclooctane I at 224.2 K.	107

5.13	Temperature dependent data for cyclooctane I single crystals	109
5.14	Temperature dependent data for Pockel's ratios and coefficients for cyclooctane I single crystals	109
5.15	Brillouin scattering data for single crystals of methane I at 72.8 K.	114
5.16	Brillouin scattering data for single crystals of methane I at 50.9 K.	116
5.17	Brillouin scattering data for single crystals of methane I at 38.5 K.	118
5.18	Brillouin scattering data for single crystals of methane I at 25.0 K.	119
5.19	Temperature dependent data for methane I single crystals	121
5.20	Temperature dependent data for Pockel's ratios and coefficients for methane I single crystals	121
6.1	Elastic constants of fcc phases of CO, N_2 and argon	123
6.2	Ratios of acoustic velocities in the high symmetry directions of SF_6 , CH_4 , and rare gas solids near their triple points as compared to those of $\alpha-CO$	124
6.3	Ratios of acoustic velocities in the high symmetry directions of several molecular crystals	129
6.4	Acoustic transverse velocity of slow T_1 mode as a function of temper- ature between the triple point and the γ - β phase transition in O_2	130
6.5	Ratios of acoustic velocities in the high symmetry directions of several molecular crystals	135

6.6	Elastic constants of methane I as a function of temperature along with those of the rare gas solids near their triple points.	135
6.7	Elastic constants of CD_4 determined by various theoretical and experimental techniques	137

Introduction

(1) Plastic crystals and order-disorder phase transitions

The study of plastic crystals and order-disorder phase transitions is a branch of condensed matter physics which has attracted considerable attention in recent years. The discovery of plastic crystals in 1957 by L. Goldschmidt and J. H. Drenth, and the subsequent discovery of order-disorder phase transitions in 1961 by J. H. Drenth and L. Goldschmidt, have opened up a new field of research in the area of solid state physics.

Plastic crystals are a class of solids in which the molecules are arranged in a regular lattice, but the orientation of the molecules is disordered. This type of order is called orientational order. The transition from a plastic crystal to a crystal with long-range order is called an order-disorder phase transition. This type of transition is characterized by a change in the symmetry of the crystal structure. The study of plastic crystals and order-disorder phase transitions is important because it provides a new way of understanding the behavior of solids at high temperatures and under high pressure.

Chapter 1.

Introduction

1.1 Plastic crystals and order-disorder phase transitions

This work involves a study of the role of rotation-translation coupling in some simple molecular crystals, namely, large single crystals of α -carbon monoxide (α -CO), γ -oxygen (γ -O₂), cyclooctane I (C₈H₁₆ I) and methane I (CH₄ I). Brillouin spectroscopy was used to observe the behaviour of acoustic phonons at various temperatures particularly on approaching the order-disorder phase transitions.

Orientational disorder in molecular crystals refers to a situation in which the centers of mass of an aggregate of molecules form a regular lattice with long range positional order while their orientations display some degree of disorder. Plastic crystals are orientationally disordered solids with considerable rotational freedom and are an intermediate phase between the completely ordered low temperature crystalline phase and the high temperature liquid phase ^{[1][2]}. In the literature, the plastic phase has been called the rotor phase and the rotational crystalline state ^[3]. Such crystals are soft or waxy and extreme cases are known where flow under gravity occurs. In

contrast, the low temperature phase is usually hard and brittle.

Properties of plastic crystals vary from one molecule to another and they may exhibit one, two or three plastic phases. The temperature range for which a plastic phase is stable can vary from a few degrees for van der Waals solids to hundreds of degrees for ionic solids. The original criterion of plasticity proposed by Timmermans^[4] is that the entropy of fusion must be less than 5 cal/degree/mole. With a few exceptions this rule holds for crystals exhibiting plasticity. The disordered phase is usually of high symmetry, mostly cubic and sometimes hexagonal, and the transition to the ordered phase is usually of first order. The molecules forming these crystals are generally globular in shape and of high symmetry, i.e. tetrahedral, octahedral or spherical. In plastic crystals, the static or time-dependent part of the potential is weak compared to the fluctuating or time-dependent part and therefore a diffusion of the molecules with respect to their angular degrees of freedom takes place. The barrier between two positions of minimum potential energy is small enough so that molecules jump from one orientation to another fairly rapidly and are therefore effectively distributed randomly between different possible orientations^[1]. In the orientationally ordered state the molecules may librate in the lattice about a particular direction. The orientational order-disorder transition is analogous to the ferromagnetic-paramagnetic transition in that the magnetic moments are randomly oriented in the paramagnetic phase and ordered in the ferromagnetic phase.

In orientationally disordered crystals and particularly plastic crystals, there is

generally a coupling between the orientational variables and the acoustic phonons which is often sufficiently strong to alter the nature of collective excitations, and which therefore plays an important role in the transition to the ordered state [5]. The transverse acoustic phonons are expected to be very sensitive to rotation-translation (RT) coupling and consequently a decrease in the frequency of these modes can occur near the phase transition [6]. This softening results in structural instability and gives rise to a decrease in the magnitude of certain elastic constants and the crystal transforms to a more stable state with the atoms adopting new sites.

1.2 Rotation-translation coupling: literature review

The importance of the dynamic coupling between translational and rotational degrees of freedom was first realized in liquids [7]. This coupling results in a doublet in the depolarized Rayleigh scattering intensity of liquids. A liquid may undergo elastic deformation if the stress is applied for a sufficiently short period of time.

Several theories have been proposed in order to explain the light scattering by shear waves in liquids, Rytov's theory being the most general [7]. Using the theory of viscoelasticity, Rytov assumed that the shear modulus was frequency dependent and hence predicted the inclusion of shear waves in the excitation modes of liquids. By assuming that the fluctuations in the dielectric constant and the strain were coupled through the photoelastic constants, he showed that the frequency spectrum of the depolarized scattered light contained two doublets, one due to the longitudinal excitation and the other due to the shear waves [8]. High resolution studies of the depolar-

ized spectra from a number of liquids have indicated the existence of shear waves [9]. Since the doublet separation varied with q vector, it was proposed that the doublet was due to thermally excited shear waves. The observed lineshapes and intensities were in agreement with Rytov's theory. In addition to the two doublets, the spectra contained a broad depolarized component known as the Rayleigh "wing". This component was believed to originate from molecular rotation in liquids. Rotation-translation (RT) coupling plays an important role in the order-disorder phase transition in molecular crystals [10] [11] [12]. The transverse acoustic phonons are generally very sensitive to RT coupling [6]. Softening of the transverse acoustic phonons can result in the increased mechanical instability of the solid as the phase transition temperature is approached [13]. This softening of phonons then results in the decreasing of shear elastic constants and can be measured by various spectroscopic techniques.

Michel *et al.* [10] [11] [12] in a series of theoretical papers studied the influence of RT coupling in ionic molecular crystals including alkali cyanides, peroxides, hydroxides and hydrosulfides near their structural phase transitions. The high temperature phase of these solids is cubic with the anions surrounded by an octahedral cage of cations. The anions assume octahedral symmetry by reorienting among equivalent orientations. The low temperature phase is more ordered in the sense that the anions are oriented along a specific direction performing librational motion. The theory treated the anions as linear dumbbells, the two ends of which interacted with the cations via a Born-Mayer potential. This potential was a function of the orientation

of the dumbbell and the center of mass position of the anions and cations and was expanded in terms of small displacements from equilibrium positions for all particles. The resulting Hamiltonian included terms with translational and rotational degrees of freedom and an extra term describing the coupling between these motions. This Hamiltonian was then used to study the elastic properties of the ionic molecular crystals by deriving expressions for coupled susceptibilities between various degrees of freedom. It was found that the RT coupling in these solids resulted in a vanishing value of the shear elastic constant C_{44} near their structural phase transitions and was in agreement with the results of Brillouin [14] and neutron scattering [15] and ultrasonic measurements [16]. For instance, softening of transverse acoustic phonons was observed in inelastic neutron [15] and Brillouin scattering [17] of *KCN* as the phase transition temperature was approached.

Of particular importance in the study of RT coupling is the role of symmetry of the lattice and the presence or absence of a center of symmetry in the molecule. Michel *et al.* later emphasized and incorporated the notion of symmetry in their theory. They expanded the coefficients in the expansion of the potential in terms of symmetry adapted functions which appropriately describe the molecular orientation in disordered solids [18]. The symmetry adapted functions are constructed from spherical harmonics and take both the molecular symmetry and the site symmetry into account. They noted that molecules of low symmetry exhibited a strong RT coupling whereas molecules with high symmetry favoured a much weaker RT coupling. For

centrosymmetric molecules, only even values of the total angular momentum quantum number l coupled to the transverse acoustic phonons and the strength of the coupling was proportional to q in the long wavelength limit. However, for non-centrosymmetric molecules, odd values of l were also important. The coupling vanished quadratically in q for odd values of l in the long wavelength limit i.e. ($q = 0$).

Molecular dynamics simulation has been used to study the coupling between the rotational variables and translational acoustic modes in orientationally disordered ionic crystals. This simulation was applied, in particular, to alkali cyanides [19]. A coupling parameter λ was defined and its wavevector dependence was studied in the simulation. It was found that λ is maximum near the center of the Brillouin zone particularly along the [100] and the [110] directions. It was noted that in the [100] direction, for instance, the coupling constant vanished near the boundary of the Brillouin zone. This was explained by noting that the planes of cations moved in phase near the boundary of the zone and hence the strain at the anion site was zero. This technique has been applied to nonionic molecular systems [20] [21].

The elastic soft mode behaviour and orientational ordering in $K_xRb_{1-x}CN$, in terms of the bilinear coupling, has been studied by Fossum *et al.* [22]. Yamada *et al.* [23] studied the order-disorder phase transition in ammonium halides. They assumed a phenomenological Hamiltonian which included coupling between the phonons and the pseudo-spin operator. The pseudo-spin operator described the variables that play the role of the order parameter and the transition was interpreted in terms of

the ordering of the spins. The softening of phonons near the order-disorder phase transitions can be studied in the framework of spin-phonon coupled systems.

Wang [24] developed a unified theory for depolarized Rayleigh-Brillouin spectra and RT coupling in molecular liquids and solids using linear response theory. He noted that for solids near the melting point, the coupling became significant and the harmonic approximation (as used by Michel) was not valid. He derived an expression for the depolarized Rayleigh-Brillouin spectral density applicable to both liquids and solids and included the static and dynamic RT coupling in his calculations. In the limit of the harmonic approximation, his theory reduced to the theory developed by Michel and also explained the results obtained for the spectra of liquids. Wang suggested that his theory can be used to explain the soft mode behaviour of the transverse acoustic phonon mode in alkali cyanides near the phase transition.

The theory of elastic and phonon softening in ionic molecular crystals has also been developed by Sahu *et al.* [25]. They evaluated the RT coupling in very similar ways to Michel but included the effect of short range repulsive forces, anisotropic electrostatic forces and direct interaction between the molecules. They noted that there was an appreciable contribution to RT coupling due to the interaction between electric quadrupole moments of the cyanide ions and the fluctuating electric field gradient in the disordered phase. This coupling was opposite in sign to the coupling due to short range repulsive forces. However the first coupling was stronger and gave rise to soft mode behaviour and lattice instability in alkali cyanides. They derived

expressions for the elastic constants (C 's) of the coupled system in terms of the elastic constants of the uncoupled system. It appeared that coupling increased the uncoupled elastic constant C_{12} value but reduced C_{11} and C_{44} as discussed in Section 3.3.

Instability of a coupled phonon-rotor system has been studied by Huller *et al.* [26] and the model was applied to s-triazine. S-triazine undergoes an order-disorder phase transition from a trigonal to monoclinic structure at 199 K. Raich *et al.* [27], using a mean field approach, considered a bilinear coupling term in their Hamiltonian of the form $Ae\eta$ where e is the strain, η the order parameter for the transition and A is a constant. They calculated the generalized susceptibilities and showed that RT coupling leads to a softening of acoustic phonons near the phase transition. They suggested similar approaches to other trigonal systems including benzil and chloranil [28].

Rotation-translation coupling also plays a very important role in the dynamics of van der Waals solids in particular in hexagonal, and cubic systems. A review of the experimental and theoretical work is now presented.

The α and β phases of solids N_2 and CO represent systems that undergo orientationally disordered hexagonal close-packed (hcp) to orientationally ordered face-centered cubic (fcc) phase transitions. The triple points for the β phases are 68.15 K and 63.15 K for CO and N_2 , respectively, whereas the α - β phase transition temperatures are 61.55 K and 36.5 K, respectively. The difference between the ranges of stability of the β phases is the biggest dissimilarity between the two. It was suggested that RT coupling is stronger in β - CO due to physical asymmetry [29], and hence or-

dering occurs more readily, while N_2 is centrosymmetric with weaker RT coupling effects. The self consistent phonon approximation of anharmonic lattice dynamics was used by Goldman *et al.* [30] to calculate the elastic constants of hcp β - N_2 . They neglected the orientational correlation and its effect on the dynamics of the center of mass. This resulted in the calculations of the transverse mode frequencies being larger than the frequencies obtained by Brillouin studies of Kieft *et al.* [31] by more than a factor of 2. Both observed shear constants were softer than their calculated values and therefore indicated the possible importance of RT coupling and orientational correlation in β - N_2 . Brillouin scattering studies of cooled single crystals of β - N_2 indicated no further softening in the transverse frequencies, and an increase of 1%/K for all five elastic constants with decrease of temperature was noted [32]. The transverse acoustic frequencies were, however, already quite soft in β - N_2 at the triple point, particularly when compared to rare gas solids [33] [34] [35] and the harmonic approximation calculation [30].

Van der Avoird *et al.* [36] have emphasized the inadequacy of quasi-harmonic approach to crystal dynamics and have developed a more general lattice dynamics scheme for handling large amplitude librational motion or hindered rotation, anharmonic translational vibrations, and RT coupling in molecular crystals. This theory yielded for the first time a quantum dynamical description of the molecular motion in the plastic β phase and an accurate α - β transition temperature. This theory also suggested that the orientational disorder in β - N_2 was caused by rapid 60° jumps

around the c -axis between localized librational states, and further predicted the correct experimental libron and translational phonon band. Brillouin scattering studies in single crystals of β -CO as a function of temperature revealed no further softening even within 0.5 K of the phase transition. As in β -N₂, the transverse phonons were, however, quite soft near the triple point and near the phase transition temperature. The elastic constants showed an increasing rate of 1%/K upon cooling [32].

Cubic phase van der Waals solids have been studied extensively in an effort to understand the role of RT coupling in their order-disorder phase transition. Succinonitrile forms a cubic bcc plastic crystal from the triple point of 330.15 K to 250.15 K. Dielectric studies have indicated very little change at the melting point, which suggested that the orientation of molecules in the plastic phase close to the triple point and in the liquid were very similar [37]. Light scattering studies of this plastic phase in the temperature range of 243.15 K to 323.15 K have been carried out by analyzing the polarized and depolarized spectra scattered at 90° [38]. There was no indication of shear phonons in the polarized spectra below 283.15 K which is unusual for cubic crystals. A pair of depolarized components appeared above 283.15 K, whose intensity increased with temperature and was quite distinct at 323.15 K. It was assumed that these components were due to transverse phonons. It was suggested that at low temperatures the slowly orienting molecules may dampen the shear waves when the molecular reorientational frequency is comparable to that of the shear phonons. At higher temperatures the two frequencies are quite different and hence the interaction

between the acoustic phonons and molecular reorientation is weaker. Rayleigh and Brillouin scattering studies in single crystals of succinonitrile indicated high elastic isotropy with respect to the propagation of ultrasonic waves [39]. Further Rayleigh-Brillouin measurements of the depolarized light scattering by Bischofberger *et al.* [40] revealed other interesting features. The positions and intensities of the shear wave peaks were strongly dependent on crystal orientation and had a non-Lorentzian shape. Using hydrodynamic theory, Courtens [41] developed a theory for the depolarized light scattering in succinonitrile taking into account the static coupling between the displacement and the reorientation of the molecules. He assumed a phenomenological Hamiltonian which included a bilinear coupling term and correctly predicted the elastic constants and the lineshape of the shear wave peaks, in excellent agreement with experimental results.

Solid CBr_4 has an orientationally disordered fcc structure from the triple point of 365 K down to 320 K where it transforms to an orientationally ordered monoclinic structure. In the disordered phase, the $C - Br$ bond lies in the vicinity of $\langle 110 \rangle$ direction [42]. The translational and librational motions of the molecules are quite large and result in diffuse neutron scattering [43]. This makes the orientationally disordered phase of CBr_4 a good candidate for studying RT coupling. Neutron scattering of this plastic phase of CBr_4 indicated weakening of acoustic phonons near the zone boundary. Molecular dynamics simulation work on CBr_4 showed that the coupling between the acoustic phonons and rotational variables was very strong [44].

The wavevector dependence of this coupling was calculated and showed no coupling at the $q = 0$ wavevector regime but did predict a strong coupling over the surface of the Brillouin zone [45]. Brillouin scattering experiments on single crystals of CBr_4 near the triple point revealed softening of the shear acoustic phonons in the $\langle 111 \rangle$ and especially the $\langle 110 \rangle$ directions [46]. The ratios of the acoustic velocities V_L/V_T particularly in these high symmetry directions were anomalously higher than those of rare gas solids (spherical atoms) as shown in Table 1.1. This was in agreement with neutron scattering experiments that demonstrated a maximum in probability distribution of orientation in the $\langle 110 \rangle$ direction and suggested a strong RT coupling

Table 1.1: Ratios of acoustic velocities in high symmetry directions of several cubic crystals close to their triple point temperatures.

	$\langle 100 \rangle$ $V_L/V_{T_2}(= V_L/V_{T_1})$	$\langle 111 \rangle$ $V_L/V_{T_2}(= V_L/V_{T_1})$	$\langle 110 \rangle$ V_L/V_{T_2}	$\langle 110 \rangle$ V_L/V_{T_1}
Rare gas solids				
Ne, Ar, Kr, Xe [35]	1.44	2.24	1.65	2.71
CBr_4 [46]	1.66	2.74	1.87	3.74
$CCl_4(I_a)$ [47]	1.79	3.07	2.01	4.70
SF_6 [48]	1.60	2.29	1.76	2.64

near the $q = 0$ regime [44]. CBr_4 is non-centrosymmetric and according to Michel's theory [5] should exhibit significant RT coupling near the Brillouin zone center ($q = 0$). This and the Brillouin scattering results are not consistent with the above mentioned simulation results.

CCl_4 has an orientationally disordered fcc phase I_a which forms at 246.0 K. How-

ever, it was later discovered that there is a rhombohedral phase I_b with melting point of 250.5 K [49]. Both phases have low entropies of fusion. The metastability of phase I_a which readily forms into this second phase I_b with a higher melting point has been a subject of fascination and discussion for many years. Molecular dynamics simulation of the I_a phase of CCl_4 by McDonald *et al.* [50] showed that the $C - Cl$ bond had a maximum in orientational probability in the $\langle 110 \rangle$ direction similar to CBr_4 . Strong damping of acoustic phonons specially in the $\langle 110 \rangle$ direction was noticed. Brillouin scattering experiments on the I_a phase of CCl_4 revealed interesting results [47]. The ratio of the acoustic velocities V_L/V_T in the $\langle 110 \rangle$ direction was greatest in $I_a CCl_4$ compared to other orientationally disordered solids and was 70% higher than the corresponding ratio for the rare gas solids as seen in Table 1.1. This corresponded to the value of C_{12} being close to C_{11} . Since one of the conditions for the stability of a solid is that C_{11} must be larger than C_{12} , this was an indication that the I_a phase was very unstable. The importance of RT coupling in CCl_4 (as in CBr_4) in the $q = 0$ regime was consistent with Michel's theory [5] of the role of symmetry in the RT coupling for noncentrosymmetric CCl_4 molecule. It was concluded that RT coupling was probably responsible for the highly metastable nature of the I_a phase.

SF_6 forms a plastic bcc crystal which is orientationally disordered from its triple point at 222.4 K down to 96.0 K. The molecules have near spherical symmetry resulting in considerable rotational freedom. Simulation studies of SF_6 [51] indicated that the disorder was due to a competition between different orientational interactions. If

the $S - F$ bonds lie along the crystal axes, the nearest neighbour interactions were attractive while the next nearest neighbours were repulsive. This resulted in disorder called "orientational frustration". Simulation work further indicated that neighbouring molecules were unable to move towards one another from their respective lattice sites without a change in their relative orientation. A molecule displaced from its site would experience a strong reorienting torque. As the temperature was increased, the displacements and the reorientation of the molecules increased, and the magnitude of the coupling increased. Neutron scattering experiments have shown that well defined collective excitations did not exist in SF_6 and that the acoustic modes were overdamped away from the Brillouin zone center but could be resolved for small wavevectors [51]. Simulation work predicted a cross over from oscillatory to highly damped collective motion at small wavevector due to RT coupling. A temperature dependence study of RT coupling in SF_6 by the simulation technique showed a strong effect which had little dependence on temperature in all directions [20]. Subsequent Brillouin scattering studies of SF_6 by Kieft *et al.* [48] showed no evidence of acoustic softening and well defined acoustic mode existed at the $q = 0$ regime as was consistent with neutron scattering results. The ratio V_L/V_{T_1} was only 10% higher than the ratio for rare gas solids in $\langle 100 \rangle$ direction as shown in Table 1.1, and therefore suggested no significant RT coupling. This agreed with Michel's theory of the role of symmetry in order-disorder transitions [5], in that, SF_6 was centrosymmetric and of high symmetry ($l = 4$) and the coupling should accordingly be very weak near the

zone center.

It must be noted that very little transverse mode softening is necessary to induce structural instability. This was clear in the Brillouin spectroscopic studies of fcc-hcp phase transitions in $Ar(O_2)$ alloys [34] where only a slight decrease (2% in C_{44} (due to increase in O_2 concentration) was exhibited during the phase transition. The interaction between the rotational motion of O_2 molecules and the translational motion of Ar molecules (as was also noted in low frequency Raman experiments [52]) seemed to be the driving mechanism for the transition.

Another approach to the role of symmetry in determining the strength of RT coupling has also been considered by Dove *et al.* [20] [21]. Using computer simulation techniques they studied three types of disorder. In type I disorder (eg. SF_6), the lattice and the site had the same symmetry. Here coupling was strong near the zone center and vanished near the boundary. In type II disorder (eg. CBr_4) the molecular symmetry was lower than that of the site and the coupling vanished at the zone center and was strong near the zone boundary. In type III disorder (eg. C_2F_6), the molecular symmetry was lower than the site, however, and the main properties of this phase were determined by the molecular symmetry. The coupling constant was found to behave similar to that of type I disorder. They commented that for centrosymmetric molecules, the coupling vanished at the zone boundary and for non-centrosymmetric molecules, the coupling vanished at the zone center (as they calculated for CBr_4). This is not entirely consistent with calculations of Michel [5] which seem to indicate

that RT coupling can be strong in noncentrosymmetric molecules near the zone center.

In the present work (as noted earlier) high resolution Brillouin scattering experiments were carried out on large oriented single crystals of α -carbon monoxide, γ -oxygen, cyclooctane I and methane I at various temperatures towards their order-disorder phase transition. The acoustic phonons were probed and the adiabatic elastic constants were determined. The importance of the role of RT coupling in these systems was consequently studied. The systems under investigation are described in the next chapter.

Chapter 2

Systems under investigation

2.1 Introduction

The understanding of molecular crystals advanced greatly with the study of rare gas solids. Rare gases are monatomic and spherical and therefore form the simplest solids in nature. They have been studied extensively by various theoretical calculations and experimental methods. A review of the various theories, models and experimental results on rare gas solids has been published in two volumes of "Rare Gas Solids" [53]. The development of interatomic potentials to correctly account for the properties of rare gas solids has been a major objective of these investigations. These solids can be represented by relatively simple models that are important in the general development of molecular theory of matter. It is, however, clear that the inclusions of large anharmonic effects, 2-body interactions, and 6-12 potential functions in these models are not enough to adequately reproduce the experimental results.

In diatomic molecules a complication arises due to their nonsphericity. The intermolecular potential must then include terms involving the intermolecular distance

and possibly several orientational (rotational) variables. The rotational motion may then interact with the translational motion of the molecules and alter the nature of collective excitations as discussed in Chapter 1. Plastic diatomic molecular crystals are the prime candidates for this study as they possess large rotational freedom which can couple to the translational motion (as in [10] [11] [12]). The effect of such an interaction is expected to exhibit itself most clearly near order-disorder phase transitions where the rotational freedom is greatly reduced in the ordered phase.

A method has been developed in the present laboratory to consistently and successfully cool single crystals to as low as 10 K. This method is explained in Section 4.5. The behaviour of the acoustic phonons can be probed by studying the Brillouin spectra of plastic crystals as a function of temperature. Such studies are important for a better understanding of phase transitions in simple plastic solids.

2.2 Carbon monoxide

CO and N_2 as explained in Section 1.2 undergo order-disorder phase transitions from hcp (β) to fcc (α) phases at 61.55 K and 35.6 K respectively. *CO* and N_2 are iso-electronic and have the same size and identical masses. Melting and boiling points are very similar and the lattice constants are almost identical. The entropy of fusion for both solids is about 2.73 cal/K/mole at their respective triple points. The phase diagrams of N_2 and *CO* have been determined by various spectroscopic and thermodynamics techniques and are shown in Fig. 2.1 [54].

Temperature dependence studies of the molar volume shows that *CO* and N_2

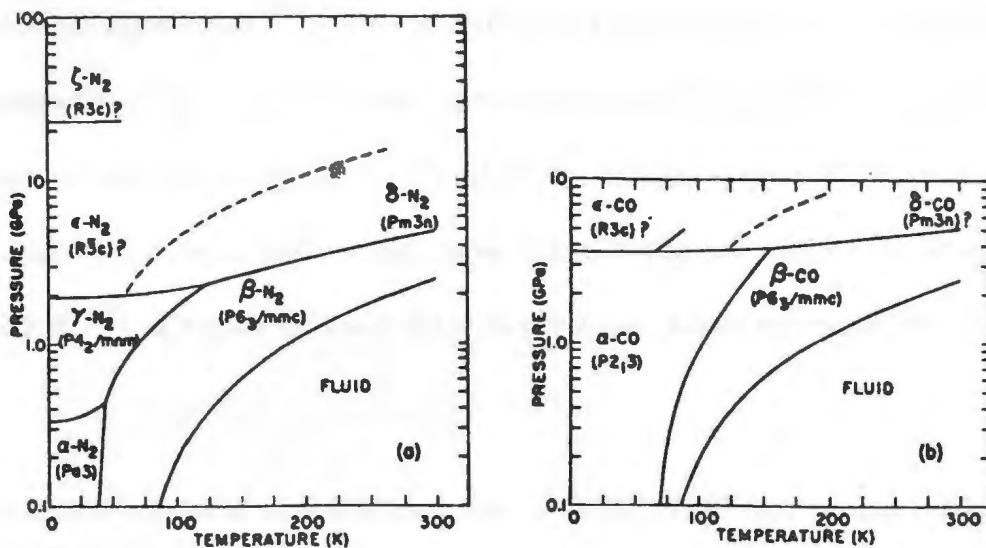


Figure 2.1: Phase diagrams of solid nitrogen and carbon monoxide.

behave very similarly above 70 K and below 30 K [55]. Between these temperatures they solidify to a disordered hcp β phase with space group $P6_3/mmc$ [56]. At lower temperatures N_2 exists in the ordered face-centered cubic α phase with space group symmetry $Pa3$ [58] [59] while CO packs as $P2_13$ [57] due to its heteronuclear structure. The molecules are slightly displaced, from fcc, along the $C - O$ axes which are aligned in the direction of the body diagonals of the cubic cell with head-to-tail disorder. The triple point temperature for the β phases of N_2 and CO are 63.15 K and 68.15 K, respectively (at normal pressures i.e. effective $P = 0$). The α - β phase transition, however, occurs at 35.6 K for N_2 and 61.55 K for CO and is the biggest dissimilarity between the two. The factors resulting in this dissimilarity are suggested to be either the larger quadrupolar interaction [62] in CO which favours ordering over a larger

temperature range in α - CO than in α - N_2 or a stronger RT coupling in β - CO (due to physical asymmetry [29]) than in β - N_2 which orders β - CO more readily. The elastic constants of the hcp phases near their respective triple points are very similar. The ratio of acoustic velocities V_L/V_T of β - N_2 and β - CO near their triple points are, however, somewhat higher than those of the hexagonal argon alloy $Ar_{94\%}(O_2)_6\%$ at 82.2 K [34] as shown in Table 2.1. Since argon atoms are spherical in shape (and

Table 2.1: Ratio of acoustic velocities in β - N_2 , β - CO and $Ar_{94\%}(O_2)_6\%$ near their respective triple points

V_L/V_T	β - N_2	β - CO	$Ar_{94\%}(O_2)_6\%$
$\langle 001 \rangle$			
$\sqrt{\frac{C_{33}}{C_{44}}}$	2.48	2.43	2.22
$\langle 100 \rangle$			
$\sqrt{\frac{C_{11}}{C_{44}}}$	2.39	2.32	2.11
$\langle 010 \rangle$			
$\sqrt{\frac{C_{11}}{C_{33}}}$	2.29	2.24	2.04
$\langle 110 \rangle$	Same as $\langle 100 \rangle$ and $\langle 010 \rangle$		

molecular rotation is therefore irrelevant), this higher ratio may be attributed to the interaction between the rotational motion and the acoustic phonons in N_2 (and CO) molecules. The Cauchy ratios C_{13}/C_{44} are about 3.2 and 2.6 for the β phases of N_2 and CO and are much higher than 1.8 for the hexagonal argon alloy and seem to indicate the importance of noncentral angle dependent forces. The difference in the Cauchy ratios between N_2 and CO may again be indicative of different RT coupling effects in these two solids as related to the dissimilarity in their α - β phase transition

temperature.

Fracassi *et al.* [6] investigated RT coupling and the lattice dynamics of α -CO using several intermolecular potentials. They concluded that RT coupling leads to an anomaly in the transverse acoustic mode in the $\langle 111 \rangle$ direction. Computer simulation studies of the dynamical structure factor of α -N₂ showed a large negative shift of the transverse acoustic phonons in the $\langle 100 \rangle$ and $\langle 110 \rangle$ directions as the temperature was increased towards the α - β phase transition temperature [63]. Lattice dynamics calculations have also shown that RT coupling lowers the sound velocities in α -N₂ [64]. The importance of libron-phonon coupling in α -N₂ has been demonstrated by Jansen *et al.* [36] using mean field theory and an extended random phase approximation. Their calculations accurately predict the α - β phase transition temperature and the libron and translational phonon bands at 50 cm⁻¹ and 25 cm⁻¹, respectively. Several previous attempts were made to study the α - β phase transition of N₂ in this laboratory by cooling β -N₂ single crystals towards the phase transition and monitoring the behaviour of the elastic constants [32]. However, close to the phase transition temperature, the samples could not be freed from the walls of the cell (due to low vapour pressure). The large temperature range required to cool β -N₂ (to the phase transition) caused very slow progress. It was therefore decided to study the very similar α - β phase transition in CO which had the advantage of a much smaller cooling range (nearly 6.5 K) from the triple point to the phase transition temperature. By determining the elastic constants near the transition temperature of α -CO, it is

possible to study the behaviour of acoustic phonons and possible associated softening due to RT coupling for comparison to the theoretical predictions. This is discussed in Section 5.1.

2.3 Oxygen

Oxygen was studied primarily to understand several unusual features observed earlier [65] (as noted below) in the Brillouin spectra of γ - O_2 near the triple point and to study the order-disorder phase transition in O_2 with the associated RT coupling and possible magnetic effects.

The electronic ground state of O_2 is $^3\Sigma_g$ which means that there are two unpaired electrons in the outermost shell and therefore O_2 exhibits magnetic effects. The phase diagram of O_2 has been determined by various techniques and is shown in Fig. 2.2 [66]. There are three (essentially) zero-pressure solid phases. The liquid freezes at the triple point of 54.49 K into a paramagnetic disordered primitive cubic γ - O_2 (space group Pm3n). The entropy of fusion is 1.96 cal/K/mole at this temperature. At 43.78 K, the γ phase transforms to ordered rhombohedral β - O_2 which is weakly antiferromagnetic. At 23.89 K, the β phase transforms to an ordered monoclinic α phase which is antiferromagnetic. The γ phase is a primitive cubic structure with 8 molecules in the unit cell. The structure of this phase is shown in Fig. 2.3. There are two inequivalent sites in this structure: 2 of the molecules, one at the center and the other at the corner(s) are spherically disordered in orientation whereas the remaining 6 have disk-like rotation about the $\langle 100 \rangle$ directions [67]. Raman spectra

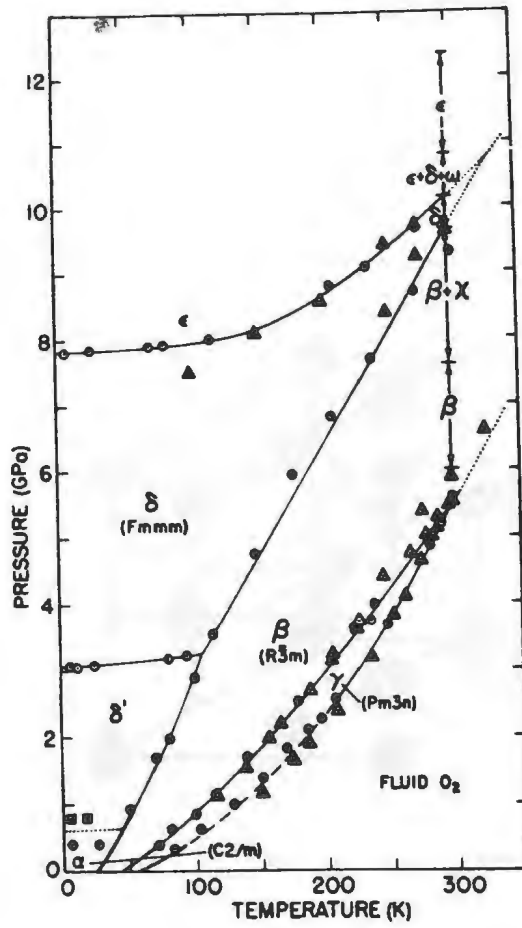


Figure 2.2: Phase diagram of solid O_2

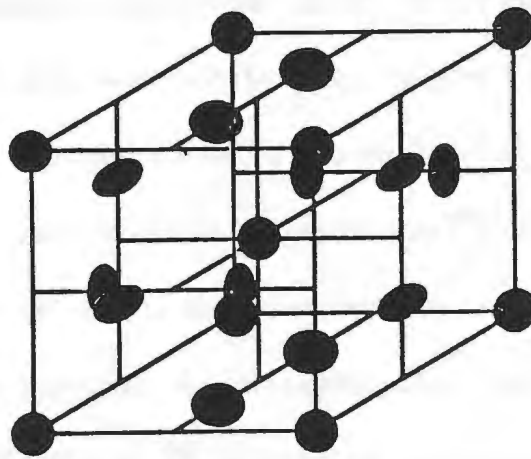


Figure 2.3: Structure of γ - O_2

of the γ phase and the liquid phase have very similar features [68] [69]. This is also apparent in the molecular dynamics simulation studies of these two phases [70] and demonstrate rotational freedom in γ - O_2 . Vibrational Raman spectra of single crystals of γ - O_2 indicated two distinct Raman lines separated by 1.08 cm^{-1} due to the two inequivalent sites [69]. The intensity ratio of the two lines was 1 to 3 with the stronger line arising from rotation of disk-like molecules. The full width at half height of the stronger and the weaker lines were 3 GHz and 5 GHz respectively indicating different degrees of freedom (probably related to rotation) for the two inequivalent sites.

Lattice dynamics calculations of γ - O_2 has been reported [71]. Elastic constants were calculated from the dispersion curves. It was noted that C_{12} was about 5 times smaller than its measured value by Brillouin spectroscopy [65]. It was concluded that the potential model was too stiff to the shear deformation due to the absence of RT coupling term in the potential. As mentioned earlier, the Brillouin scattering technique was used by Kieft *et al.* [65] to study the spectra of single crystals of γ - O_2 and determine its adiabatic elastic constants near the triple point. The observed Brillouin spectra had interesting and unique features which could be either due to the magnetic nature of oxygen or to the peculiar structure of γ - O_2 . These features are: (1) Only one transverse component was ever observed for all the orientations studied. This was considered unusual because cubic crystals generally give rise to two transverse components in their Brillouin spectra. (2) Little variation in the frequency shifts from one crystal orientation to another was noted i.e. γ - O_2 single crystals

appeared to be isotropic with respect to sound propagation at GHz frequencies and, of course explains why there was only one transverse acoustic mode observed in the Brillouin spectrum. (3) The intensity ratio of the transverse to longitudinal component varied from 0.4 to 2.0 depending on the orientation of the crystal. This was unusually high. (4) All the spectra showed a high constant low level background whose origin was not investigated. They [65] determined the adiabatic elastic constants and noted that $\gamma\text{-O}_2$ did not obey Cauchy relation which must hold for cubic crystals if the forces acting between molecules are central in nature. The Cauchy ratio C_{44}/C_{12} was 0.13 for $\gamma\text{-O}_2$ (as compared to nearly 0.73 for rare gas solids) and was indicative of the possible importance of non-central angle dependent forces in this plastic crystal.

In order to attempt to explain the (above mentioned) unusual features of $\gamma\text{-O}_2$ Brillouin spectra, magnetic field experiments were done. It was suspected that magnetic coupling to the acoustic phonons may play an important role in the dynamics of $\gamma\text{-O}_2$. Theoretical studies have indicated a lowering of libron frequencies in the presence of a strong magnetic field (5-30 T) in $\beta\text{-O}_2$ [72]. The magnetic susceptibility of the γ phase is three times larger than that of the β phase [73]. Hence it may be possible to observe changes in the Brillouin spectrum of $\gamma\text{-O}_2$ in the presence of a much weaker magnetic field (0.45 T in this experiment). Likewise, $\gamma\text{-O}_2$ possesses large rotational freedom and RT coupling may be important in the dynamics of this solid. Consequently it was decided to look at $\gamma\text{-O}_2$ again (in this laboratory). The behaviour of transverse acoustic phonons on approaching and on going through

order-disorder phase transition is therefore of interest. Brillouin spectra of γ - O_2 single crystals were studied from 54.0 K to 44.0 K and the γ - β phase transition was carried out as explained in Section 4.2.

2.4 Cyclooctane

The phase diagram of cyclooctane (C_8H_{16}) has been determined by NMR [74] [75] and calorimetric [76] studies. Liquid cyclooctane freezes at 288 K to form plastic cyclooctane I (space group Pm3n) which is orientationally disordered. The entropy of fusion at this temperature is 2 cal/K/mole [76]. At 183.8 K, phase I transforms to another rotor phase II which seems to be very similar to phase I in orientational disorder. The entropy of transition is about 0.4 cal/K/mole. Phases I and II are usually referred to as I/II phase. At 166.5 K, phase II transforms to phase III which is a non-rotor phase and is believed to be monoclinic. The entropy of transition is about 9 cal/K/mole [76].

There are two reasons why cyclooctane I was studied for this work: (1) X-ray diffraction measurements have indicated that cyclooctane I has exactly the same crystal structure (Pm3n) and symmetry as γ - O_2 [77]. (2) The NMR [74] [75], and Raman studies [78] in cyclooctane I indicated large rotational freedom and the liquid and phase I had similar spectral features. The deuterium NMR experiments indicated that 75% of the molecules were undergoing simultaneous pseudorotation and uniaxial rotation as pancakes (disks) while 25 % rotated like spheres and was in agreement with the x-ray results [77]. The molecular reorientation time was estimated to be

of the order of 10^{-9} s (~ 1 GHz in frequency). This reorientational frequency is of the order of the Brillouin frequency shifts in plastic crystals and hence RT coupling is expected to be strong in cyclooctane I. The behaviour of acoustic phonons with temperature can be used to study the strength of this coupling as the phase transition is approached. If the unusual features in γ -oxygen were related to its structure and the rotational freedom in that structure, then similar features should be present in the Brillouin spectrum of cyclooctane I.

Cyclooctane single crystals were grown and the Brillouin spectra were recorded from 284.2 K down to 224.2 K as explained in Section 5.3. It should be noted that β -fluorine [1], high pressure phases δ -nitrogen and δ -carbon monoxide [54], cyclooctanone and cyclononanone [79] also occur in the Pm3n structure.

2.5 Methane

Methane was studied since RT coupling is known to be significant in this solid near the triple point. Heavy methane (CD_4) exists in an orientationally disordered plastic fcc phase I (space group Fm3m) between the melting point of 89.8 K and the phase transition temperature 27.2 K to the partially ordered James and Keenan structure II (space group Fm3c) [80]. The entropy of fusion at the melting point is 2.42 cal/K/mole [81]. In the second phase, 6 out of the 8 molecules in the unit cell are orientationally ordered. The structure of both solid phases were predicted by James and Keenan [82] using a molecular field approach assuming only octupole-octupole interactions between nearest neighbour molecules and was later confirmed by coher-

ent neutron scattering studies [80]. The James and Keenan phase transforms to an ordered tetragonal phase III at 22.4 K [80]. The phase transition at 27.2 K is believed to be second order while the one at 22.4 K is considered first order [80].

Methane (CH_4) exists in an orientationally disordered plastic fcc phase I (space group Fm3m) between the melting point of 90.4 K and the phase transition temperature 20.6 K to the partially ordered James and Keenan structure II (space group Fm3c). The entropy of fusion at the melting point is 2.48 cal/K/mole [81]. Phases I and II of methane are isostructural with the corresponding phases of heavy methane [83]. The existence of a third phase in methane at about 8 K has been suggested [84]. The transition at 20.6 K is probably a second order phase transition [85].

Although both solid I phases are orientationally disordered, the molecular rotational motion is not completely free. The infrared spectrum of methane at 77 K consisted of a broad band which was believed to be due to hindered rotational motion [86]. This was further supported by the Raman studies which indicated that the rotational correlation function was quite different from that of a freely rotating spherical top molecule [87]. Inelastic neutron scattering studies in CD_4 [88] have indicated no well defined librational excitations, however, shoulders in the neutron spectra were observed which were believed to arise from damped librations. A molecular dynamics simulation study of methane showed a large anisotropy and strong violation of the Cauchy relation which seemed to indicate strong angular dependent forces between molecules [89]. The adiabatic elastic constants were determined from the slope of the

calculated dispersion curves and were all lower than their measured values obtained by Brillouin spectroscopy. This discrepancy was attributed to the absence of RT coupling terms in the intermolecular potential.

The Brillouin spectroscopy of single crystals of methane and heavy methane near their triple points were reported by Rand *et al.* [90]. The ratio of acoustic velocities V_L/V_{T_1} showed an anomalously large value in $\langle 110 \rangle$ direction compared to rare gas solids. This anomaly was caused by a soft acoustic phonon and was interpreted as being indicative of RT coupling. This was confirmed by theoretical calculations of Wonneberger *et al.* [91], who studied the effect of RT coupling on the elastic constants of heavy methane. By assuming an angle and position dependent potential, they expanded the molecular and atomic densities in terms of the cubic harmonics. By calculating the coupled phonon-phonon susceptibility, they determined the elastic constants of CD_4 in good agreement with the experimental values.

A study of the behaviour of acoustic phonons on approaching the order-disorder phase transition in methane should then clarify the role of RT coupling in the dynamics of the phase transition. The phase transition in CD_4 (and probably CH_4) is presumed to be second order and must therefore be accompanied with critical effects. Such an effect has been reported in CD_4 by neutron incoherent scattering experiments [80]. Critical slowing down of orientational fluctuations has been observed near the order-disorder phase transition in CD_4 [92] [88] and are also of interest in this study. Consequently single crystals of CH_4 were cooled and Brillouin scattering

experiments were carried out as discussed in Section 5.4.

Chapter 3

Background theory

1.1 Stress, strain and elastic constant

When a body is subjected to a force, it undergoes a deformation. The amount of deformation is called the strain. In Figure 1.1, a wire of length L is stretched by a force F . The strain is defined as the ratio of the change in length to the original length. If the original length is L_0 and the stretched length is L , then the strain is given by $\epsilon = \frac{L - L_0}{L_0}$. The stress is defined as the force per unit area. If the force is F and the cross-sectional area is A , then the stress is given by $\sigma = \frac{F}{A}$. The relationship between stress and strain is called the stress-strain relationship. For a linear elastic material, the stress is directly proportional to the strain. This is known as Hooke's law. The constant of proportionality is called the elastic constant or Young's modulus, denoted by E . The relationship is given by $\sigma = E\epsilon$.

$$\sigma = E\epsilon \quad (1.1)$$

When a body is subjected to a force, it undergoes a deformation. The amount of deformation is called the strain. In Figure 1.1, a wire of length L is stretched by a force F . The strain is defined as the ratio of the change in length to the original length. If the original length is L_0 and the stretched length is L , then the strain is given by $\epsilon = \frac{L - L_0}{L_0}$. The stress is defined as the force per unit area. If the force is F and the cross-sectional area is A , then the stress is given by $\sigma = \frac{F}{A}$. The relationship between stress and strain is called the stress-strain relationship. For a linear elastic material, the stress is directly proportional to the strain. This is known as Hooke's law. The constant of proportionality is called the elastic constant or Young's modulus, denoted by E . The relationship is given by $\sigma = E\epsilon$.

Chapter 3

Background theory

3.1 Stress, strain and elastic constants

A solid body is deformed elastically when it returns to its original configuration after the removal of the stress which caused the deformation. The relation between internal stresses trying to bring the body back to equilibrium and the amount of deformation is governed by Hooke's law [93]. Under stress, a lattice point \mathbf{r} is displaced to a new position \mathbf{r}' and the displacement vector is $\mathbf{u} = \mathbf{r}' - \mathbf{r}$. If dl and dl' represent the distances between two points before and after deformation then it is straightforward to show that $dl'^2 = dl^2 + 2e_{kl}dr_k dr_l$, where for small deformations e_{kl} becomes

$$e_{kl} = \frac{1}{2} \left(\frac{\partial u_k}{\partial r_l} + \frac{\partial u_l}{\partial r_k} \right) \quad (3.1)$$

and is called the strain tensor. We note that $e_{kl} = e_{lk}$. The component of the force acting on one part of the body by the rest of it can be written as $F_i = \int_V f_i(\mathbf{r}) d^3\mathbf{r}$, where $f(\mathbf{r})$ is force per unit volume. These forces are only exerted on the surface enclosing volume V and can be expressed as a surface integral $F_i = \int_A \sigma_{ij} da_j$, where $f_i(\mathbf{r}) = \frac{\partial \sigma_{ij}}{\partial r_j}$. The quantity σ_{ij} is the i th component of the force on a unit area

perpendicular to r_j axis and is called the stress tensor. For small strain, the relation between the stress and strain is defined by Hooke's law through a 4th rank elastic constants tensor C_{ijkl} as:

$$\sigma_{ij} = C_{ijkl}e_{kl}. \quad (3.2)$$

The strain energy density of a deformed crystal is given by:

$$E = \frac{1}{2}C_{ijkl}e_{ij}e_{kl}. \quad (3.3)$$

There are 81 elastic constants in Eq. (3.2). Using symmetry relations for σ_{ij} and e_{kl} [93], the number of independent elastic constants becomes 36 and using the expression for energy density, they are further reduced to 21. For cubic crystals, the cubic symmetry reduces the number of elastic constants from 21 to 3, i.e. C_{11} , C_{12} and C_{44} . The elastic constant matrix $|C_{ij}|$ becomes

$$\begin{pmatrix} C_{11} & C_{12} & C_{12} & 0 & 0 & 0 \\ C_{12} & C_{11} & C_{12} & 0 & 0 & 0 \\ C_{12} & C_{12} & C_{11} & 0 & 0 & 0 \\ 0 & 0 & 0 & C_{44} & 0 & 0 \\ 0 & 0 & 0 & 0 & C_{44} & 0 \\ 0 & 0 & 0 & 0 & 0 & C_{44} \end{pmatrix}.$$

The elastic anisotropy is defined as:

$$A = \frac{2C_{44}}{C_{11} - C_{12}} \quad (3.4)$$

and has the value of 1 for an isotropic solid.

3.2 Propagation of elastic waves in cubic crystals

The force per unit volume $\mathbf{f}(\mathbf{r})$ and the displacement vector \mathbf{u} are related by Newton's second law of motion [94];

$$\mathbf{f} = \rho \frac{d^2 \mathbf{u}}{dt^2} \quad (3.5)$$

where ρ is the crystal density. The i th component of this equation is

$$\sum_j \frac{\partial \sigma_{ij}}{\partial x_j} = \rho \frac{d^2 u_i}{dt^2} \quad (3.6)$$

using Hooke's law and Eq. (3.5) we can write

$$\sum_{jk} C_{ijkl} \frac{\partial^2 u_l}{\partial x_j \partial x_k} = \rho \frac{d^2 u_i}{dt^2}. \quad (3.7)$$

This is the differential equation for wave propagation and has a solution of the form:

$$u_i(\mathbf{r}, t) = u_{i0} e^{i(\mathbf{q} \cdot \mathbf{r} - \omega t)} \quad (3.8)$$

where u_{i0} is the amplitude of propagation. Substituting Eq. (3.7) in Eq. (3.6) and rearranging we obtain:

$$\sum_i \left(\sum_{jk} C_{ijkl} q_j q_k - \rho \omega^2 \delta_{il} \right) u_{i0} = 0 \quad (3.9)$$

This is true if the determinant of the matrix $\sum_{jk} (C_{ijkl} q_j q_k - \rho \omega^2 \delta_{il})$ vanishes.

The solution of this secular equation yields expressions for ω^2 . There will be three roots $\omega_\mu(q)$ in general identified as ($\mu=1$) slow transverse acoustic mode, ($\mu=2$) fast transverse acoustic mode and ($\mu=3$) longitudinal mode. The equation of motion can then be written in matrix form

$$(\lambda_{ij} - \rho\omega^2\delta_{ij})u_{io} = 0 \quad (3.10)$$

where δ_{ij} is the Kronecker delta. The quantities λ_{ij} are given by

$$\lambda_{ij} = (C_{11} - C_{44})q_i^2 + C_{44}q^2 \quad (3.11)$$

if $i = j$ otherwise

$$\lambda_{ij} = (C_{12} + C_{44})q_i q_j \quad (3.12)$$

where q_i 's are the components of the \mathbf{q} vector with respect to the crystal frame of reference.

For small strain, the coupling between the strain in a crystal and the dielectric tensor is called the photoelastic effect ^[95] and is described by the equation

$$-\frac{\delta\epsilon_{ij}(\mathbf{r}, t)}{\epsilon_0^2} = P_{ijkl}e_{kl}(\mathbf{r}, t) \quad (3.13)$$

where $\epsilon_0 = n^2$ and P_{ijkl} are the elasto-optic (Pockel's) coefficients. For cubic crystals there are three independent elasto-optic coefficients P_{11} , P_{12} and P_{44} . The above equation therefore reduces to

$$-\frac{\delta\epsilon_{ij}(\mathbf{r}, t)}{\epsilon_0^2} = 2P_{44}e_{ij}(\mathbf{r}, t) + (P_{11} - P_{12} - 2P_{44})\delta_{ij}e_{ij}(\mathbf{r}, t) + P_{12}\delta_{ij}\sum_k e_{kk}(\mathbf{r}, t). \quad (3.14)$$

Consider a monochromatic light wave of the form:

$$\mathbf{E}(\mathbf{r}, t) = \mathbf{E}_0 \exp[i(\mathbf{k}_0 \cdot \mathbf{r} - \omega_0 t)] \quad (3.15)$$

incident on the scattering volume $|d\mathbf{r}|$ located at a point \mathbf{r} in the crystal, where \mathbf{E}_0 is the amplitude, ω_0 the angular frequency, $k_0 = n\omega_0/c$ the wavevector of the incident light, and c the speed of light in vacuum. This light is scattered by the fluctuations in the dielectric constant $\delta\epsilon(\mathbf{r}, t)$. Assuming $|d\mathbf{r}| \ll \lambda_0^3$ (λ_0 is the wavelength of the incident light), the far field scattered amplitude at a point \mathbf{R} is given by [94]

$$\mathbf{E}'(\mathbf{R}, t) = -\left(\frac{\omega_0}{c}\right)^2 \frac{(2\pi)^{3/2}}{4\pi R} \sum_{\mu} e^{i(\mathbf{k}' \cdot \mathbf{R} - \omega' t)} \times \hat{I}_k \times \left(\hat{I}_k \times (\delta\epsilon_{\mu}(\mathbf{q}) \cdot \mathbf{E}_0) \right) \quad (3.16)$$

where \hat{I}_k is the unit vector in the scattering direction and the fluctuations in the dielectric tensor are expressed in terms of their spatial Fourier components, viz.

$$\delta\epsilon(\mathbf{r}, t') = (2\pi)^{-3/2} \sum_{\mu} \int |d\mathbf{q}| \delta\epsilon_{\mu}(\mathbf{q}) e^{i(\mathbf{q} \cdot \mathbf{r} \mp \omega_{\mu}(\mathbf{q})t')} \quad (3.17)$$

where $\omega_{\mu}(\mathbf{q})$ is the angular frequency of the fluctuations identified as the thermal sound waves with wavevector \mathbf{q} . The index ($\mu=1,2,3$) denotes the possibility, in general, of the existence of three branches in the dispersion relation connecting $\omega_{\mu}(\mathbf{q})$ and \mathbf{q} . Also

$$\mathbf{k}' = \mathbf{k}_0 \pm \mathbf{q} \quad (3.18)$$

$$\mathbf{k}' = \frac{n}{c} [\omega_0 \pm \omega_\mu(\mathbf{q})] \hat{I}_k \quad (3.19)$$

$$\omega' = \omega_0 \pm \omega_\mu(\mathbf{q}). \quad (3.20)$$

This equation indicates that the frequency of the scattered wave is shifted by $\pm\omega_\mu(\mathbf{q})$. In quantum mechanical language one speaks of creation and annihilation of the phonons by the incident photons, whereby momentum and energy are conserved. Since the change in wavelength of light is negligibly small (in the scattering process), $|\mathbf{k}'| \cong |\mathbf{k}_0|$ and \mathbf{q} connects the two vectors and is perpendicular to the line that bisects the angle between \mathbf{k}_0 and \mathbf{k}' . It can be easily shown that

$$\omega_\mu(\mathbf{q}) = \omega' - \omega_0 = \pm \frac{2n}{c} V_\mu \omega_0 \sin(\alpha/2) \quad (3.21)$$

where α is the angle between \mathbf{k}' and \mathbf{k}_0 (i.e. the scattering angle). This equation was first obtained by Brillouin who considered the scattered light as the Doppler-shifted Bragg reflection of the incident light from thermal sound waves propagating with velocity $\pm V$ [94] [96] [35].

Taking the Fourier transform of $\delta\epsilon_{ij}$ we get

$$\delta\epsilon(\mathbf{q}, t) \cdot \mathbf{E}_0 = -i\epsilon_0^2 E_0 q u_\mu(\mathbf{q}, t) \zeta_\mu \quad (3.22)$$

where $\mathbf{u}_\mu(\mathbf{q}, t) = u_\mu(\mathbf{q}, t) \hat{\Pi}(\mathbf{q}, t)$ and

$$\zeta_\mu = \frac{P_{44}}{2} (\hat{\Pi}_\mu(\hat{\mathbf{q}} \cdot \hat{\mathbf{E}}_0) + (\hat{\Pi}_\mu \cdot \hat{\mathbf{E}}_0)\hat{\mathbf{q}}) + P_{12}(\hat{\Pi}_\mu \cdot \hat{\mathbf{q}})\hat{\mathbf{E}}_0 + (P_{11} - P_{12} - P_{44}) \sum_{x=1}^3 \hat{\Pi}_{\mu x}(\hat{\mathbf{q}})_x (\hat{\mathbf{E}}_0)_x \hat{\mathbf{x}}.$$

$\hat{\mathbf{E}}_0$ is the unit vector along \mathbf{E}_0^* i.e. along the direction of polarization of the incident light, $\hat{\Pi}_\mu$ is the unit vector in the direction of polarization of the sound waves of mode μ and $\hat{\Pi}_{\mu x}$ is the component of $\hat{\Pi}_\mu$ in the cube axis direction ($x = 1, 2, 3$). Then

$$\mathbf{E}'(\mathbf{R}, t) = - \left(\frac{\omega_0}{c} \right)^2 \frac{(2\pi)^{3/2} \epsilon_0^2}{4\pi R} \frac{1}{i} \mathbf{q} E_0 e^{i(\mathbf{q} \cdot \mathbf{R} - \omega_0 t)} u_\mu(\mathbf{q}, t) \xi_\mu \quad (3.23)$$

where $\xi_\mu = \hat{\mathbf{I}}_k \times (\hat{\mathbf{I}}_k \times \zeta_\mu)$. The average total scattered power per unit frequency interval (about ω_0), per unit solid angle, at the field point \mathbf{R} is given by

$$P(\mathbf{q}, \mathbf{R}) = \frac{c}{8\pi} \left(\frac{1}{2\pi} \int_{-\infty}^{\infty} \langle \mathbf{E}'(\mathbf{R}', t + \tau) \cdot \mathbf{E}'^*(\mathbf{R}, t) \rangle e^{i\omega'\tau} d\tau \right). \quad (3.24)$$

The bracket $\langle \rangle$ denotes the autocorrelation function of $\mathbf{E}'(\mathbf{R}, t)$. The problem is then to find the autocorrelation of the displacement vector which is

$$\langle u_\mu(\mathbf{q}, t + \tau) u_\mu(\mathbf{q}, t) \rangle = \left(\frac{V}{(2\pi)^3} \frac{K_B T}{2\rho\omega_\mu^2(\mathbf{q})} \right) e^{\pm i\omega_\mu(\mathbf{q})\tau} e^{-\Gamma_\mu(\mathbf{q})\tau}. \quad (3.25)$$

The term in the angular brackets is obtained from the equipartition theorem of harmonic oscillators and $\Gamma_\mu(\mathbf{q})$ is the decay rate of the correlation caused by the random fluctuations in the displacement vector. The final expression for $P(\mathbf{q}, \mathbf{R})$ is obtained by substituting Eq. (3.23) and Eq. (3.25) in Eq. (3.24) to obtain

$$P(\mathbf{q}, \mathbf{R}) = \frac{c}{8\pi} \left(\frac{\omega_0}{c} \right)^4 \frac{V}{4\pi^2} \frac{K_B T}{\rho R^2} \epsilon_0^4 E_0^2 \sum_{\mu} \frac{|\xi_{\mu}|^2 q^2}{\omega_{\mu}^2(\mathbf{q})} \frac{1}{2\pi} \left(\frac{\Gamma_{\mu}(\mathbf{q})}{(\omega' - \omega_0 - \omega_{\mu}(\mathbf{q}))^2 + \Gamma_{\mu}^2(\mathbf{q})} + \frac{\Gamma_{\mu}(\mathbf{q})}{(\omega' - \omega_0 + \omega_{\mu}(\mathbf{q}))^2 + \Gamma_{\mu}^2(\mathbf{q})} \right) \quad (3.26)$$

The spectrum consists of three Lorentzian doublets with frequencies $\pm\omega_{\mu}(\mathbf{q})$, with full width at half maximum intensity of $2\Gamma_{\mu}(\mathbf{q})$. The vector ξ_{μ} contains information about the polarization of the scattered light, and the squares $|\xi_{\mu}|^2$ play the role of weighting factors which determine the relative intensities of each of the three doublets. The intensity ratio of two acoustic modes, say L and T is given by

$$\frac{I_T}{I_L} = \left[\frac{\omega_L(\mathbf{q})|\xi^T|}{\omega_T(\mathbf{q})|\xi^L|} \right]^2. \quad (3.27)$$

ξ_{μ} contains all the elasto-optic coefficients and therefore by measuring the values of the intensity ratios of the Brillouin components, the ratio of these coefficients can be calculated.

3.3 Rotation-translation coupling

The interaction between molecules in a lattice depends on their intermolecular distance and the orientation of the molecules relative to one another at any given time [91]. Mathematically this can be represented as:

$$V = V(\mathbf{R}_a - \mathbf{R}_b, \omega_a, \omega_b) \quad (3.28)$$

where \mathbf{R}_a and \mathbf{R}_b are the position vectors of the centers of mass of molecules a and b and ω_a and ω_b denote the sets of three Euler angles (θ, ϕ, χ) that define the orientation of the two molecules with respect to the molecular frame of reference. For instance, if the centers of mass of the molecules attract one another via a r^{-6} potential and the atoms of adjacent molecules repel one another via a r^{-12} potential, then the interaction potential has the form:

$$V(\mathbf{R}_a - \mathbf{R}_b, \omega_a, \omega_b) = \frac{-D}{|\mathbf{R}_a - \mathbf{R}_b|^6} + \sum_{ij} \frac{C}{|\mathbf{R}_a + \mathbf{r}_{ai} - \mathbf{R}_b - \mathbf{r}_{bj}|^{12}} \quad (3.29)$$

where \mathbf{r}_{ai} is the position of atom i within molecule a , relative to the center of mass position of this molecule. The second term in Eq. (3.20) gives rise to the angle dependence of this interaction. To determine the mean value of the rotational potential $\bar{W}(\omega_a)$ experienced by molecule a , we average over the orientations of its neighbours i.e. we use the averaged potential $\bar{V}(\mathbf{R}_a - \mathbf{R}_b, \omega_a)$ which is the average angular potential seen by molecule a due to the presence of its neighbour b when this neighbour is found in all orientations with equal probability. The mean value of the rotational potential $\bar{W}(\omega_a)$ experienced by molecule a is then given by:

$$\bar{W}(\omega_a) = \int d\mathbf{R} \int d\mathbf{r} \bar{V}(\mathbf{R}, \omega_a) \rho_{NN}(\mathbf{R}) \rho(\mathbf{r}) \quad (3.30)$$

where $\mathbf{R}_a - \mathbf{R}_b = \mathbf{R}$ and \mathbf{r} denotes the position of atoms at a given site. $\rho_{NN}(\mathbf{R})$ is the density of nearest neighbours and can be expanded into cubic harmonics

$$\rho_{NN}(\mathbf{R}) = \sum_{\lambda=0}^{\infty} \sum_{\nu=0}^{2l+1} a_{\lambda\nu}(\mathbf{R}) K_{\lambda\nu}(\vartheta_R, \varphi_R) \quad (3.31)$$

such that ϑ_R and φ_R denote the polar coordinates for the nearest neighbour molecules. Cubic harmonics are surface harmonic functions that transform in simple ways under the operation of the cubic group. Similarly the density of atoms of molecule a is expanded into cubic harmonics in the frame rotating with the molecule and then transformed into the crystal frame by means of the rotator functions $U_{m''m'}^{(l')}(w_a)$

$$\rho(\mathbf{r}) = \sum_{l'=0}^{\infty} \sum_{m',m''=1}^{2l'+1} b_{l'm'}(\mathbf{r}) K_{l'm''}(\vartheta_r, \varphi_r) U_{m''m'}^{(l')}(w_a) \quad (3.32)$$

where ϑ_r and φ_r define the polar coordinates of the atoms in the molecular frame at a given site. Some of the coefficients in the expansion of the densities are zero due to molecular and site symmetry considerations depending on the particular material under investigation.

Let us consider three lattice modes ($\mu = 1, 2, 3$) with displacements

$$\mathbf{u}_\mu(\mathbf{R}) = -\tilde{u}(\mathbf{q}_\mu) \hat{e}_\mu(\mathbf{q}_\mu) (2/N)^{\frac{1}{2}} \sin(\mathbf{q}_\mu \cdot \mathbf{R}) \quad (3.33)$$

where \mathbf{q}_μ is the wavevector for propagation and \hat{e}_μ is the unit vector for the polarization of mode μ . The displaced positions $\mathbf{R} + \mathbf{u}_\mu(\mathbf{R})$ of the neighbours of molecule n are inserted into (3.29) and (3.30) and the terms that are linear in the displacement are isolated for each of the three lattice modes μ . The bilinear coupling term involving the rotational and translational variables resembles

$$W_{uR}(\mathbf{q}_\mu, \omega_n) = -C\tilde{u}(\mathbf{q}_\mu) W_n(\mathbf{q}_\mu) R^l(\omega_n) \quad (3.34)$$

where $R^l(\omega_n)$ denotes the operator acting on the angular variables of the molecule n and $W_n(\mathbf{q}_\mu)$ is the coupling constant.

The coupling term in the Hamiltonian is obtained by summing the above equation over all the N rotating molecules

$$H_{uR} = -C\tilde{u}(\mathbf{q}_\mu) \sum_{n=1}^N W_n(\mathbf{q}_\mu) R^i(\omega_n). \quad (3.35)$$

In general, the Hamiltonian for an interacting system has the form [27]

$$H_0 = \sum_{i\alpha} H_\alpha(Q_{i\alpha}) - \frac{1}{2} \sum_{i\alpha, j\beta} W_{i\alpha, j\beta} Q_{i\alpha} Q_{j\beta} \quad (3.36)$$

where the generalized coordinates $Q_{i\alpha}$ are the α th coordinate for the i th molecule and may represent translational or rotational motion.

If we examine, using linear response theory, the response of this interacting system to an external perturbation $U_{j\beta}(t)$ on operators $Q_{j\beta}$ of this system, an expression for the generalized susceptibilities $\chi_{\alpha\beta}(\mathbf{q}_\mu, \omega)$ of the coupled system can be obtained as follows:

$$\chi_{\alpha\beta}(\mathbf{q}_\mu, \omega) = [1 - \chi(\mathbf{q}_\mu, \omega)W]_{\alpha\beta}^{-1} \chi_\beta(\mathbf{q}_\mu, \omega) \quad (3.37)$$

where W is the coupling matrix in Eq. (3.35) and $\chi(\mathbf{q}_\mu, \omega)$ is the diagonal matrix of the susceptibilities of the single degrees of freedom and $\chi_\beta(\mathbf{q}_\mu, \omega)$ is the susceptibility of a single degree of freedom (either rotational or translational). Now if we consider the problem of one phonon coupled to N rotating molecules in the crystal, H_0 can be written as $H_0 = H_u + H_R + H_{uR}$ where H_{uR} is the coupling term which we get from Eq. (3.34). The coupled phonon-phonon susceptibility can therefore be calculated from Eq. (3.36) as:

$$\chi_{uu}(\mathbf{q}_\mu, \omega) = \chi_u(\mathbf{q}_\mu, \omega) \left(1 - \chi_u(\mathbf{q}_\mu, \omega) \chi_{R^i}(\omega) C^2 \sum_{n=1}^N W_n^2(\mathbf{q}_\mu) \right)^{-1} \quad (3.38)$$

where $\chi_u(\mathbf{q}_\mu, \omega)$ is the phonon susceptibility. Now the sound velocity is given by

$$v_\mu^2 = \lim_{q \rightarrow 0} \lim_{\omega \rightarrow 0} (\chi_{uu}(\mathbf{q}_\mu, \omega) q^2 m)^{-1}. \quad (3.39)$$

Putting Eq. (3.37) into Eq. (3.38) and replacing $\lim_{q \rightarrow 0} \lim_{\omega \rightarrow 0} \chi_u(\mathbf{q}_\mu, \omega)$ by the uncoupled elastic constants ($C_{11}^o, C_{12}^o, C_{44}^o$), we find the following relations between the “coupled” and “uncoupled” elastic constants;

$$C_{11} = C_{11}^o - \frac{1}{mq^2} \chi_{R^l}(0) C^2 W_1^2 \quad (3.40)$$

$$C_{44} = C_{44}^o - \frac{1}{mq^2} \chi_{R^l}(0) C^2 W_3^2 \quad (3.41)$$

$$C_{12} = C_{12}^o + \frac{1}{mq^2} \chi_{R^l}(0) C^2 W_2^2 \quad (3.42)$$

where W_1^2, W_2^2 and W_3^2 are the low frequency and wavevector limits of $\sum_{n=1}^N W_n^2(\mathbf{q}_\mu)$ for appropriate wavevector and polarization directions that result in the three elastic constants. These equations indicate the possible effect of RT coupling on the elastic constants, i.e. decrease in C_{11} and C_{44} and particularly $C_{11} - C_{12}$ given by:

$$C_{11} - C_{12} = C_{11}^o - C_{12}^o - \frac{1}{mq^2} \chi_{R^l}(0) C^2 (W_1^2 + W_2^2) \quad (3.43)$$

3.4 Euler angles

The three Euler angles are defined in the standard way as ϕ about the body z axis, θ about the line of nodes and χ about the body z axis, where all the rotations are counterclockwise [97]. The rotation matrix from the body to the space coordinate system then is given by:

$$R = \begin{pmatrix} \cos \chi \cos \phi - \cos \theta \sin \phi \sin \chi & -\sin \chi \cos \phi - \cos \theta \sin \phi \sin \chi & \sin \theta \sin \phi \\ \cos \chi \sin \phi + \cos \theta \cos \phi \sin \chi & -\sin \chi \sin \phi + \cos \theta \cos \phi \cos \chi & -\sin \theta \cos \phi \\ -\sin \chi \sin \theta & \cos \chi \sin \theta & \cos \theta \end{pmatrix}.$$

A vector \mathbf{X} in the body frame of reference can be transformed to the space frame of reference \mathbf{X}' by $\mathbf{X}' = R\mathbf{X}$, where \mathbf{X} and \mathbf{X}' can be expressed as column matrices of the form $\begin{bmatrix} a \\ b \\ c \end{bmatrix}$ such that a , b , and c are constants.

Euler angles are calculated in the present experiment to determine the orientation of crystal axes with respect to the laboratory frame of reference. The sound wave vector \mathbf{q} which is known in the laboratory frame of reference (due to the choice of scattering geometry $q_y = \frac{1}{\sqrt{2}}$ and $q_z = -\frac{1}{\sqrt{2}}$) is then be transformed to the body (crystal) frame of reference with respect to which the elastic constants are to be determined.

Chapter 4

Experimental arrangements and procedure

4.1 Experimental setup

The experimental arrangement for Brillouin scattering studies of transparent single crystals is shown in Fig. 4.1. A single mode Argon-ion laser beam was focused along the axis of the cell inside a cryostat. The scattered beam was analyzed at 90° by a Brillouin spectrometer using Fabry-Perot interferometry and photon counting and stabilization techniques. X-rays were used to obtain Laue diffraction photographs of the crystals and to determine their orientations. A He-Ne laser beam defined the optic axis. The laboratory frame of reference (XYZ) is also shown in Fig. 4.1

4.2 Laser

Highly monochromatic laser radiation is necessary in the technique of Brillouin spectroscopy. A single mode argon ion laser (Spectra Physics 165-08) was used in this experiment. The output of the laser cavity was tuned to 514.5 nm wavelength with an intracavity prism. Several longitudinal modes satisfying the resonance condition

exist within the Doppler broadened output. A highly stable temperature controlled Fabry-Perot etalon inserted in the cavity was used to isolate one of the longitudinal modes. Frequency stability of the laser depends on temperature changes of the cavity length i.e. mechanical shifts and 'jitter'. Mechanical stability was achieved by mounting the laser on a steel table bearing a large "floating" granite block which was isolated from the floor by rubber mountings. Jitter, mainly caused by the flow of cooling water, was always present and limited the resolution in this experiment to about 10-15 MHz. The output of the laser was generally reduced in power to 20 mW using neutral density filters to prevent the crystals from being destroyed by heating effects.

4.3 The Brillouin spectrometer

4.3.1 Fabry-Perot interferometer

The Brillouin spectrometer consisted of a piezoelectrically scanned multipass Fabry-Perot interferometer, a photomultiplier tube, an amplifier/discriminator, and a data acquisition and stabilization system DAS-1 coupled via several lenses and apertures.

The plane Fabry-Perot interferometer consists of an optical cavity formed by two parallel plates (mirrors) separated by a distance d [98] [99]. The inner surfaces of the mirrors are flat to $\lambda/200$ (in this experiment) and are coated with highly reflective films. The front mirror was manually adjustable on a mount using three extremely fine micrometer screws. The rear mirror is mounted on three piezoelectric transducers in a triangular geometry [100]. When a beam of light is incident on the Fabry-Perot

parallel to the optic axis, only those wavelengths pass through which satisfy the resonance condition of the cavity i.e.

$$2nd = m\lambda \quad (4.1)$$

where n is the refractive index of the medium in the cavity ($n = 1$ for air). By moving one of the mirrors, d can be changed and different wavelengths can be scanned. The range of wavelengths between two consecutive orders of interference is called the Free Spectral Range (SFR) of the Fabry-Perot and is given by

$$SFR = \frac{c}{2d} \quad (4.2)$$

where c is the speed of light in the medium. The Fabry-Perot interferometer therefore acts as a highly tunable frequency filter.

Another important characteristics of the Fabry-Perot is the Finesse, F , defined by the expression

$$F = \frac{SFR}{FWHM} \quad (4.3)$$

where $FWHM$ stands for full-width at half-maximum of a fringe. Therefore a higher finesse indicates the ability of the spectrometer to better resolve closely spaced lines. For high values of finesse, a number of limiting factors must be considered including the flatness of the mirrors, the reflectivity of the mirrors and the diffraction at the pinhole A4. Each time the SFR was changed the size of this pinhole needed to be adjusted so as to establish a balance between the gain in effective finesse and loss of intensity. Pinhole sizes of 600-1000 microns were used for SFR s in the range of 7.19 GHz-16.43 GHz in the present experiment.

Also of importance is the Contrast, defined by the ratio of maximum to minimum transmission intensity and defines the ability of the spectrometer to detect very weak signals. To observe weak spectral features i.e. weak transverse components, a triple pass Fabry-Perot interferometer was used. This was achieved by rotating the retroreflectors into a three pass mode. Retroreflectors are corner cubes consisting of three mutually perpendicular mirrors joined together to form a corner. A beam of light reflected once from each internal surface of a corner suffers a translational shift and a reversal in direction. Triple passing cubes the contrast, increases the finesse but decreases the throughput. By properly choosing the reflectivity coefficient of the mirrors, it is possible to balance between the loss in throughput and the gain of finesse. In this experiment mirrors of 93% reflectivity were used. This limited the effective finesse to about 60 and contrast to about 10^5 .

4.3.2 Data acquisition and stabilization system

The Data Acquisition and Stabilization system (DAS-1) performed several functions ^[101]:

i) It employed a 1024 channel multichannel analyzer to store digital data generated by the light transmitted through the Fabry-Perot into the phototube and displayed the resultant spectrum on its CRT screen. A cursor was used to address a particular channel. The channel number and the corresponding photon counts were displayed on the screen.

ii) It provided a simultaneous ramp voltage to the three piezoelectric transducers in order to scan the rear mirror of the Fabry-Perot interferometer. A digital clock

generated a series of pulses (ramp voltage) of equal magnitude and duration which were amplified and integrated up to 1000 V by a high voltage operational amplifier and applied to the three piezoelectric elements to scan the rear mirror. The clock sequentially addressed the channel address scaler of the 1024 channels of the multi-channel analyzer. Therefore there was a direct correspondence between the channel number, the voltage and the frequency. The scanning time could be varied from 0.01 ms to 99.99 ms in steps of 0.01 ms per channel. There was a flyback time of 2 ms between the scans to allow for the relaxation and adjustment of the piezoelectric elements and the Fabry-Perot mirrors.

iii) A drift stabilization system was incorporated to correct for the frequency drifts due to temperature changes in the laser cavity and the Fabry-Perot cavity. Frequency stabilization was achieved by setting a particular channel as the reference channel (500 in this experiment) displayed on the DAS screen by a vertical bar. Two other channels which defined the drift stabilization width were symmetrically situated about the reference channel and displayed as vertical bars. The reference channel was locked to a strong spectral feature by manually adjusting the zero level of the ramp scaler. The number of counts on either side of the reference channel was stored in two digital registers A and B. The contents of the registers were compared and if one was smaller than the other, a correction voltage was automatically applied to the ramp scaler (during flyback) to bring the peak back towards the reference channel.

iv) The DAS-1 also maximized the finesse. The finesse optimizer improved any

misalignment in the mirrors due to temperature changes or mechanical relaxation. A window, generally of 5-7 channels, was set symmetrically, within the drift stabilization windows, about the reference channel. The counts in this window were stored in a register and maximized during a four sweep cycle. During the first sweep the contents of the register were stored. Next a test voltage was applied to the three piezoelectric elements to tilt the mirror about the vertical axes. Counts were compared and appropriate correction voltages were applied to the piezoelectric transducers to tilt the mirror so as to increase the number of counts. During the other two sweeps, the mirror was tilted about the horizontal axis to improve the counts.

v) The segmented ramp feature of the DAS allowed for spending more time (up to 100 times more) in accumulating counts in selected portions of the spectrum. This is very important when studying weak spectral features eg. weak transverse components.

4.3.3 Optical setup and alignment

The optical arrangement is explained in detail elsewhere^[102] and is shown in Fig. 4.1.

A He-Ne laser beam defined the horizontal optic axis of the Brillouin spectrometer. This was taken to be the Y axis of the laboratory frame of reference. The Z axis was defined along the vertical axis of the cell. The argon-ion laser beam was polarized along the X axis. This beam was focused by a high quality quartz lens L1 (focal length 30 cm) at 4 mm above the bottom plug inside the cell via a high quality mirror M which deflected the beam upwards. Apertures A1 and A2 were mainly placed to



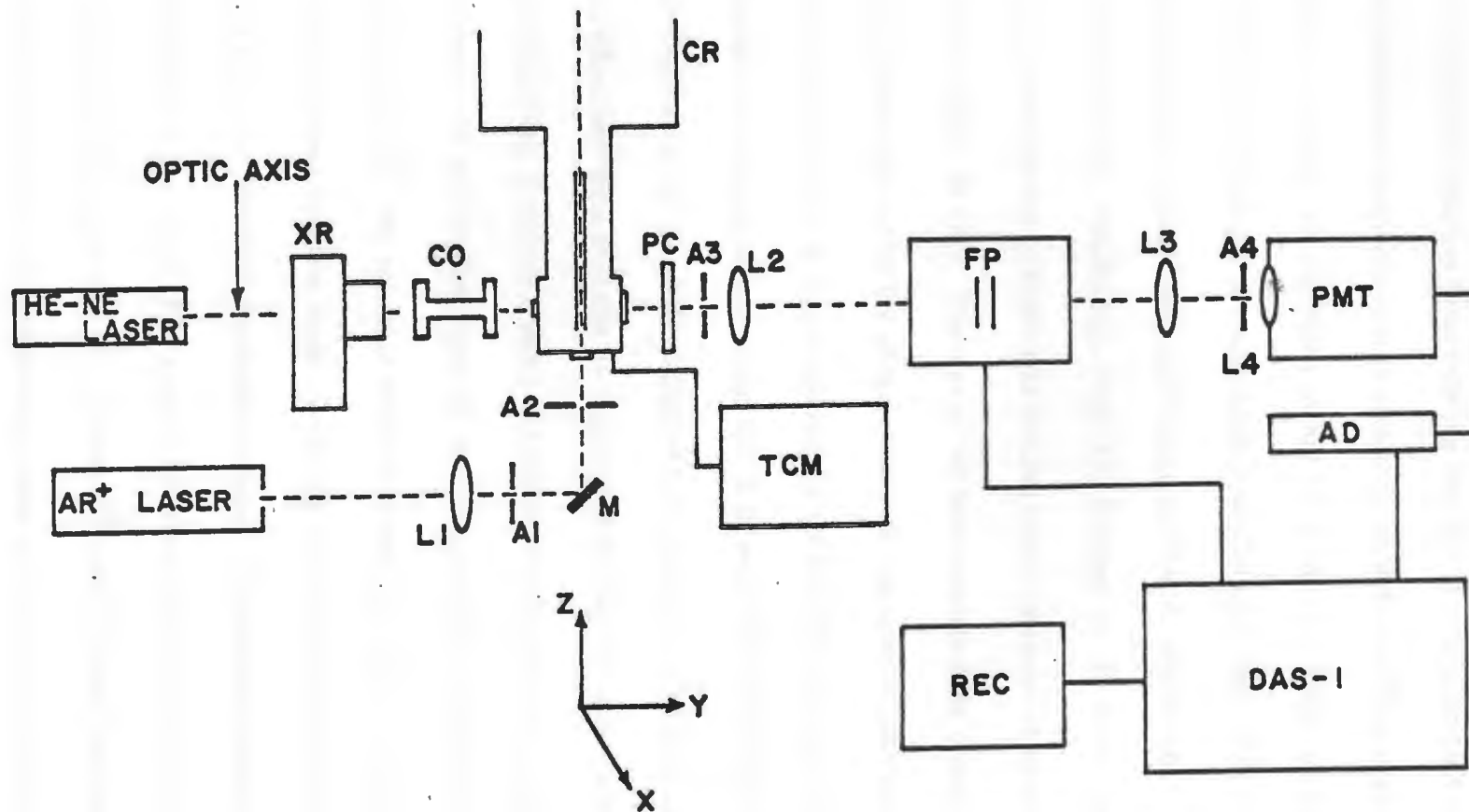


Figure 4.1: The optical arrangement

block unwanted radiation from entering the cell. It was important that the two laser beams be exactly perpendicular to each other to define a 90° geometry. A pentaprism was used to ensure this condition within $15'$ error. The scattered light, after passing through a 6 mm pinhole A3, was rendered parallel by another high quality quartz lens L2 (focal length 45 cm) which was focused on the cell axis at about 4 mm above the bottom of the cell. Parallel rays were then incident on the Fabry-Perot front mirror. The output of the Fabry-Perot was focused onto a pinhole A4 by a high quality lens L3 (focal length 80 cm). The size of A4 was important as noted in Section 4.3.1. The light was collected by the photocathode of a photomultiplier tube (ITT FW 130) which was mounted in a thermoelectrically cooled RF shielded chamber to cool the photocathode temperature to about 250 K in order to reduce the dark count of the tube. The output of the photomultiplier tube was fed to the Amplifier/discriminator which effectively separated the photopulses from the tube noise (and other electronic instabilities) and produced a series of identical 1 volt pulses at a rate proportional to the intensity of the incident light on the photocathode. This constituted the input signal to the DAS. The resultant dark count was less than 1 count/sec.

The alignment was first made by passing the He-Ne beam first through the apertures A3 and A4. The photomultiplier tube was centered and placed perpendicular to the direction of the beam. The x-ray collimator was added and adjusted so that the beam passed exactly through the pinholes. The Fabry-Perot was then placed in position and its four leveling screws were adjusted until the beam entered and left through

the center of its aperture when operated in the single pass mode. The Fabry-Perot mirrors were made perpendicular to the beam by making the back reflection off the front mirror to coincide with the He-Ne incident beam. Lens L2 was placed and adjusted so that it backreflected the beam on itself and sent a parallel beam through the Fabry-Perot. Lens L3 was placed so that the output of the Fabry-Perot passed through pinhole A4 in both the single as well as the triple pass mode. A card was placed at the intersection of the two laser beams and the optical system was aligned by observing the scattering from the card. The Fabry-perot front mirrors were adjusted (with the two adjusting screws) until a flashing spot was seen at the exit of the Fabry-Perot. The Fabry-Perot piezoelectric bias controls on DAS-1 were adjusted (and again the lenses were adjusted) to maximize the signal. Adjustment of L2 was done at this point in the absence of A4. The corner cubes were then rotated into three-pass position and the bias controls and lenses were finely adjusted to maximize the intensity of the scattered light received by the phototube. A4 was then replaced and final adjustments were made with L3. The plates of the Fabry-Perot were then almost exactly parallel. Once the optics was optimized the card was replaced by the cryostat and the spectrum was recorded with the DAS-1 in the stabilization and optimization modes.

4.4 Cryostat, cell and temperature control

Two different cryostats were used in this experiment. For CO , O_2 and CH_4 samples, a liquid helium cryostat was used in order to achieve temperatures as low as 10 K.

For cyclooctane samples, a thermoelectric cryostat was used which provided for temperatures between the room temperature and as low as 173 K. A description of each cryostat, cell and the respective temperature control unit is presented in the following two sections.

4.4.1 Liquid helium cryostat

A modified commercial liquid helium cryostat (Janis Research Co. Model 10DT) was used in this experiment to achieve low temperatures. This cryostat has been described in detail elsewhere ^[102] and a brief description is presented here. The cryostat is shown in Fig. 4.2

The outer body (26) was made of thin stainless steel. It contained two reservoirs: a five litre reservoir for liquid nitrogen (8) which was automatically refilled every 6 hours from a 200 litre liquid nitrogen tank and controlled by a liquid level sensor (High Vacuum Equipment Co., Model ME 77), and a 7 litre reservoir for liquid helium (9) which was filled every two days from a 60 litre liquid helium tank via an inlet (6) and monitored by a liquid helium level indicator (American Mag. Inc., Model KE 101). These reservoirs were highly polished to reduce heat transfer by radiation into the cell area.

The cell (16), soldered to a long stainless steel tube, was suspended in the central bore of the cryostat and centered vertically by a teflon spacer (21). The top part of it was connected to a brass tube (1) through which the sample was entered the cell. The rotation of the cell was carried through rotary seals (29), (31) with a scale to

read the degree of rotation. The liquid helium from the reservoir (9), after passing through the capillary tube (22) reached the heat exchanger (20). A needle valve (23), having a control knob (28) at the top, regulated the flow of the helium. Liquid helium, after arriving at the bottom of the heat exchanger, was vapourized and the cool vapour circulated upward to escape through the outlet (4) into the helium return system. Two brass rods were projected downwards from the bottom sides of the heat exchanger and served as the cold finger. These were connected to the copper braids from the cell (19). A heater (12) was used to control the temperature of the cold finger in conjunction with a GaAs(Si) temperature sensor and proportional control circuit. There were two aluminum shields surrounding the cell. The inner shield (13) was maintained at the same temperature as the heat exchanger and the outer shield (10) at liquid nitrogen temperature. Plexiglass windows on these shields reduced radiative heating effects and prevented the formation of 'hot' spots inside the cell. There were windows around the cell, one made of quartz (17) through which the laser beam entered. The window (15) through which the scattered light passed and a smaller window (18) were made of plexiglass to allow x-ray transmission. The cryostat rested on an aluminum plate which could be adjusted by means of three leveling screws. The plate was finely adjustable allowing for the cryostat to be moved across the beam.

The cell region is easily accessible by removing the tail section of the cryostat. The cell, shown in Fig. 4.3, was a quartz tube of inner diameter 3 mm and outer diameter 5 mm and length of about 2 cm and was fitted with a quartz-to-Kovar graded seal at



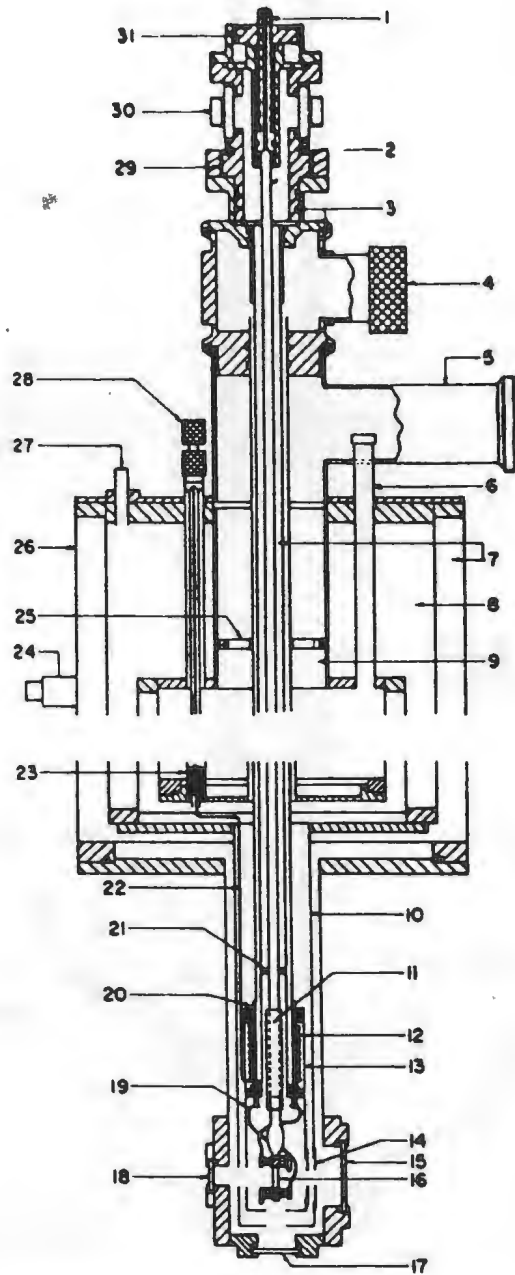
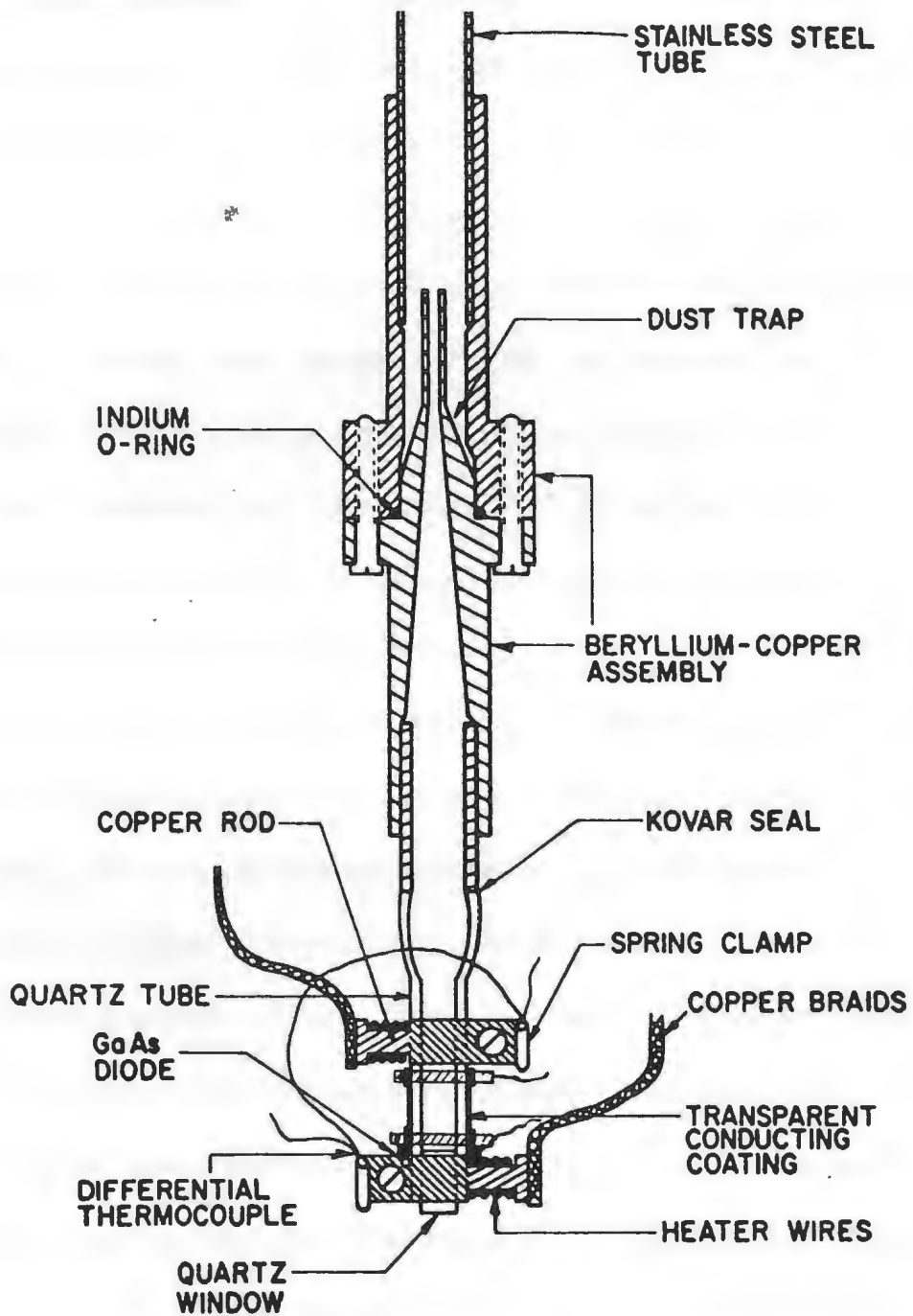


Figure 4.2: The top and the tail section of the cryostat



SAMPLE CELL

Figure 4.3: The sample cell

the top. A dust trap between the cell and the inlet tube prevented dust particles from settling at the bottom of the cell. The bottom of the cell was closed by a polished fused quartz plug glued to the cell with epoxy resin. A phosphor bronze clip was clamped to the lowest part of the cell. This clamp had miniature GaAs (Si) diodes mounted on it. One side of the clamp was folded to provide housing for a differential thermocouple. Another clamp was fastened to the cell above the first and provided for the second junction of the thermocouple. To each clamp, two copper rods were soldered and joined to one end of a copper braid. The other end of the copper braid was connected to the cold finger of the heat exchanger. Wires wound on each rod provide for the control of the cell temperature.

A unique and crucial feature of the cell was the deposition of a thin, optically transparent, electrically conducting coating on the cell body between the clamps. The film has a 70% optical transmission coefficient and 10 ohms electrical resistance and is about 1 cm high. Two thin brass clamps, lined inside with indium, were used for electrical contact to the film. Teflon rings were used to isolate these clamps from the rest of the system (i.e. from the above mentioned phosphor bronze cooling clamps). This film was used when the crystals were being cooled i.e. electrical current was passed through the film to heat the walls of the cell and release the crystals from it. In this way free standing crystals could be obtained and then cooled without shattering.

The cell temperature was controlled in four stages:

- i) The external automatically controlled needle valve regulated the rate of flow of liquid helium in the heat exchanger.
- ii) Temperature at the bottom of the can was finely controlled to about 4 K below cell temperature by a GaAs diode sensor in conjunction with a temperature indicator/controller (Lake Shore Cryotronics, Inc., Model DTC-500) and heater wires. The temperature indicator/controller provided a direct current of $10 \mu\text{A}$ through the diode. The forward voltage of GaAs diodes increases with the decrease in temperature. The temperature controller compared the voltage across the diode with a highly stable set-point voltage. The resulting error signal was amplified by the unit and was used to regulate the amount of current through the heater wires.
- iii) Temperature at the bottom of the cell was controlled using a similar proportional electronic control assembly to within 0.01 K.
- iv) Temperature at the top of the cell and hence temperature gradient in cell (as measured by a Keithly Instruments microvoltmeter, Model 150B) was controlled via differential thermocouple and heater proportional control system. The current to the cell heater wires was divided unequally between the heaters at the top and bottom of the cell by means of a potentiometer with the top hotter than the bottom of the cell and was completely adjustable.

4.4.2 Thermoelectric cryostat

The details of the cryostat for the second setup is shown in Fig. 4.4. This cryostat was built and designed by S. W. Breckon^[103]. The outer body of the cryostat (5) was



Figure 1. Diagram of the assembly

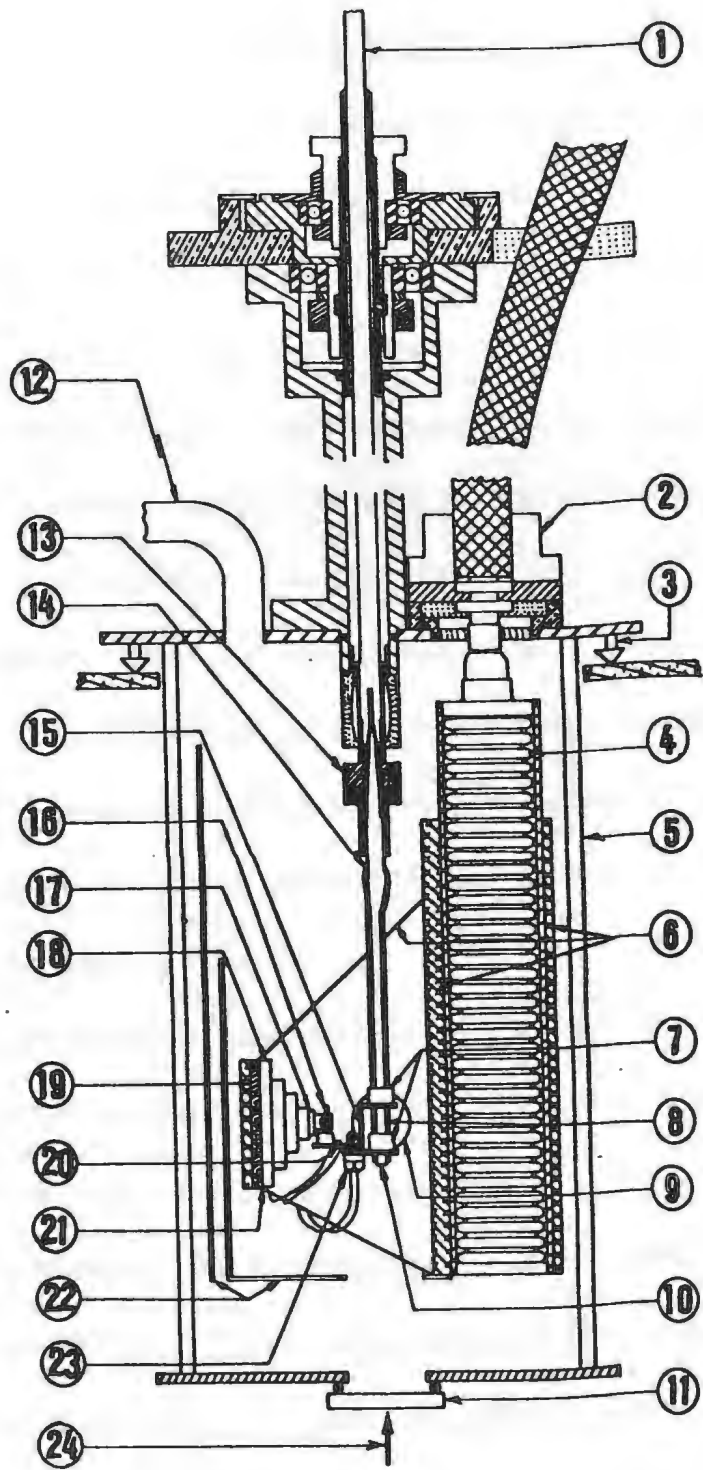


Figure 4.4: Cryostat and the cell assembly

made of acrylic tube of 12.5 cm diameter. A fused quartz cell (8) of inner diameter of 3 mm and outer diameter of 5 mm was suspended through the center of the cryostat and was connected at the top to a stainless steel tube (1) via a quartz-to-Kovar seal (14) through which the sample was introduced into the cell. A fused quartz plug (10) was sealed into the bottom of the cell by means of epoxy and provided for the entry of the laser beam into the cell. Again a brass dust trap assembly (13) was placed inside the cell to prevent dust particles from settling on the quartz plug. The cell was capable of rotating about its axis via vacuum tight rotary seals at the top of the cryostat and the amount of rotation could be read on a graduated scale. The cryostat could move vertically as well as horizontally with the help of fine adjusting screws. This allowed for accurate positioning of the cryostat so that the laser beam (24) passed exactly through the center of the cell via a quartz window (11) at the bottom of the cryostat.

Plexiglass windows (9) were used for X-ray and light scattering purposes. The cell was surrounded by aluminum shields (22) to reduce external radiation affects. The cryostat was kept under vacuum via an outlet (12) to rotary and diffusion vacuum pumps. The cold surface of a four stage thermoelectric module (18) was soldered to copper pieces (17) which in turn were soldered to a two-armed silver strip (15). The arms were 10 mm apart and made good thermal contact to the cell with the help of two copper rings (7) encasing a set of phosphor bronze spring ribbons thereby allowing for complete rotation of the cell. The hot end of the module was thermally

connected to the cooling head (4) of an immersion refrigeration system (Neslab PBC-4) by soldering to a thick copper plate (19) which was screwed and butted, using thermal grease, to an aluminum block (6) forming part of the cooler head. The Neslab cooler head (4) was placed inside the cryostat through a vacuum tight hose entry unit (2). A GaAs diode sensor (23) was mounted on the silver strip (15) near the bottom of the cell along with heater wires (20) of 50Ω resistance. A copper constantan thermocouple (16) was used to monitor the vertical temperature gradient in the cell.

The cell temperature was controlled in three stages:

- i) The temperature of the hot end of the thermomodule could be controlled to as low as 235 K by controlling the rate of flow of refrigerant through the Neslab cooler head (4). This was achieved automatically by a home made pulse generator. The frequency and the length of the pulse could be set externally to allow for enough refrigerant to pass through the cooler head (4) and maintain the temperature of the hot end of the thermomodule at the desired value. A copper constantan thermocouple monitored the temperature at the module interface.
- ii) A direct current was passed through the thermomodule to establish a temperature difference between the two ends of the module (Peltier effect). In this experiment a current of about 2 A was passed through the four stage thermomodule to attain temperatures as low as 170 K. The current could be varied externally to achieve intermediate temperatures.

iii) The temperature of the cell was accurately monitored and controlled utilizing the GaAs diode sensor and heater wires in conjunction with a cryogenics temperature controller (Thor 3010 II). The function of this unit is very similar to the one used in the previous setup for measuring and controlling the temperature of the cell to an accuracy of 0.04 K.

4.5 Single crystal growth and cooling

The single crystals were basically grown by Bridgman's method [104]. This method involved slow solidification from the liquid at the triple point in presence of a fixed temperature gradient.

In cases of carbon monoxide, oxygen, and methane, gas samples were put into the cell and the cell was flushed and pumped out several times to remove possible impurities. The cryostat was precooled for a day by allowing liquid nitrogen into the cryostat. Liquid helium was then transferred into the appropriate space in the cryostat. The temperature of the cell was lowered by adjusting the needle valve until liquid was formed. This liquid was further cooled to about 1 K above the triple point.

For growing cyclooctane single crystals, liquid samples were used. The cyclooctane samples were probed with a cadmium laser beam to check for any luminescence due to impurities and dust particles in the cell. The liquid was cooled to 1 K above the triple point temperature by controlling the rate at which refrigerant would flow through the Neslab cooler head.

The crystals were generally grown by lowering the temperature of the cell very

slowly by 0.05-0.1 K per hour while an upward temperature gradient of about 2 K was maintained between the top and bottom of the cell until a small seed of about 0.05 mm was formed on the window of the cell. The seed was annealed overnight and the resulting sample* was grown to height of 1 cm at the rate of 0.3 mm/h. X-ray diffraction photographs were taken to ensure that the crystal was single and of good quality. Strained samples were easily recognized by the streaked nature of the Laue spots. Polycrystalline samples were readily identified by the presence of twin or multiple Laue spots forming too many crystallographic zones. Strained or polycrystalline samples were melted completely and grown again. A success rate of about 1 in 3 was achieved after initial trials with each sample substance.

Single crystals of good quality were then ready for cooling. Cooling van der Waals solids was very difficult. These solids have a very high coefficient of thermal expansion and prefer to stick to the walls of the cell and hence shatter easily on cooling. Previously no one had been able to consistently cool these single crystals in an optical system, and hence Brillouin scattering experiments on cooled single crystals have not been performed in the past. In case of carbon monoxide, oxygen, and methane crystal samples, any remaining liquid was first removed by slow pumping on the cell using a rotary pump. The film voltage was then raised in steps of 10 mV to melt the solid from the sides while carefully and periodically pumping to remove the resulting melt. The result was a dome-shaped crystal released from the sides of the cell. Once the crystal was freed from the sides, the temperature of the cell was lowered

automatically by about 8 K per hour to any desired temperature. Occasionally the crystal grew on the sides and the cooling process had to be stopped and the rate of pumping was increased slightly. The cooling process was therefore a delicate balance between the rate of pumping, the rate of cooling and the rate at which the film voltage was increased. Care was also taken not to pump on the cell for too long (greater than two hours) because of the effect of cryopumping resulting in oil particles moving towards the cell. Once the desired temperature was achieved, the pumping and cooling were stopped and the crystal was allowed to grow on the sides. The film voltage was lowered in steps of 10 mV per hour to avoid nonequilibrium temperature changes. Cyclooctane crystals were cooled manually by lowering the temperature of the cell by 20 K in three days.

Laue x-ray diffraction patterns were then taken to ascertain that the crystal was still single and of the same orientation. If the orientation was different due to rotation of the crystal in the cell (which sometimes occurred), the new orientations were determined before performing Brillouin scattering experiments. The cooling procedure was almost always successful although occasionally the crystals became too small due to the necessary pumping and a new crystal had to be regrown.

4.6 X-ray crystal orientation procedure

The x-ray source used in this experiment was a Philips MO 100/Be 100 KV beryllium window tube operated at 70 KV and 10 mA current. The beam was passed through a lead collimator in alignment with the optic axis. The collimated x-ray beam was

passed through the crystal and the Laue diffraction pattern was recorded on Polaroid 57 film in a XR-7 Land camera. The camera was placed perpendicular to the direction of the incident x-rays and 8.4 cm away from the center of the cell. Transmission Laue x-ray diffraction usually consists of a central bright spot (due to the undiffracted beam) and several other spots of varying intensities. The diffraction pattern is used to determine the quality and the orientation of the crystals. The quality refers to whether the crystal is a strain-free single crystal or a polycrystalline sample. Single crystals give rise to well defined elliptically shaped spots. Distorted Laue spots mean that the crystal is strained.

The orientation refers to how the crystal axes are situated relative to the laboratory frame of reference and is expressed in terms of the Euler angles (θ, ϕ, χ) . The orientation procedure has been completely computerized [105] and is based on the technique of stereographic projection [106]. The measured coordinates of the Laue spots (x_i, z_i) are put into the program. Each Laue spot represents a particular crystal plane. The direction cosines (X_i, Y_i, Z_i) of the normal to the crystal planes are calculated from elementary geometry using the following expressions:

$$X_i = \frac{x_i}{r_i \sqrt{2}} \left(1 + \frac{D}{\sqrt{r_i^2 + D^2}}\right)^{1/2} \quad (4.4)$$

$$Y_i = \frac{1}{\sqrt{2}} \left(1 - \frac{D}{\sqrt{r_i^2 + D^2}}\right)^{1/2} \quad (4.5)$$

$$Z_i = \frac{z_i}{r_i \sqrt{2}} \left(1 + \frac{D}{\sqrt{r_i^2 + D^2}}\right)^{1/2} \quad (4.6)$$

where $r_i = \sqrt{x_i^2 + z_i^2}$ and D is the crystal to film distance.

The direction cosines of the normal to a plane are related to the Miller indices of the plane (h, k, l) by the following relation:

$$\begin{pmatrix} X_i \\ Y_i \\ Z_i \end{pmatrix} = S_i R Q^{-1} \begin{pmatrix} h_i \\ k_i \\ l_i \end{pmatrix} \quad (4.7)$$

where S is the interplanar spacing for planes of the form $\{hkl\}$ and for cubic crystals is given by the expression

$$S = \frac{a_0}{\sqrt{h^2 + k^2 + l^2}}$$

Q is the structure matrix which for cubic crystals is given by

$$Q = \begin{pmatrix} a_0 & 0 & 0 \\ 0 & a_0 & 0 \\ 0 & 0 & a_0 \end{pmatrix},$$

and R is the rotation matrix which transforms a vector from the body to the laboratory coordinate system; it is expressed in terms of the Euler angles as explained in the Section 3.4. a_0 is the lattice constant for cubic crystals.

Interplanar angles were first calculated using known values of direction cosines.

The dot product between the normal to two planes is:

$$(X_1, Y_1, Z_1) \begin{pmatrix} X_2 \\ Y_2 \\ Z_2 \end{pmatrix} = S_1 S_2 (h_1, k_1, l_1) (Q Q^\dagger)^{-1} \begin{pmatrix} h_2 \\ k_2 \\ l_2 \end{pmatrix} \quad (4.8)$$

Miller indices were then assigned from a list of indices to the first three Laue spots (not lying in the same crystallographic zone) on a trial and error basis so as to satisfy the dot product between the normal to any two planes. An error of 2° was generally allowed in the interplanar angles. Once the Miller indices were assigned to Laue spots, an approximate rotation matrix and Euler angles were calculated. The

trial and error procedure generates several sets of Euler angles allowed within the specified error in the interplanar angle. These approximate Euler angles were then used to assign Miller indices to the remaining Laue spots on the photograph. The final version of the rotation matrix and the Euler angles was calculated by a least squares fitting procedure [105]. The Euler angles thus calculated were correct within $\pm 0.5^\circ$.

The crystal was then rotated about the cell axis by a finite amount and the Laue photograph was taken again. Rotation of the crystal about the z-axis must change the angle ϕ by the same finite amount and leave θ and χ unchanged. Consistent orientations were obtained, and care was taken to include all the Laue spots in the orientation procedure in all crystals discussed in this work.

4.7 Analysis of the Brillouin spectrum

The Brillouin spectra were accumulated in the 1024 channels of the DAS memory. Once a desired spectrum was obtained on the CRT screen of the DAS, the channel numbers and photon counts for each peak were carefully measured using the cursor-activated readout features of the instrument.

The Brillouin spectrum can be explained using Fig. 4.5. Three (central) Rayleigh peaks (R) due to the unshifted Rayleigh and parasitic scattering were usually recorded. Associated with each Rayleigh peak, there were symmetrically upshifted and downshifted longitudinal components (L), slow transverse components (T_1) and fast transverse components (T_2). The frequency shift in channel numbers for a particular acous-

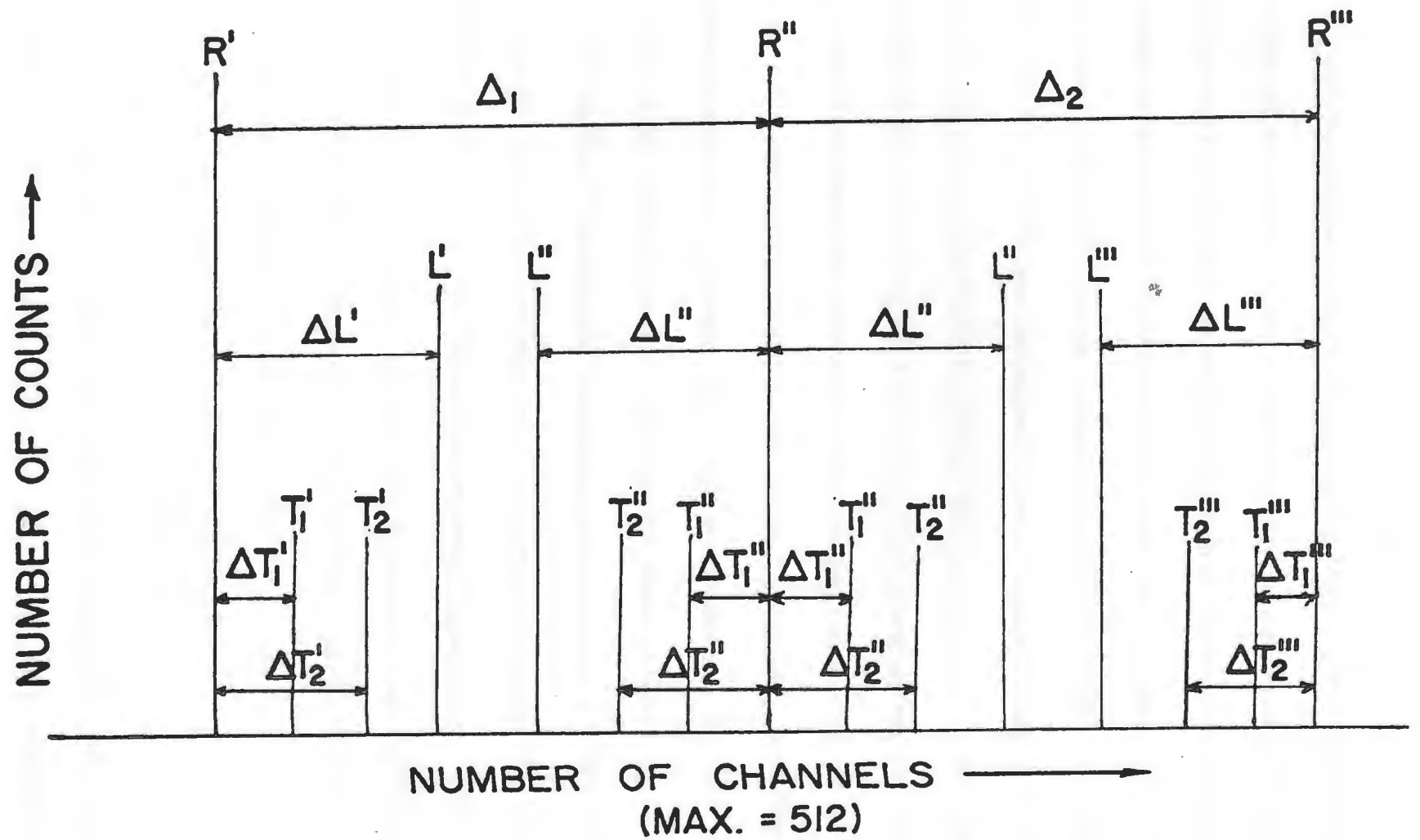


Figure 4.5: Stick-diagram of the Brillouin spectrum.

tic mode was obtained by the difference between the channel number corresponding to the acoustic mode and the channel number corresponding to the Rayleigh peak from which this acoustic mode was frequency shifted. The average frequency shifts in channel numbers for all three acoustic modes were then calculated. Since the distance between two Rayleigh peaks was defined as the *SFR* of the Fabry-Perot interferometer, the average *SFR* was determined in terms of channel numbers. The *SFR* in GHz units was calculated both by mechanically measuring the spacing between the plates (to within 0.01 mm) and by recording the Brillouin spectra of a quartz sample whose transverse and longitudinal shifts are already known to be 15.15 GHz and 23.88 GHz, respectively. From this information the conversion factor between the channel numbers and frequency units in GHz was determined. This factor was used to convert the average shifts of the three acoustic modes to GHz units.

For extremely weak signals, the segmented ramp feature of the DAS was used. A segment was set up extending from the Rayleigh to a longitudinal component. The Fabry-Perot spent more time in this segmented region to record features such as extremely weak transverse components and it was noted that significant changes in the positions of these components could occur. The nonsegmented (actual) shift was therefore calculated by the following relation:

$$\Delta T^* = \Delta T \frac{\Delta L^*}{\Delta L}$$

where the asteriks refer to the segmented shifts. Various *SFRs* were used in these experiments to avoid overlap of different spectral features and to correctly assign the

frequency shifts to the respective Rayleigh lines. Typically the frequency shift measurements are considered to be accurate to within 1 channel. This generally corresponds to about 0.5 % to 1.0 % for longitudinal and transverse components, respectively.

4.8 Determination of the elastic constants

The elastic constants were calculated using a computerized least squares-fit iteration procedure [32] [34]. Trial values of the three elastic constants were assumed. For each crystal orientation specified by the Euler angles, the λ_{ij} s were calculated from Eq. 3.10 and Eq. 3.11. and the λ matrix was subsequently diagonalized. The diagonal elements gave three eigenvalues for ω in Eq. 3.9. The acoustic velocities corresponding to each crystal orientation were then obtained by

$$V_{\mu} = \frac{\omega_{\mu}(\mathbf{q})}{q} \quad (4.9)$$

where q is the magnitude of \mathbf{q} . The frequency shifts due to the propagation of the acoustic waves were then determined from Eq. 3.21. These calculated frequency shifts were labeled as $\nu_k^{calc}(C_{ij})$, where k refers to a particular orientation. The differences between the calculated frequency shifts and the observed frequency shifts were then minimized by a least squares-fit procedure based on Newton's method [107]. The actual term which was minimized with respect to the variation in elastic constants was χ^2 defined by

$$\chi^2(C_{ij}) = \frac{1}{N-3} \sum_{k=1}^N \left(\frac{\nu_k^{calc}(C_{ij}) - \nu_k^{obs}}{\sigma_k} \right)^2 \quad (4.10)$$

where N is the total number of measured transverse and longitudinal frequency shifts at a particular temperature, $N - 3$ is the number of degrees of freedom, and σ_k is a weighting factor and is the standard deviation of the k th frequency shift measurement. This (σ_k) was varied from 0.01 GHz to 0.09 GHz in the present work. The quoted "relative" errors are based on the criterion that when $\chi^2 = 1$, σ_k would be equal to one standard deviation. The best-fit elastic constants were those values for which χ^2 was minimum.

4.9 Application of magnetic field

A magnetic field was applied to crystals of γ - O_2 near the triple point and the phase transition temperature to study the effect of external magnetic field on the spectrum, and hence the possible magnetic coupling to acoustic phonons in γ - O_2 as explained in Section 2.3.

The electromagnet used in this experiment was an A-2 electromagnet (Quantum Electronics Corporation) which provided a uniform magnetic field of up to 0.45 T between tapered pole faces of 1 inch diameter. Each pole piece was held in place by two clamp screws. The gap between the pole pieces could be varied from 0 to 4 inches. The pole pieces were placed in various configurations around the tail section of the cryostat (inside which the sample cell was situated). The electromagnet consisted of 4500 turns of heavy copper wire wound directly on a core and protected by an aluminum cover. A regulated power supply provided a current of 50 mA to 1.8 A at 60 V DC through the wires to create the required magnetic fields. The maximum

Chapter 5

Experimental results

5.1 Results for α -carbon monoxide

5.1.1 The Brillouin spectrum of α -CO

CO gas of 99% purity (Matheson Gas Products) was used to grow and cool single crystals of β -CO as explained in Section 4.4. Single crystals of α -CO were grown by cooling single crystals of β -CO to 62.0 K, and by subsequent slow cooling through the phase transition to 60.9 K. The β phase underwent dramatic changes just before the phase transition. Tiny spaces appeared and the crystal lost its transparency. After several hours, an interface appeared that visually separated the two phases which were transparent by this time. Since x-ray diffraction photographs indicated traces of the parent β phase left in the daughter α phase, the crystal was cooled by another 0.1-0.3 K to complete the phase transition. This was confirmed by taking Laue photographs which showed no further trace of the parent phase in the daughter phase. Three single crystals of about 8 mm in length were finally grown in this way. Laue x-ray diffraction photographs were taken to ensure that α -CO crystals were

single and to determine their orientations as discussed in Section 3.5.

Three Rayleigh peaks (R) were recorded for each spectrum. These were the most intense features. There were two longitudinal components (L), an upshifted and a downshifted, situated symmetrically about the central Rayleigh peak. The transverse component (T_2) was almost always present but the other transverse component (T_1) was observed for only two orientations of one of the crystals. Although an input power of 20 mW was used, these transverse modes were very weak in intensity and 10-12 hours were required in order to collect one spectrum. Generally the longitudinal component was 1000 times weaker than the Rayleigh peak and about 20 times stronger than the strongest transverse component. The *SFR* in this experiment was 11.19 GHz. All widths for all spectra described in this work were instrumental i.e. as given by the Finesse.

Brillouin spectra were recorded for 18 orientations of three single crystals of α -CO close to the α - β phase transition temperature and the measured frequency shifts are shown in Table 5.1

5.1.2 Elastic constants of α -CO

Values of the density and refractive index were necessary in order to determine the elastic constants. The value for the density of CO at 60.9 K was obtained from the temperature dependence of the molar volume measurements and was $\rho(60.9K) = 0.965 \text{ g/cm}^3$ with about 1% uncertainty [55] [108]. There is no measurement of the refractive index of solid CO in the literature. The values for density and refractive

Table 5.1: Brillouin scattering data for single crystals of α -CO at 60.9 K.

Crystal	Euler Angles in degrees			Observed frequency shifts in GHz			Calculated best-fit frequency shifts in GHz		
	θ	ϕ	χ	L	T_2	T_1	L	T_2	T_1
1	116.1	105.1	49.4	5.99	5.995	3.660	2.805
	116.3	114.9	49.4	6.08	2.58	6.092	3.657	2.592
	117.0	125.0	49.9	6.13	2.49	6.139	3.658	2.477
	116.7	135.2	49.9	6.15	2.59	6.126	3.661	2.504
	116.5	142.7	50.0	6.10	2.70	6.085	3.661	2.602
	116.2	152.6	50.4	6.11	6.006	3.647	2.800
2	63.9	296.2	53.6	6.20	6.167	3.518	2.607
	63.9	306.2	52.6	6.08	6.185	3.546	2.524
	62.0	317.5	52.5	6.25	2.72	6.133	3.592	2.587
	61.8	328.5	52.0	6.01	2.85	6.026	3.640	2.765
	62.4	342.2	50.5	5.98	3.02	5.880	3.658	3.041
	63.6	351.3	52.1	5.79	5.831	3.621	3.176
3	54.9	267.2	96.3	6.24	3.44	2.73	6.231	3.285	2.756
	54.9	277.2	96.3	6.19	2.58	6.254	3.208	2.794
	54.9	287.2	96.3	6.16	2.55	6.264	3.265	2.705
	54.6	294.9	97.9	6.10	2.57	6.244	3.376	2.612
	53.3	306.0	99.9	6.15	2.55	6.179	3.520	2.574
	53.4	317.5	98.3	6.21	3.61	2.64	6.089	3.555	2.737

index of β -CO [32] [33] were used along with the Lorentz-Lorenz relation to obtain $n(60.9K) = 1.27$ with about 2% uncertainty.

The procedure as outlined in Section 4.8 was used to calculate the adiabatic elastic constants. The best-fit values for α -CO at 60.9 K are (in units of kbar):

$C_{11} = 24.06 \pm 0.54$ $C_{12} = 14.40 \pm 0.45$ $C_{44} = 10.62 \pm 0.36$. The bulk modulus is given by $B_s = (C_{11} + 2C_{12})/3$ and is 20.9 in the same units.

The above quoted errors were determined by the quality of the fit (here $\sigma_k = 0.09$ GHz) and are good as far as relative values are concerned. In addition, there is a possible systematic error of the order of up to 3% due to uncertainties in the values of index of refraction, density, and scattering angle.

5.1.3 α - β phase transition in CO

The mechanism of the α - β phase transition and correlation between the orientations of these two phases has been previously performed in this laboratory and reported for three different single crystals of CO [32]. By determining the orientation of each crystal relative to the laboratory frame of reference, it was possible to correlate the two orientations. The correlation involves noting the correspondence between the hcp basal planes and the particular plane to which it transformed in the cubic phase. Using the rotation matrix R defined in Section 3.4 (with the Euler angles of the hcp phase), the c-axis for each of the three β -CO single crystals was transformed to the lab frame of reference. Then an application of the inverse rotation matrix with the Euler angles of the fcc phase results in the new components of the (old hcp) c-axis in

the fcc structure. The following notations were adopted

- () for a lattice plane
- { } for a family of planes
- [] for the direction of a lattice point
- < > for a family of directions

crystal I

Fig. 5.1 shows the Laue diffraction pattern for the transmission x-rays for β -CO at 0° orientation of the cell. For the β phase, the orientation (i.e. the crystals body axis with respect to the lab frame of reference) at 0° rotation of the cell was determined to be: $(\theta, \phi, \chi)_\beta = (74.6, 171.3, 46.3)$. These Euler angles were consistent with orientations obtained at 10° and 350° rotation of the cell. Fig. 5.2 shows the Laue diffraction pattern for the transmission x-rays for α -CO at 0° rotation of the cell.

For the α phase, the orientation (i.e. the crystals body axis with respect to the lab frame of reference) at 0° rotation of the cell was determined to be: $(\theta, \phi, \chi)_\alpha = (116.7, 135.2, 49.9)$. These Euler angles were also consistent with orientations obtained at 10° and 350° rotation of the cell. the c-axis was calculated to have changed to the $[0.81 \ -0.06 \ 0.60]$ direction in the fcc structure. This is very close (within 8°) to the $[101]$ direction and means that the basal planes of the hcp phase transformed close to $\{110\}$ planes of the fcc phase.

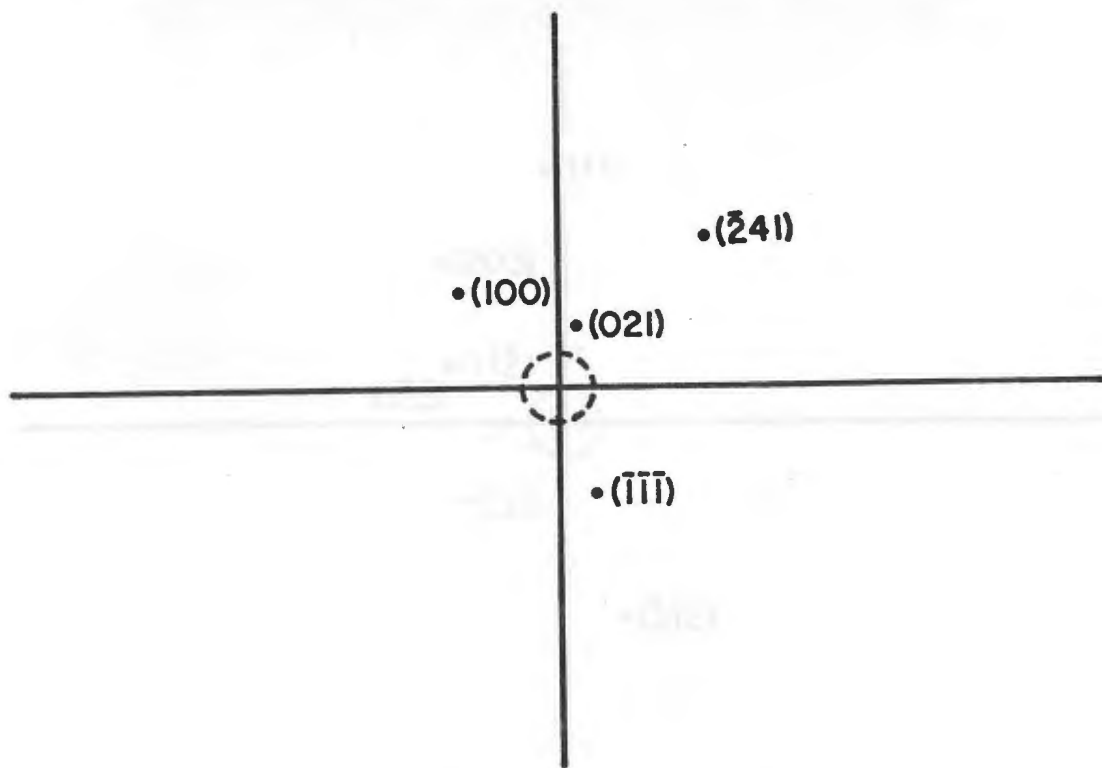
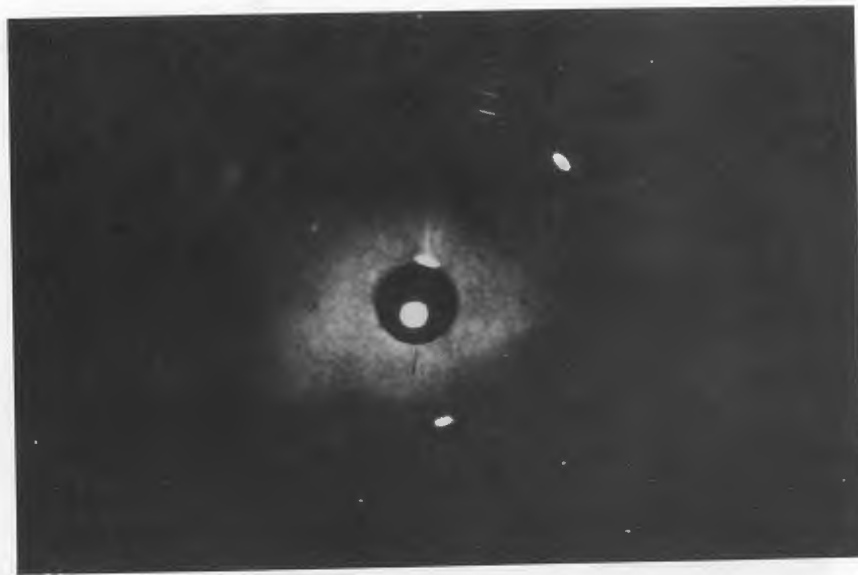


Figure 5.1: Laue diffraction pattern of the β phase of crystal I.

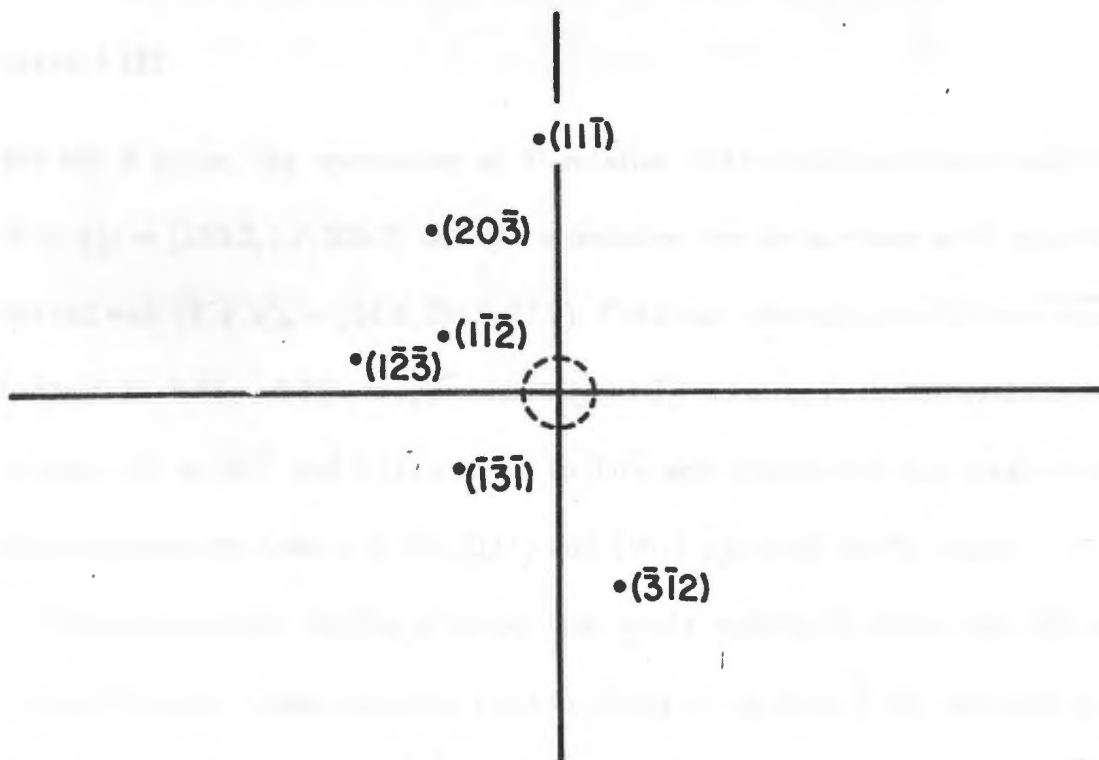


Figure 5.2: Laue diffraction pattern of the α phase of crystal I.

crystal II

For the β phase, the orientation at 0° rotation of the cell was determined to be: $(\theta, \phi, \chi)_\beta = (82.1, 198.2, 247.6)$. These values were again consistent with orientations obtained at 10° and 350° rotation of the cell.

The orientation for the α phase at 0° rotation of the cell was determined to be: $(\theta, \phi, \chi)_\alpha = (61.8, 328.5, 52.0)$. Using the appropriate transformations, the c-axis was calculated to have changed to the $[0.54 \quad -0.30 \quad -0.75]$ direction in the fcc structure which is at 20° to $[10\bar{1}]$ and 15° to $[1\bar{1}\bar{1}]$. This implies that the basal planes of the hcp transform close to the $\{110\}$ and $\{111\}$ planes of the fcc phase.

crystal III

For the β phase, the orientation at 0° rotation of the cell was determined to be: $(\theta, \phi, \chi)_\beta = (153.2, 1.7, 305.2)$ and the orientation for the α phase at 0° rotation of the cell was: $(\theta, \phi, \chi)_\alpha = (54.6, 294.9, 97.9)$. The c-axis was calculated to have changed to the $[0.34 \quad 0.37 \quad -0.86]$ (or approximately $[11\bar{3}]$) direction in the fcc structure. This is about 30° to $[01\bar{1}]$ and $[11\bar{1}]$ and 25° to $[00\bar{1}]$ and implies that the basal planes of the hcp transform close to $\{110\}$, $\{111\}$ and $\{001\}$ planes of the fcc phase.

From the present results, although not nearly exactly, it seems that the basal planes of the hcp phase transform close to planes of the form $\{110\}$, although planes of the form $\{111\}$ also appear to be a possibility for the α - β phase transition in *CO*.

5.2 Results for γ -oxygen

5.2.1 The Brillouin spectrum of γ - O_2

Oxygen gas of 99.99% purity (Matheson Gas Products) was used to grow four large single crystals of γ - O_2 in a manner explained in Section 4.4. X-ray Laue diffraction photographs were taken to ensure that they are single and of good quality (strain-free) and to determine their orientations. The x-ray diffraction patterns of γ - O_2 usually included 5-9 Laue spots. These crystals were cooled to the desired temperatures as explained in Section 4.4.

A typical Brillouin spectrum of γ - O_2 is shown in Fig. 5.3. The *SFR* for this experiment was 7.19 GHz. An hour was sufficient to collect the spectrum at 10 mW input power. One set of longitudinal components (L), an upshifted and a downshifted, and one set of transverse (doublet) components (either T_1 or T_2) were recorded. A second transverse component was never observed for any of the orientations studied in the temperature range of 54.0-44.0 K in the Brillouin spectrum of γ - O_2 , even when the segmented ramp feature of the DAS was used to increase the accumulation time between the Rayleigh and longitudinal components by a factor of 70. The Brillouin shifts for different orientations were very similar at the triple point, and maximum variations of only 1% and 2% were observed for the longitudinal and the transverse shifts, respectively [65]. These variations were comparable to the error in the measurements. Near the phase transition temperature (44.0 K), however, the maximum variations increased to 3% and 20%, respectively.

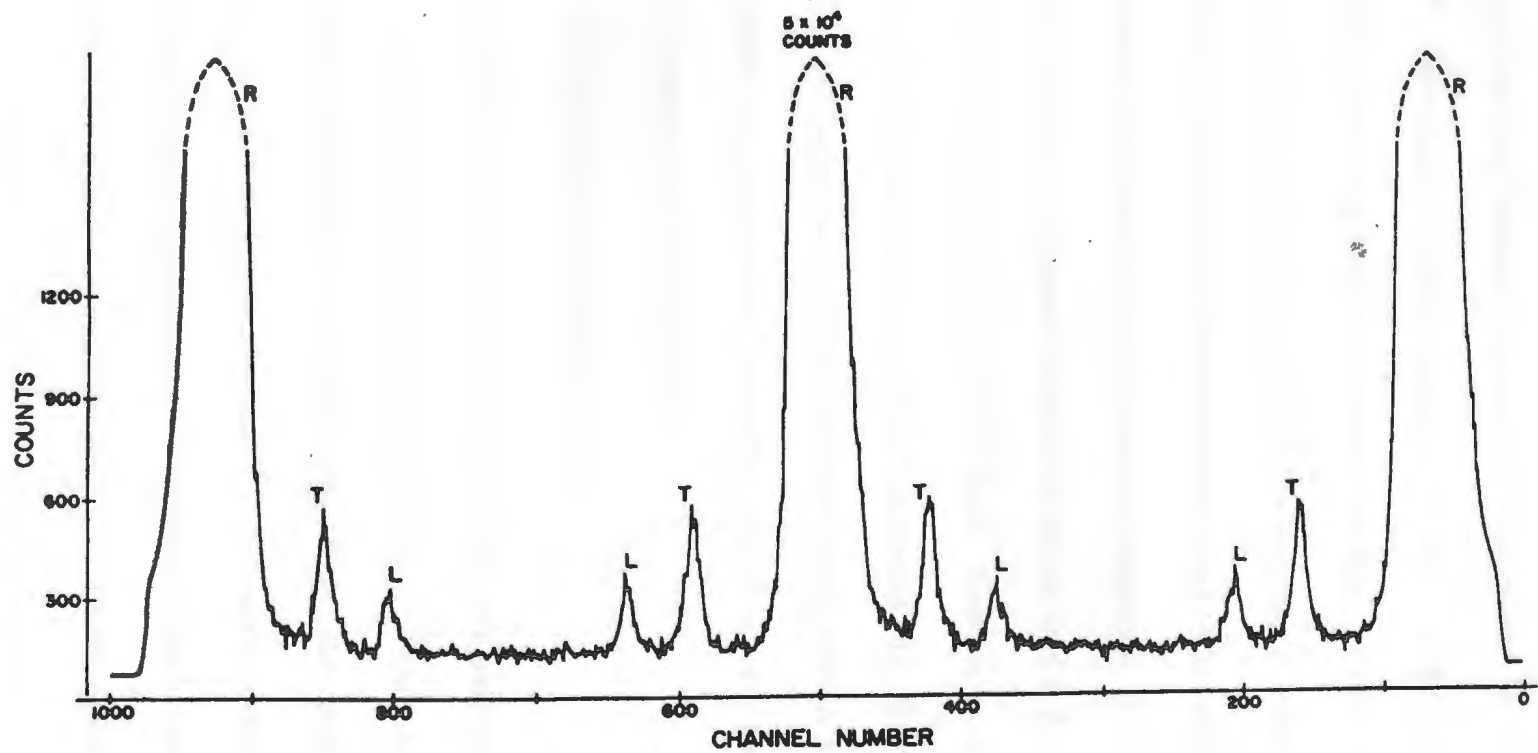


Figure 5.3: The Brillouin spectrum of γ -O₂ at 44.0 K.

The intensity of the transverse component in $\gamma\text{-O}_2$ behaves very unusually in that I_T/I_L can vary between 0.4 and 2.0 for different orientations near the triple point [65]. This range of ratios changes to 0.5-2.9 near the phase transition. In one of the crystals for which Brillouin spectra were systematically recorded for different temperatures between 54.0 K and 44.0 K, it was directly noted that the intensity of the transverse components increased with decreasing temperature. A peculiar feature of the Brillouin spectrum of $\gamma\text{-O}_2$ is its strong background. A 5145 Å filter was placed in front of the pinhole A3 to see whether this background is due to Raman scattering and if the second transverse was hidden there. However no second transverse was observed with the filter in place and the background still persisted.

In total 14 spectra were recorded for two of the crystals at 49.0 K (Table 5.2), 46.5 K (Table 5.3), and 45.6 K (Table 5.4) and 21 spectra were recorded for three different crystals at 44.0 K (Table 5.5).

5.2.2 Elastic constants of $\gamma\text{-O}_2$

The densities for solid $\gamma\text{-O}_2$ for the temperatures studied were obtained from the molar volume measurements as a function of temperature [109] and are shown in Table 5.6. The corresponding values for the refractive indices (also shown in Table 5.6) were obtained by using the triple point values for the density and refractive index of the solid, and the Lorentz-Lorenz relation. The adiabatic elastic constants were calculated as a function of temperature using the method outlined in Section 5.1. Since it was

Table 5.2: Brillouin scattering data for single crystals of γ -O₂ at 49.0 K.

Crystal	Euler angles in degrees			Observed frequency shifts in GHz			Calculated best-fit frequency shift in GHz			Observed intensity ratios		Calculated intensity ratios	
	θ	ϕ	χ	L	T ₂	T ₁	L	T ₂	T ₁	I _{T₂} /I _L	I _{T₁} /I _L	I _{T₂} /I _L	I _{T₁} /I _L
1	54.9	62.5	32.6	4.91	1.52	4.905	1.568	1.506	2.30	0.074	2.073
	54.9	72.5	32.6	4.92	1.50	4.904	1.567	1.511	2.12	0.095	2.039
	54.9	82.5	32.6	4.90	1.52	4.899	1.570	1.524	2.00	0.103	1.852
	54.9	92.5	32.6	4.91	1.55	4.892	1.576	1.541	1.44	0.094	1.551
	54.9	102.5	32.6	4.90	1.54	4.884	1.582	1.560	1.00	0.065	1.220
	54.9	112.5	32.6	4.90	1.56	4.876	1.588	1.577	0.85	0.023	0.938
	54.9	122.5	32.6	4.90	1.61	4.871	1.592	1.589	0.64	0.005	0.742
2	114.2	274.8	148.4	4.87	1.57	4.883	1.582	1.563	0.83	0.400	0.847
	114.2	284.8	148.4	4.86	1.58	4.876	1.589	1.576	0.69	0.476	0.406
	114.2	294.8	148.4	4.86	1.58	4.872	1.593	1.585	0.43	0.442	0.200
	114.2	304.8	148.4	4.86	1.60	4.871	1.592	1.590	0.45	0.533	0.031
	114.2	314.8	148.4	4.85	1.59	4.873	1.593	1.583	0.45	0.360	0.271
	114.2	324.8	148.4	4.87	1.57	4.877	1.590	1.572	0.54	0.440	0.399
	114.2	334.8	148.4	4.88	1.57	4.884	1.582	1.558	0.81	0.515	0.670

Table 5.3: Brillouin scattering data for single crystals of γ -O₂ at 46.5 K.

Crystal	Euler angles in degrees			Observed frequency shifts in GHz			Calculated best-fit frequency shift in GHz			Observed intensity ratios		Calculated intensity ratios	
	θ	ϕ	χ	L	T_2	T_1	L	T_2	T_1	I_{T_2}/I_L	I_{T_1}/I_L	I_{T_2}/I_L	I_{T_1}/I_L
1	54.9	62.5	32.6	4.96	1.45	4.962	1.564	1.441	3.12	0.087	2.439
	54.9	72.5	32.6	4.96	1.45	4.960	1.563	1.451	2.54	0.111	2.376
	54.9	82.5	32.6	4.97	1.47	4.950	1.569	1.476	2.17	0.119	2.111
	54.9	92.5	32.6	4.94	1.50	4.936	1.580	1.511	1.40	0.107	1.718
	54.9	102.5	32.6	4.94	1.55	4.920	1.593	1.549	1.22	0.074	1.309
	54.9	112.5	32.6	4.92	1.57	4.906	1.604	1.583	0.84	0.026	0.980
	54.9	122.5	32.6	4.90	1.60	4.896	1.612	1.606	0.70	0.004	0.761
2	114.2	274.8	148.4	4.90	1.56	4.919	1.593	1.555	0.83	0.424	0.907
	114.2	284.8	148.4	4.91	1.59	4.906	1.607	1.581	0.72	0.492	0.425
	114.2	294.8	148.4	4.90	1.59	4.898	1.614	1.599	0.52	0.450	0.203
	114.2	304.8	148.4	4.87	1.62	4.895	1.612	1.608	0.42	0.538	0.031
	114.2	314.8	148.4	4.90	1.60	4.899	1.614	1.595	0.54	0.366	0.276
	114.2	324.8	148.4	4.89	1.61	4.908	1.608	1.572	0.69	0.454	0.418
	114.2	334.8	148.4	4.91	1.57	4.922	1.593	1.545	0.76	0.542	0.725

Table 5.4: Brillouin scattering data for single crystals of γ -O₂ at 45.6 K.

Crystal	Euler angles in degrees			Observed frequency shifts in GHz			Calculated best-fit frequency shift in GHz			Observed* intensity ratios		Calculated intensity ratios	
	θ	ϕ	χ	L	T ₂	T ₁	L	T ₂	T ₁	I _{T₂}/I_L}	I _{T₁}/I_L}	I _{T₂}/I_L}	I _{T₁}/I_L}
	1	54.9	62.5	32.6	4.99	1.42	4.986	1.566	1.415	2.59	0.056
	54.9	72.5	32.6	4.99	1.42	4.983	1.565	1.428	2.50	0.072	2.077
	54.9	82.5	32.6	4.98	1.45	4.971	1.573	1.458	1.29	0.075	1.843
	54.9	92.5	32.6	4.97	1.49	4.955	1.586	1.501	1.80	0.064	1.514
	54.9	102.5	32.6	4.95	1.54	4.935	1.601	1.548	1.17	0.041	1.186
	54.9	112.5	32.6	4.92	1.58	4.917	1.615	1.589	0.88	0.012	0.931
	54.9	122.5	32.6	4.92	1.60	4.905	1.625	1.617	0.73	0.010	0.763
2	114.2	274.8	148.4	4.92	1.58	4.933	1.601	1.555	0.99	0.341	0.838
	114.2	284.8	148.4	4.91	1.61	4.917	1.618	1.586	0.60	0.444	0.439
	114.2	294.8	148.4	4.90	1.60	4.907	1.627	1.608	0.44	0.463	0.231
	114.2	304.8	148.4	4.91	1.59	4.904	1.625	1.620	0.42	0.606	0.024
	114.2	314.8	148.4	4.90	1.63	4.909	1.627	1.603	0.58	0.379	0.305
	114.2	324.8	148.4	4.92	1.59	4.920	1.619	1.576	0.58	0.417	0.440
	114.2	334.8	148.4	4.92	1.58	4.937	1.601	1.543	0.66	0.450	0.697

Table 5.5: Brillouin scattering data for single crystals of γ -O₂ at 44.0 K.

Crystal	Euler angles in degrees			Observed frequency shifts in GHz			Calculated best-fit frequency shift in GHz			Observed [*] intensity ratios		Calculated intensity ratios	
	θ	ϕ	χ	L	T ₂	T ₁	L	T ₂	T ₁	I _{T₂}/I_L}	I _{T₁}/I_L}	I _{T₂}/I_L}	I _{T₁}/I_L}
1	54.9	62.5	32.6	5.02	1.36	5.018	1.560	1.346	2.90	0.065	2.649
	54.9	72.5	32.6	5.02	1.36	5.014	1.559	1.365	2.58	0.082	2.545
	54.9	82.5	32.6	5.01	1.39	4.999	1.568	1.411	2.27	0.085	2.216
	54.9	92.5	32.6	4.98	1.46	4.976	1.586	1.471	1.60	0.072	1.782
	54.9	102.5	32.6	4.97	1.51	4.950	1.607	1.536	1.30	0.046	1.370
	54.9	112.5	32.6	4.95	1.56	4.925	1.626	1.592	1.00	0.013	1.064
	54.9	122.5	32.6	4.92	1.66	4.909	1.638	1.629	0.83	0.011	0.868
2	114.2	274.8	148.4	4.93	1.57	4.947	1.606	1.541	0.99	0.382	0.971
	114.2	284.8	148.4	4.93	1.60	4.925	1.629	1.585	0.65	0.497	0.510
	114.2	294.8	148.4	4.91	1.63	4.911	1.641	1.615	0.63	0.526	0.267
	114.2	304.8	148.4	4.91	1.62	4.907	1.638	1.631	0.49	0.694	0.026
	114.2	314.8	148.4	4.91	1.62	4.914	1.641	1.608	0.65	0.430	0.352
	114.2	324.8	148.4	4.92	1.61	4.930	1.630	1.570	0.65	0.468	0.514
	114.2	334.8	148.4	4.93	1.56	4.952	1.605	1.525	1.05	0.503	0.819

Table 5.5 (Conti.)

3	49.7	55.1	203.6	5.00	1.41	5.015	1.517	1.402	2.39	0.156	2.224
	49.7	65.1	203.6	5.02	1.39	5.027	1.492	1.387	2.72	0.130	2.593
	49.7	75.1	203.6	5.02	1.38	5.029	1.486	1.387	2.35	0.153	2.645
	49.7	85.1	203.6	5.01	1.40	5.021	1.504	1.398	2.10	0.284	2.282
	49.7	95.1	203.6	5.00	1.40	5.003	1.537	1.424	1.59	0.341	1.786
	49.7	105.1	203.6	4.98	1.46	4.980	1.572	1.468	1.45	0.293	1.355
	49.7	115.1	203.6	4.95	1.51	4.953	1.603	1.524	1.14	0.202	1.051

not possible to decide whether the observed transverse component was T_1 or T_2 , a complete analysis for the determination of the elastic constants was performed assuming the transverse component to be T_2 , and the whole analysis was then repeated assuming it to be T_1 at all temperatures studied. The resulting elastic constants in both cases agree within the quoted relative uncertainties. The final assignment was made based on comparing the measured intensity data with those calculated from an evaluation of the Pockel's coefficients ratios.

The Pockel's coefficients were calculated using a method similar to the determination of elastic constants [65]. Initial values of P_{12}/P_{11} and P_{44}/P_{11} were assumed. These values were used to calculate the intensity ratios I_{T_1}/I_L and I_{T_2}/I_L . The initial values of the elasto-optic ratios were varied using a computerized least squares-fit procedure until reasonable agreement between the calculated and the measured intensity ratios was achieved. The correct labelling of the transverse intensity ratios resulted in a fit that best reproduced the input intensity ratios (with the least χ^2 value). By the end of this procedure, it was clear which transverse mode was T_1 and which was T_2 (or a sum of the two), as designated in Tables 5.2-5.5.

The best-fit adiabatic elastic constants for $\gamma\text{-O}_2$ as a function of temperature were then determined and are shown in Table 5.6 and in Fig. 5.4. The quoted errors were determined by the quality of the fit and the σ_k values were 0.01 GHz, 0.01 GHz, 0.01 GHz, and 0.02 GHz for 49.0 K, 46.5 K, 45.6 K, and 44.0 K, respectively. In addition to the quoted errors, there is a 1.5%-2% systematic uncertainty due to the

values of the density, refractive index and the scattering angle. It should be mentioned that Brillouin spectra near the triple point were recorded and the elastic constants were entirely consistent with those of Kieft *et al* [65].

Information on the ratios of the Pockel's coefficients was also obtained from the ratio of the intensities of the transverse to longitudinal components using the iteration method mentioned above. This fit was considered satisfactory because only ratios for peak intensities (possibly for both transverse modes together) were measured and almost all the measured intensity ratios were reproduced to within 10%. The results for the elasto-optic ratios for different temperatures are shown in Table 5.7. Estimated values of the Pockel's coefficients are also given in this Table using the following approximate expression [110]

$$P_{11} + 2P_{12} = \frac{(\epsilon - 1)(\epsilon + 2)}{\epsilon^2}$$

here $\epsilon = n^2$ where n is the refractive index.

5.2.3 Magnetic field results

To possibly explain the peculiar aspects of the γ - O_2 Brillouin spectrum, especially the single and very intense transverse components, it was decided to study the Brillouin spectra of γ - O_2 under the influence of a magnetic field, as explained in Section 2.3. An electromagnet was set up at 90° and 60° to the z-axis and a field of up to 0.45 T was established. No noticeable changes were observed in either shifts or intensities of the Brillouin spectra of this material as recorded for 2 hours for four orientations near

Table 5.6: Temperature dependent data for $\gamma\text{-O}_2$

Temperature (K)	Density (g/cm ³)	Refractive index	C_{11} (kbar)	C_{12} (kbar)	C_{44} (kbar)	A	B (kbar)
49.0	1.367	1.2732	26.47±0.04	21.47±0.05	2.83±0.02	1.13	23.14
46.5	1.376	1.2752	26.80±0.04	22.30±0.05	2.94±0.01	1.31	23.80
45.6	1.382	1.2764	26.96±0.04	22.64±0.05	2.99±0.01	1.38	24.08
44.0	1.387	1.2776	27.01±0.04	23.18±0.04	3.06±0.01	1.56	24.45

Table 5.7: Elasto-optic ratios and constants for $\gamma\text{-O}_2$

Temperature (K)	P_{12}/P_{11}	P_{44}/P_{11}	P_{11}	P_{12}	P_{44}
49.0	0.39±0.02	0.15±0.01	0.48	0.19	0.07
46.5	0.38±0.01	0.15±0.01	0.49	0.19	0.07
45.6	0.42±0.03	0.17±0.02	0.47	0.19	0.07
44.0	0.41±0.01	0.17±0.01	0.47	0.19	0.08

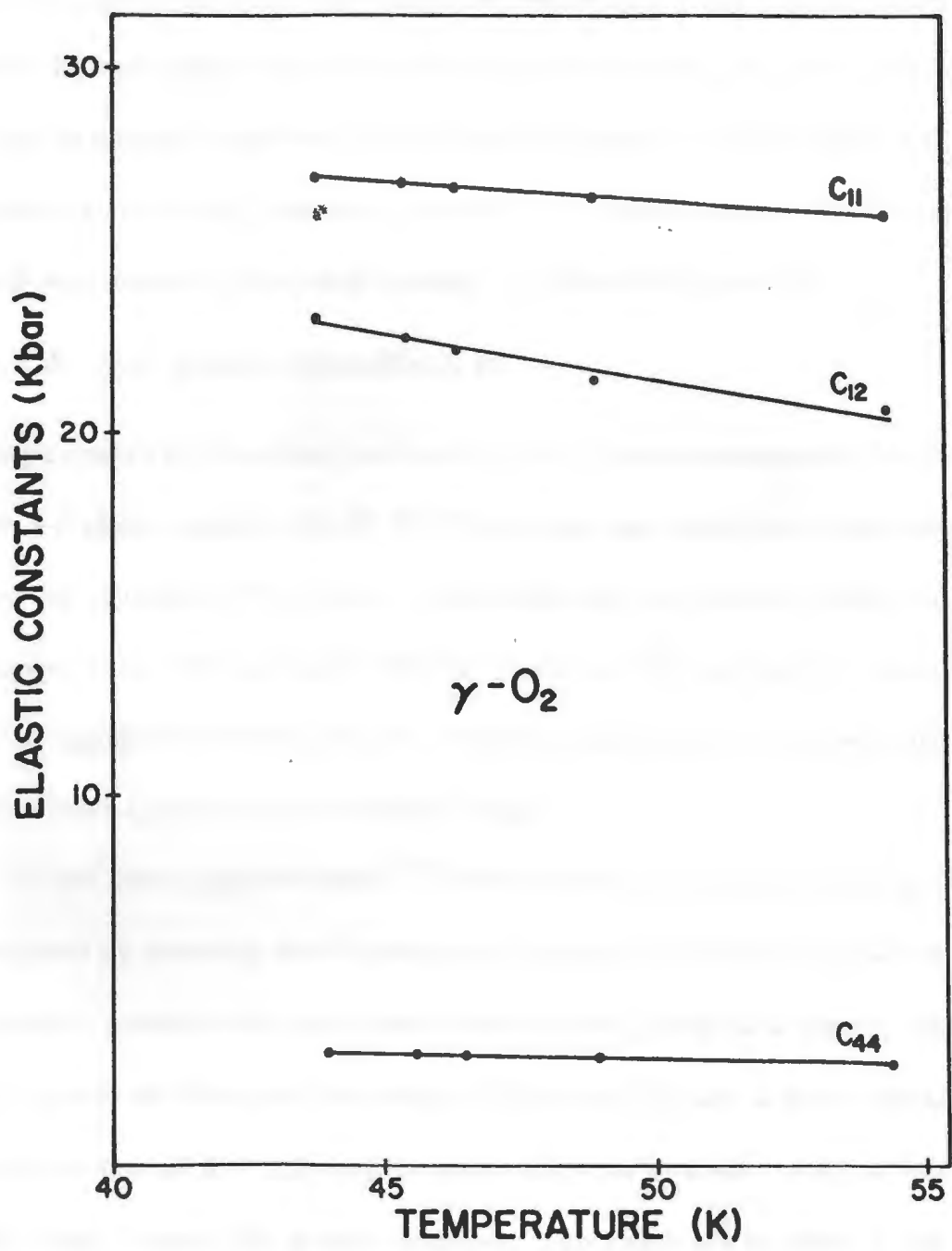


Figure 5.4: Temperature dependence of the elastic constants of γ - O_2

the triple point and the phase transition temperature. Particular emphasis was placed on orientations where the transverse component was strongest. This suggested that the unusual properties of $\gamma\text{-O}_2$ were not related to its magnetic nature. It was, therefore, at this time, decided to later study cyclooctane which has a similar structure and large degrees of rotational freedom as explained in Section 2.4.

5.2.4 $\gamma\text{-}\beta$ phase transition in O_2

Single crystals of $\gamma\text{-O}_2$ which were cooled to 44.0 K were subsequently cooled through the $\gamma\text{-}\beta$ phase transition (43.78 K). The cooling was carried out at the rate of 1 K per day to maintain the crystal in thermodynamic equilibrium. There is a volume change of about 8% associated with the transition. The resulting β crystal consisted of an aggregate of crystallites with different orientations (as observed with x-rays) and always appeared to be somewhat opaque.

It had been suggested before [111] that transparent single crystals of $\beta\text{-O}_2$ could be grown by annealing the β crystal very close to the transition temperature. The annealing process would presumably result in the growth of a larger crystallite at the expense of others until the sample is fully converted into a single crystal. It was further suggested that replacing the quartz cell walls by a softer material like Dacron film might improve the growth condition. This could not be done in the present experiment and also was probably not necessary since the crystal was released from the walls by pumping. Even when the crystal was cooled through the phase transition without the action of the pump, it contracted and stayed away from the walls of the

cell. The phase transition was carried out five times. Each time the crystal was kept near the phase transition for several weeks. The crystal became opaque during the phase transition and remained opaque afterwards (for at least 1 month).

One time, however, the resulting β phase did change into a single crystal but it still remained opaque. Fig 5.5 shows the Laue diffraction pattern for the β - O_2 single crystal and the computer fit to the position of the Laue spots. The spots were well defined; and the orientation of the rhombohedral crystal axes (of the β phase) with respect to the laboratory frame of reference defined according to Nye [95] was $(\phi, \theta, \chi) = (119.9, 1.6, 58.6)$. The other four crystals did not form a single crystal of the β phase. Even upon cooling β - O_2 crystals to temperatures around 23 K, no apparent changes were observed in the condition of the crystal. The purpose behind cooling to 23 K was to see if the α - β phase transition would have an improving effect on the transparency of the β phase.

The laser beam was passed through the β - O_2 single crystal and the resulting spectrum was observed on the DAS screen. The Rayleigh scattering intensity was extremely intense. The phase transition was probably accompanied by the development of voids or cavities inside the crystal and the boundary of these voids scattered the light so strongly that made it impossible to observe the Brillouin spectrum of β - O_2 . Almost 1 year was spent trying to grow transparent single crystals of β - O_2 .

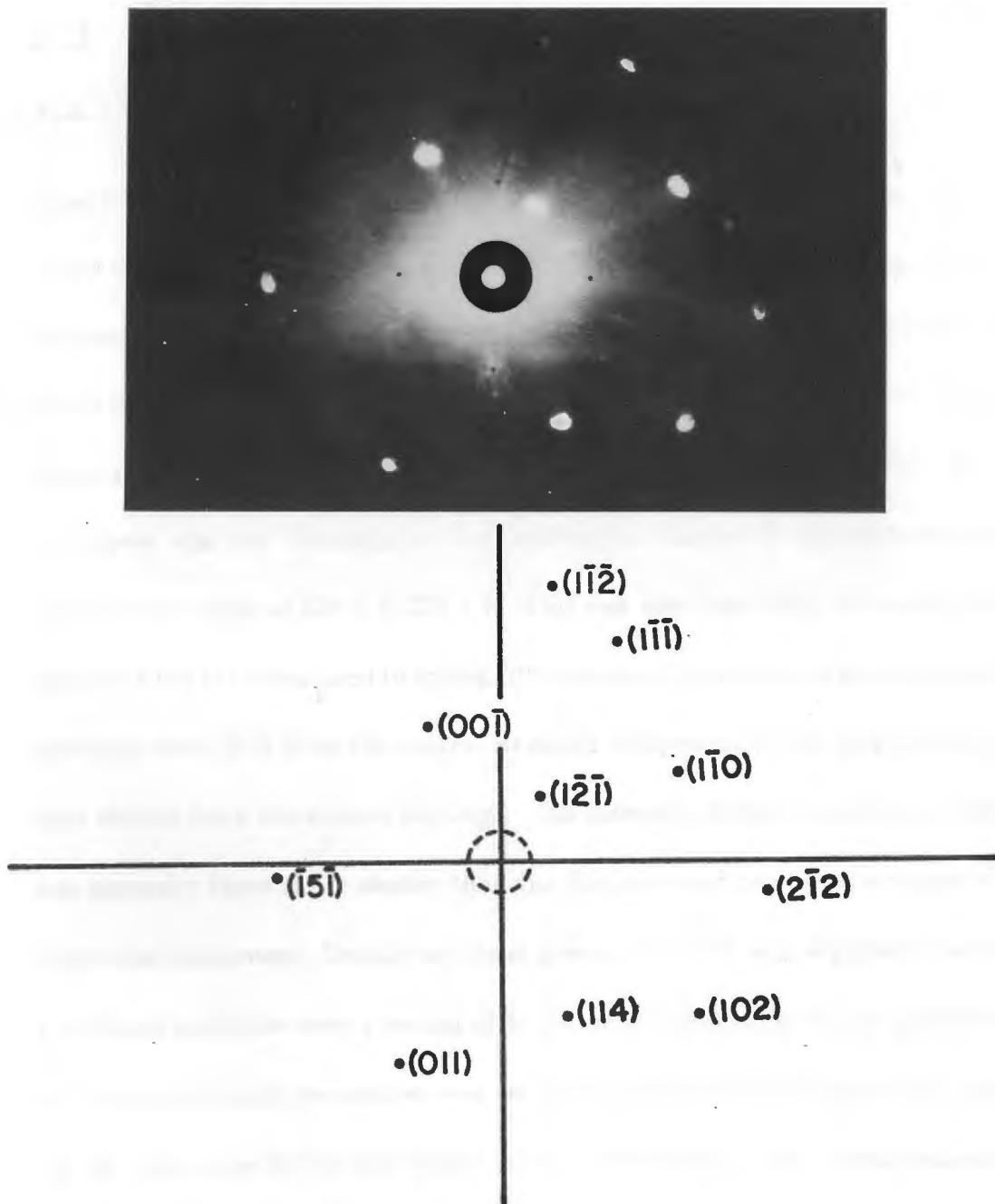


Figure 5.5: Laue diffraction photograph of the beta phase of O_2 .

5.3 Results for cyclooctane I

5.3.1 Brillouin spectrum of cyclooctane I

Liquid cyclooctane of 99+% purity (Aldrich Chem. Comp. Inc.) was used to grow single crystals of cyclooctane I as explained in Section 4.4. Brillouin spectra of three different single crystals of cyclooctane I were recorded at 284.2 K. The spectrum consisted of a strong central component due to Rayleigh scattering, a set of longitudinal components L and one set of transverse components (either T_1 or T_2). No second transverse was ever observed for the orientations studied in this experiment in the temperature range of 284.2 K-224.2 K. This was also true when the segmented ramp feature of the DAS was used to spend 70 times more time in the segmented area of the spectrum extending from the central Rayleigh component to the longitudinal component shifted from the central Rayleigh. The intensity of the longitudinal component was generally three times weaker than the Rayleigh and ten times stronger than the transverse component. Usually an input power of 20 mW was required to accumulate a Brillouin spectrum over a period of 8-10 hours. The change in the frequency shifts from one orientation to another was very small (upto 2% for longitudinal shifts and 7% for transverse shifts) and comparable to the errors in their measurements. The crystal was therefore almost isotropic with respect to the propagation of the hyper-sonic waves. The spectral free range in this experiment was 16.513 GHz. A strong background was present in the Brillouin spectrum of cyclooctane I. A 5145 Å filter was placed in front of the pinhole A3 to see whether this background is due to Raman

scattering. Filtering reduced the background significantly and the contrast ratio of the longitudinal intensity to the background was increased from 2:1 to 15:1.

Brillouin spectra were recorded for 36 orientations of three different single crystals of cyclooctane I at 284.2 K (close to the triple point of 288 K) as shown in Table 5.8. In addition, two of the crystals were cooled, one to 274.2 K (Table 5.9), 254.2 K (Table 5.10), 234.2 K (Table 5.11) with 12 recorded spectra at each temperature and the other to 224.2 K (Table 5.12) with 3 recorded spectra. It was not possible to cool these crystal any further because a large bubble developed within the crystal and the Laue x-rays indicated the development of strain in the sample manifested by less clearly defined spots in the photograph.

5.3.2 Elastic constants of cyclooctane I

The values of the density at different temperatures were calculated from the measured values of lattice constants which were 11.90 Å and 11.82 Å at 273.2 K and 209.2 K, respectively, by assuming a linear behavior of lattice constant with temperature [77]. The refractive index of the liquid cyclooctane at 293.2 K as provided by the manufacturer (Aldrich Chem. Comp. Inc.) was 1.4574. The only other known value for the refractive index of liquid cyclooctane at 293.2 K is 1.45849 [76]. The density of the liquid phase at 293.2 K was also provided and was 0.834 g/cm³ and is comparable to the only other known value at 248.7 K namely 0.8322 g/cm³ [76]. These values for the liquid density and refractive index were used along with the Lorentz-Lorenz relation to calculate the values for the refractive indices corresponding to the

Table 5.8: Brillouin scattering data for single crystals of cyclooctane I at 284.2 K.

Crystal	Euler Angles in degrees			Observed frequency shifts in GHz			Calculated best-fit frequency shifts in GHz			Observed intensity ratios		Calculated intensity ratios	
	θ	ϕ	χ	L	T_2	T_1	L	T_2	T_1	I_{T_2}/I_L	I_{T_1}/I_L	I_{T_2}/I_L	I_{T_1}/I_L
1	50.5	360.8	271.1	7.51	2.08	7.467	2.143	2.138	0.04	0.000	0.050
	50.5	340.8	271.1	7.51	2.16	7.459	2.164	2.143	0.04	0.049	0.000
	50.5	320.8	271.1	7.47	2.23	7.443	2.214	2.150	0.04	0.044	0.003
	50.5	300.8	271.1	7.39	2.19	7.430	2.241	2.168	0.02	0.035	0.013
	50.5	280.8	271.1	7.43	2.20	7.426	2.229	2.193	0.05	0.012	0.037
	50.5	260.8	271.1	7.42	2.24	7.428	2.237	2.178	0.04	0.012	0.037
	50.5	240.8	271.1	7.41	2.24	7.433	2.247	2.150	0.04	0.026	0.022
	50.5	220.8	271.1	7.39	2.24	7.444	2.220	2.139	0.04	0.036	0.012
	50.5	200.8	271.1	7.45	2.18	7.459	2.170	2.140	0.05	0.043	0.007
	50.5	180.8	271.1	7.48	2.14	7.467	2.143	2.139	0.05	0.001	0.049
	50.5	160.8	271.1	7.48	2.14	7.462	2.159	2.140	0.05	0.042	0.008
	50.5	140.8	271.1	7.44	2.15	7.448	2.209	2.139	0.04	0.037	0.011
2	35.6	243.5	113.3	7.49	2.19	7.438	2.210	2.172	0.04	0.002	0.048
	35.6	223.5	113.3	7.45	2.20	7.432	2.237	2.163	0.04	0.034	0.013
	35.6	203.5	113.3	7.43	2.20	7.433	2.246	2.152	0.03	0.044	0.002
	35.6	183.5	113.3	7.44	2.20	7.445	2.209	2.147	0.05	0.047	0.001
	35.6	163.5	113.3	7.48	2.19	7.459	2.162	2.147	0.05	0.022	0.028
	35.6	143.5	113.3	7.51	2.12	7.460	2.165	2.139	0.04	0.010	0.040
	35.6	123.5	113.3	7.45	2.17	7.447	2.194	2.157	0.06	0.037	0.011
	35.6	103.5	113.3	7.46	2.23	7.430	2.223	2.184	0.04	0.046	0.001
	35.6	83.5	113.3	7.40	2.27	7.423	2.225	2.205	0.04	0.042	0.005
	35.6	63.5	113.3	7.44	2.20	7.429	2.228	2.182	0.03	0.020	0.029
	35.6	43.5	113.3	7.42	2.15	7.443	2.214	2.150	0.03	0.023	0.026
	35.6	23.5	113.3	7.46	2.13	7.457	2.178	2.138	0.07	0.028	0.021

Table 5.8 (Conti.)

3	95.3	147.4	261.4	7.40	2.19	7.424	2.228	2.199	0.04	0.010	0.037
	95.3	167.4	261.4	7.42	2.20	7.432	2.243	2.159	0.06	0.000	0.048
	95.3	177.4	261.4	7.43	2.15	7.434	2.248	2.144	0.05	0.000	0.049
	95.3	187.4	261.4	7.42	2.13	7.435	2.251	2.138	0.04	0.002	0.048
	95.3	197.4	261.4	7.43	2.17	7.434	2.251	2.143	0.05	0.005	0.044
	95.3	207.4	261.4	7.42	2.14	7.431	2.248	2.155	0.04	0.009	0.039
	95.3	227.4	261.4	7.40	2.19	7.427	2.229	2.187	0.04	0.011	0.037
	95.3	247.4	261.4	7.41	2.20	7.431	2.232	2.173	0.06	0.000	0.048
	95.3	267.4	261.4	7.43	2.16	7.436	2.243	2.142	0.04	0.000	0.049
	95.3	287.4	261.4	7.43	2.14	7.437	2.237	2.146	0.04	0.002	0.047
	95.3	307.4	261.4	7.42	2.16	7.435	2.217	2.175	0.04	0.001	0.047
	95.3	327.4	261.4	7.43	2.18	7.435	2.230	2.161	0.04	0.006	0.042

Table 5.9: Brillouin scattering data for single crystals of cyclooctane I at 274.2 K.

Crystal	Euler Angles in degrees			Observed frequency shifts in GHz			Calculated best-fit frequency shifts in GHz			Observed intensity ratios		Calculated intensity ratios	
	θ	ϕ	χ	L	T_2	T_1	L	T_2	T_1	I_{T_2}/I_L	I_{T_1}/I_L	I_{T_2}/I_L	I_{T_1}/I_L
1	50.5	360.8	271.1	7.60	2.12	7.592	2.144	2.141	0.05	0.000	0.042
	50.5	340.8	271.1	7.62	2.21	7.586	2.163	2.144	0.03	0.045	0.000
	50.5	320.8	271.1	7.59	2.22	7.572	2.205	2.151	0.03	0.045	0.004
	50.5	300.8	271.1	7.56	2.31	7.561	2.228	2.166	0.08	0.038	0.015
	50.5	280.8	271.1	7.54	2.19	7.558	2.217	2.187	0.04	0.014	0.046
	50.5	260.8	271.1	7.57	2.20	7.559	2.224	2.174	0.05	0.016	0.043
	50.5	240.8	271.1	7.55	2.17	7.564	2.233	2.150	0.04	0.031	0.022
	50.5	220.8	271.1	7.57	2.20	7.573	2.210	2.141	0.06	0.038	0.010
	50.5	200.8	271.1	7.57	2.15	7.585	2.167	2.142	0.05	0.040	0.005
	50.5	180.8	271.1	7.57	2.12	7.592	2.144	2.141	0.05	0.001	0.042
	50.5	160.8	271.1	7.60	2.18	7.588	2.158	2.142	0.05	0.038	0.006
	50.5	140.8	271.1	7.58	2.13	7.576	2.200	2.141	0.05	0.037	0.009

Table 5.10: Brillouin scattering data for single crystals of cyclooctane I at 254.2 K.

Crystal	Euler Angles in degrees			Observed frequency shifts in GHz			Calculated best-fit frequency shifts in GHz			Observed intensity ratios*		Calculated intensity ratios	
	θ	ϕ	χ	L	T_2	T_1	L	T_2	T_1	I_{T_2}/I_L	I_{T_1}/I_L	I_{T_2}/I_L	I_{T_1}/I_L
1	50.5	360.8	271.1	8.11	2.13	8.086	2.162	2.161	0.07	0.061	0.000
	50.5	340.8	271.1	8.06	2.20	8.087	2.161	2.159	0.06	0.001	0.077
	50.5	320.8	271.1	8.07	2.19	8.088	2.161	2.154	0.08	0.009	0.090
	50.5	300.8	271.1	8.11	2.19	8.090	2.159	2.152	0.08	0.039	0.091
	50.5	280.8	271.1	8.05	2.13	8.090	2.156	2.153	0.05	0.120	0.042
	50.5	260.8	271.1	8.09	2.16	8.090	2.158	2.152	0.05	0.106	0.051
	50.5	240.8	271.1	8.14	2.12	8.089	2.161	2.151	0.06	0.043	0.077
	50.5	220.8	271.1	8.07	2.12	8.088	2.162	2.154	0.07	0.015	0.080
	50.5	200.8	271.1	8.10	2.17	8.087	2.162	2.159	0.10	0.007	0.071
	50.5	180.8	271.1	8.07	2.16	8.086	2.162	2.161	0.06	0.060	0.001
	50.5	160.8	271.1	8.06	2.19	8.087	2.162	2.160	0.07	0.008	0.064
	50.5	140.8	271.1	8.12	2.15	8.088	2.162	2.155	0.09	0.014	0.075

Table 5.11: Brillouin scattering data for single crystals of cyclooctane I at 234.2 K.

Crystal	Euler Angles in degrees			Observed frequency shifts in GHz			Calculated best-fit frequency shifts in GHz			Observed intensity ratios ^{ap}		Calculated intensity ratios	
	θ	ϕ	χ	L	T_2	T_1	L	T_2	T_1	I_{T_2}/I_L	I_{T_1}/I_L	I_{T_2}/I_L	I_{T_1}/I_L
1	50.5	360.8	271.1	8.26	8.333	2.118	2.117	0.099	0.000
	50.5	340.8	271.1	8.26	2.16	8.333	2.117	2.116	0.11	0.000	0.102
	50.5	320.8	271.1	8.26	2.14	8.334	2.117	2.114	0.08	0.008	0.102
	50.5	300.8	271.1	8.26	2.09	8.334	2.116	2.113	0.07	0.031	0.087
	50.5	280.8	271.1	8.38	2.15	8.335	2.115	2.113	0.08	0.095	0.030
	50.5	260.8	271.1	8.39	2.07	8.335	2.116	2.113	0.09	0.091	0.033
	50.5	240.8	271.1	8.41	2.16	8.334	2.117	2.112	0.21	0.048	0.068
	50.5	220.8	271.1	8.37	2.16	8.334	2.118	2.114	0.23	0.023	0.085
	50.5	200.8	271.1	8.42	2.12	8.333	2.118	2.116	0.21	0.013	0.089
	50.5	180.8	271.1	8.37	2.12	8.333	2.118	2.117	0.07	0.097	0.002
	50.5	160.8	271.1	8.38	2.08	8.333	2.117	2.117	0.13	0.015	0.086
	50.5	140.8	271.1	8.26	2.02	8.334	2.118	2.114	0.11	0.022	0.084

Table 5.12: Brillouin scattering data for single crystals of cyclooctane I at 224.2 K.

Crystal	Euler Angles in degrees			Observed frequency shifts in GHz			Calculated best-fit frequency shifts in GHz		
	θ	ϕ	χ	L	T_2	T_1	L	T_2	T_1
3	95.3	217.4	261.4	8.45	2.00	8.436	2.037	1.999
	95.3	207.4	261.4	8.46	1.99	8.437	2.041	1.990*
	95.3	197.4	261.4	8.417	1.98	8.438	2.043	1.983

densities in Table 5.13. The measured frequency shifts were then analyzed by using the Brillouin equation and the eigenvalue equations for the acoustic wave dynamical matrix with the computerized iterative least-squares fit procedure explained in Section 4.8. Since it was not possible to decide whether the observed transverse was T_1 or T_2 , the procedure outlined in Section 5.2 for this identification (based on intensities) was adopted. Labelling all the transverse modes as either T_1 or T_2 , however, resulted in elastic constants that agreed with one another within the quoted relative uncertainties. The best-fit adiabatic elastic constants for cyclooctane I are given in Table 5.13 and in Fig. 5.6 for different temperatures along with the anisotropy factor A and the adiabatic bulk modulus B . The values of σ_k associated with each fit are 0.02 GHz, 0.03 GHz, 0.03 GHz, 0.06 GHz, and 0.02 GHz for 284.2 K, 274.2 K, 254.2 K, 234.2 K and 224.4 K respectively. In addition to the quoted uncertainties, there is possible systematic error of 1.5%-2% due to uncertainties in the values of index of refraction, density and scattering angle.

Information on the ratios of the Pockel's coefficients was also obtained from the ratio of the intensities of the transverse to longitudinal components using the iteration method mentioned in Section 5.2. This fit was again considered satisfactory because almost all the measured intensity ratios were reproduced to within 10%. The ratios of the Pockel's coefficients and their estimated absolute values as a function of temperature are given in Table 5.14.

Table 5.13: Temperature dependent data for cyclooctane I single crystals

Temperature (K)	Density (g/cm ³)	Refractive index	C_{11} (kbar)	C_{12} (kbar)	C_{44} (kbar)	A	B (kbar)
284.2	0.8805	1.4873	29.39±0.04	24.03±0.04	2.41±0.02	0.90	25.82
274.2	0.8844	1.4898	30.41±0.10	25.12±0.10	2.42±0.03	0.92	26.88
254.2	0.8888	1.4927	34.53±0.09	29.64±0.09	2.47±0.03	1.01	31.27
234.2	0.8944	1.4963	36.72±0.18	32.00±0.18	2.37±0.06	1.00	33.57
224.2	0.8970	1.4980	37.82±0.36	33.39±0.18	2.08±0.07	0.94	34.87

Table 5.14: Temperature dependent data for Pockel's ratios and coefficients for cyclooctane I single crystals

Temperature (K)	P_{12}/P_{11}	P_{44}/P_{11}	P_{11}	P_{12}	P_{44}
284.2	0.84±0.01	0.07±0.01	0.39	0.33	0.03
274.2	0.83±0.01	0.07±0.01	0.39	0.32	0.03
254.2	0.76±0.01	0.07±0.01	0.41	0.32	0.03
234.2	0.79±0.02	0.09±0.01	0.46	0.37	0.03

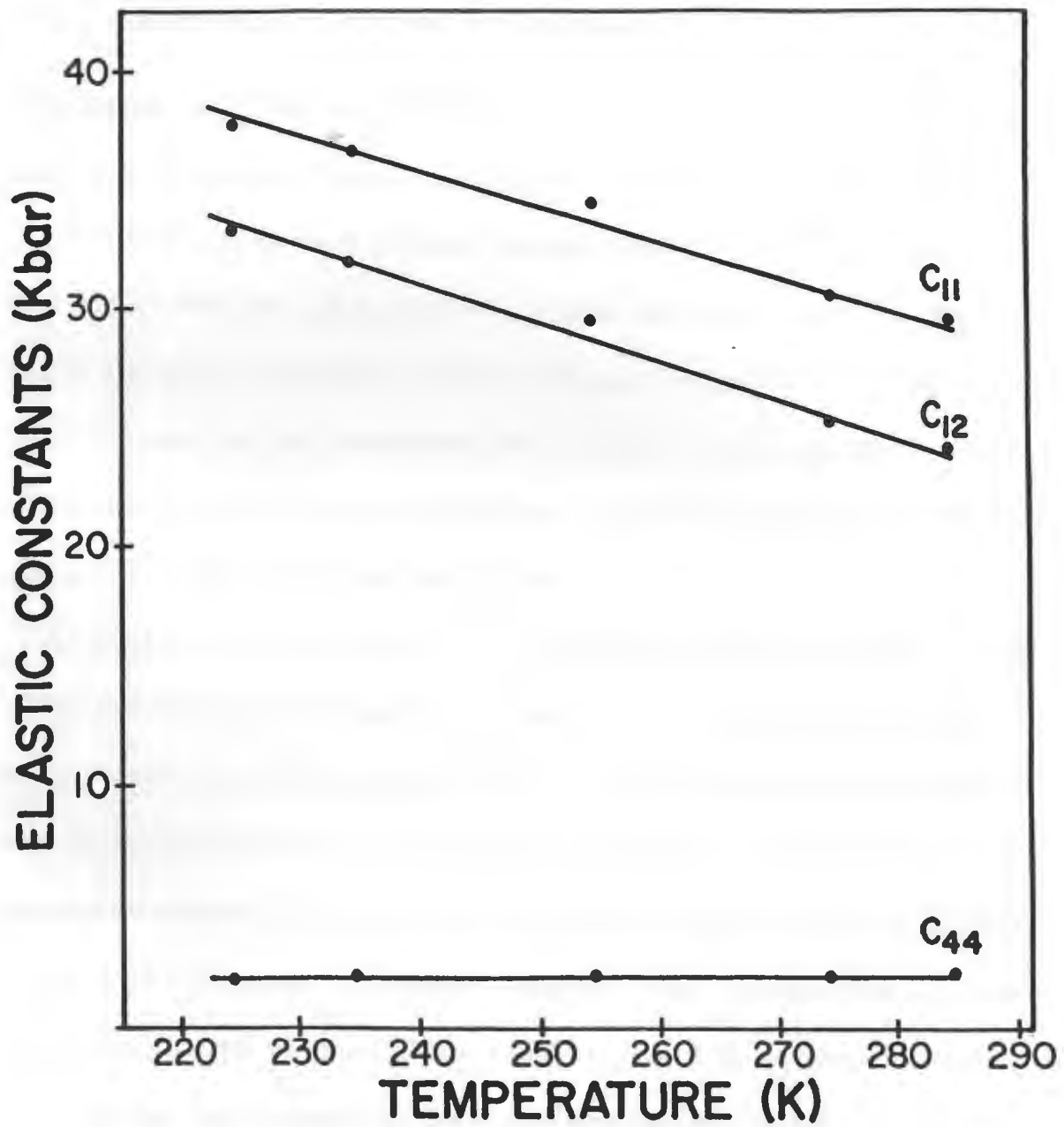


Figure 5.6: Temperature dependence of elastic constants of cyclooctane I

5.4 Results for methane I

5.4.1 Brillouin spectrum of methane I

Methane gas of 99.99% purity (Matheson Gas Products) was used to grow single crystals of methane as explained in Section 4.4. Brillouin spectra were recorded for 21 orientations of three different single crystals of methane I at 72.8 K (Table 5.15) and 50.9 K (Table 5.16). In addition, one of the crystals was cooled to 38.5 K (Table 5.17) and 25.0 K (Table 5.18) with 7 recorded spectra per temperature. Attempts were made to further cool the crystals and look for possible visual signs due to critical effects associated with the second order phase transition in methane at 20.6 K. No indication of critical phenomena was observed.

A typical spectrum is shown in Fig. 5.7. The Brillouin spectra consisted of a strong central component due to Rayleigh scattering, a set of longitudinal components L and one set of transverse components (either T_1 or T_2). Both transverse components were never observed together for any orientation studied in this experiment in the temperature range of 72.8 K and 25.0 K. This was also true when the segmented ramp feature of the DAS was used to spend 70 times more time in the segmented area than any where else in the spectrum. Usually input powers of 20 mW were required to accumulate the Brillouin spectrum over a 2-3 hour period. The spectral free range used in this experiment was 16.43 GHz. A 5145 Å filter was placed in front of the aperture A3 to block the strong background due to Raman scattering.

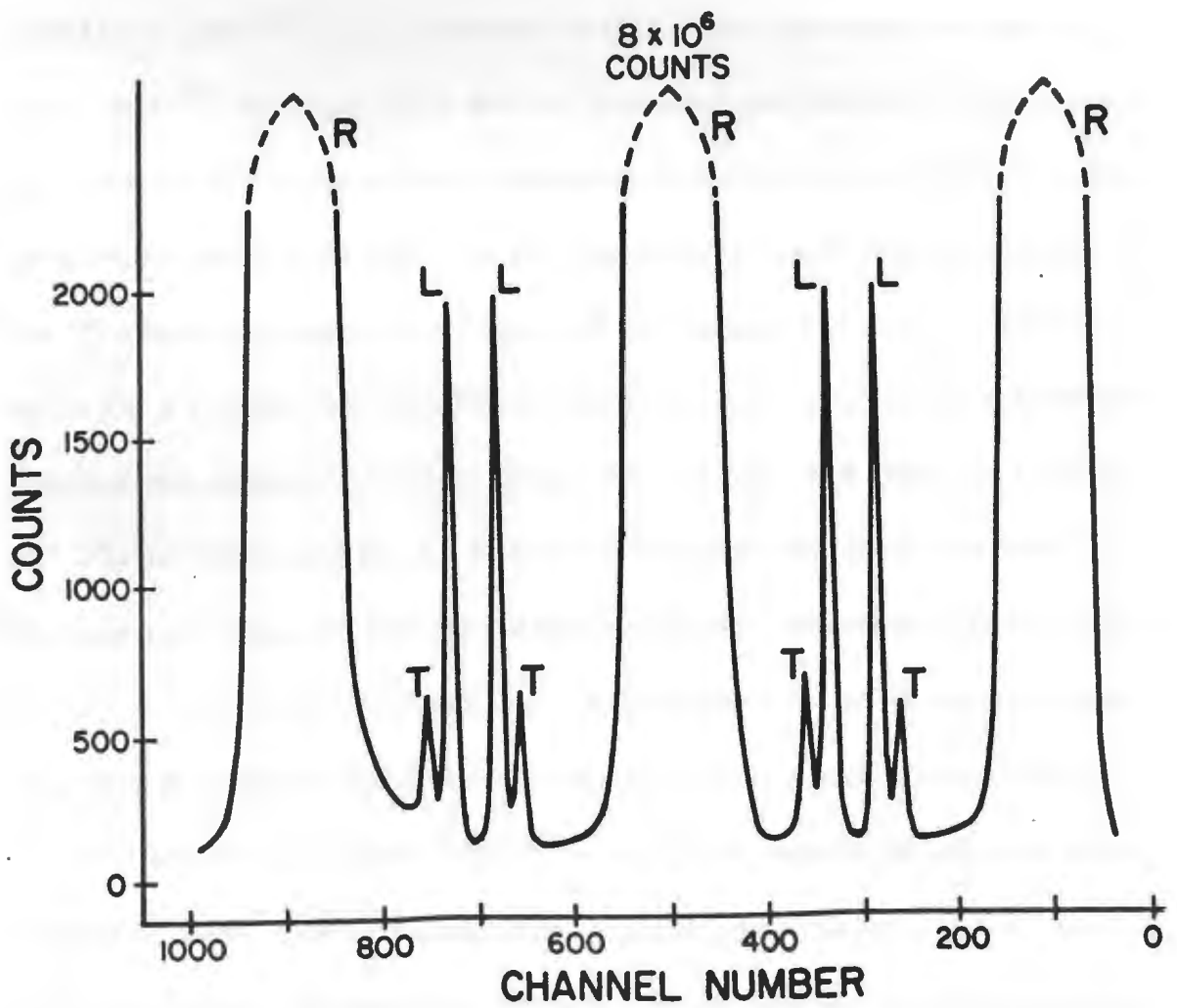


Figure 5.7: The Brillouin spectrum of methane I at 25.0 K.

5.4.2 Elastic constants of methane I

Assuming a linear behaviour of density with temperature ^[112], the values of the density at different temperatures were calculated from the following known values of the densities of solid methane I:

$\rho(77.4\text{ K}) = 0.494\text{ g/cm}^3$, $\rho(20.4\text{ K}) = 0.522\text{ g/cm}^3$, $\rho(90.4\text{ K}) = 0.4874\text{ g/cm}^3$. The value for the refractive index of solid methane at the triple point is known to be $n(90.4\text{ K}) = 1.323$ ^[90]. These values for the solid density and refractive index at the triple point ^[90] were used along with the Lorentz-Lorenz relation to calculate the values for the refractive indices corresponding to the densities in Table 5.19. The measured frequency shifts were then analyzed using the method outlined in Section 4.8. The best-fit adiabatic elastic constants for methane I is shown in Table 5.19 and in Fig. 5.8 for different temperatures along with the anisotropy factor A and the adiabatic bulk modulus B . The σ_k values were 0.05 GHz, 0.09 GHz, 0.05 GHz and 0.07 GHz for 72.8 K, 50.9 K, 38.5 K, and 25.0 K respectively. It must be noted that the triple point values (90.4 K) for the elastic constants obtained in this experiment were $C_{11} = 19.37$, $C_{12} = 14.12$ and $C_{44} = 9.04$ in kbar units which were consistent with those measured by Rand *et al.* In addition to the quoted errors, there is an additional systematic error of 1.5%-2% due to uncertainties in the values of index of refraction, density and scattering angle. Information on the ratios of the Pockel's coefficients was also obtained from the ratio of the intensities of the transverse to longitudinal components using the iteration method mentioned in Section 4.8. This

Table 5.15: Brillouin scattering data for single crystals of methane I at 72.8 K.

Crystal	Euler Angles in degrees			Observed frequency shifts in GHz			Calculated best-fit frequency shifts in GHz			Observed intensity ratios		Calculated intensity ratios	
	θ	ϕ	χ	L	T_2	T_1	L	T_2	T_1	I_{T_2}/I_L	I_{T_1}/I_L	I_{T_2}/I_L	I_{T_1}/I_L
	1	98.0	227.6	269.1	9.51	3.88	9.529	4.276	3.840	0.11	0.015
	98.0	237.6	269.1	9.47	4.45	9.510	4.397	3.750	0.04	0.044	0.032
	98.0	247.6	269.1	9.44	4.83	9.431	4.766	3.490	0.11	0.068	0.010
	98.0	257.6	269.1	9.31	5.21	9.320	5.128	3.267	0.07	0.053	0.003
	98.0	267.6	269.1	9.20	9.221	5.393	3.119	0.022	0.001
	98.0	277.6	269.1	9.19	9.177	5.495	3.069	0.007	0.002
	98.0	287.6	269.1	9.22	5.46	9.203	5.415	3.135	0.04	0.020	0.014
2	39.8	352.6	39.0	8.04	5.36	8.088	5.494	5.315	0.05	0.003	0.051
	39.8	2.6	39.0	8.02	5.37	8.038	5.482	5.400	0.06	0.006	0.035
	39.8	12.6	39.0	8.22	5.14	8.184	5.487	5.173	0.06	0.002	0.093
	40.3	22.9	38.4	8.41	4.73	8.456	5.389	4.826	0.17	0.005	0.162
	40.3	32.9	38.4	8.80	4.36	8.760	5.224	4.450	0.21	0.007	0.206
	40.8	42.7	38.2	9.03	4.04	9.034	5.033	4.110	0.22	0.004	0.208
	40.8	51.8	38.9	9.24	3.86	9.230	4.895	3.830	0.13	0.000	0.170

Table 5.15 (Conti.)

3	117.5	333.6	61.2	8.46	4.78	8.489	5.357	4.803	0.17	0.006	0.169
	117.5	323.6	61.2	8.22	5.11	8.222	5.473	5.126	0.05	0.003	0.098
	117.1	313.4	61.1	8.22	5.34	8.072	5.487	5.345	0.05	0.006	0.048
	116.4	304.3	61.5	8.22	5.35	8.105	5.485	5.298	0.05	0.006	0.060
	117.6	294.6	61.9	8.21	5.04	8.292	5.468	5.018	0.06	0.003	0.121
	116.3	285.5	61.9	8.49	4.68	8.517	5.380	4.728	0.17	0.007	0.166
	116.3	275.5	61.9	8.78	4.40	8.802	5.200	4.395	0.19	0.009	0.207

Table 5.16: Brillouin scattering data for single crystals of methane I at 50.9 K.

Crystal	Euler Angles in degrees			Observed frequency shifts in GHz			Calculated best-fit frequency shifts in GHz			Observed intensity ratios		Calculated intensity ratios	
	θ	ϕ	χ	L	T_2	T_1	L	T_2	T_1	I_{T_2}/I_L	I_{T_1}/I_L	I_{T_2}/I_L	I_{T_1}/I_L
1	98.0	227.6	269.1	10.03	4.62	10.111	4.663	4.237	0.05	0.071	0.064
	98.0	237.6	269.1	10.00	4.72	10.092	4.782	4.150	0.06	0.101	0.045
	98.0	247.6	269.1	9.90	5.18	10.012	5.147	3.900	0.11	0.120	0.018
	98.0	257.6	269.1	9.80	5.49	9.900	5.507	3.688	0.11	0.094	0.006
	98.0	267.6	269.1	9.67	5.65	9.800	5.770	3.548	0.07	0.056	0.001
	98.0	277.6	269.1	9.64	9.756	5.872	3.501	0.039	0.001
	98.0	287.6	269.1	9.76	5.85	9.782	5.792	3.564	0.09	0.058	0.015
2	39.8	352.6	39.0	8.58	5.94	8.661	5.871	5.696	0.05	0.019	0.059
	39.8	2.6	39.0	8.66	5.77	8.613	5.859	5.780	0.07	0.031	0.038
	39.8	12.6	39.0	8.86	5.52	8.756	5.864	5.557	0.14	0.012	0.105
	40.3	22.9	38.4	9.17	5.12	9.026	5.766	5.216	0.23	0.009	0.170
	40.3	32.9	38.4	9.51	4.74	9.331	5.601	4.846	0.25	0.010	0.205
	40.8	42.7	38.2	9.74	4.45	9.608	5.411	4.510	0.24	0.007	0.200
	40.8	51.8	38.9	9.97	4.22	9.807	5.274	4.234	0.20	0.003	0.159

Table 5.16 (Conti.)

3	117.5	333.6	61.2	9.08	5.29	9.059	5.734	5.194	0.18	0.012	0.173
	117.5	323.6	61.2	8.79	5.66	8.794	5.851	5.511	0.13	0.015	0.106
	117.1	313.4	61.1	8.54	5.87	8.646	5.864	5.726	0.09	0.030	0.051
	116.4	304.3	61.5	8.67	5.78	8.678	5.862	5.680	0.07	0.030	0.064
	117.6	294.6	61.9	8.87	5.48	8.863	5.846	5.404	0.14	0.014	0.129
	116.3	285.5	61.9	9.15	5.15	9.087	5.757	5.120	0.17	0.016	0.168
	116.3	275.5	61.9	9.46	4.80	9.373	5.578	4.791	0.24	0.016	0.202

Table 5.17: Brillouin scattering data for single crystals of methane I at 38.5 K.

Crystal	Euler Angles in degrees			Observed frequency shifts in GHz			Calculated best-fit frequency shifts in GHz			Observed intensity ratios		Calculated intensity ratios	
	θ	ϕ	χ	L	T_2	T_1	L	T_2	T_1	I_{T_2}/I_L	I_{T_1}/I_L	I_{T_2}/I_L	I_{T_1}/I_L
3	117.5	333.6	61.2	9.37	5.58	9.440	6.234	5.499	0.20	0.007	0.226
	117.5	323.6	61.2	9.06	5.92	9.088	6.377	5.912	0.15	0.006	0.139
	117.1	313.4	61.1	8.95	6.24	8.883	6.393	6.200	0.17	0.011	0.069
	116.4	304.3	61.5	8.97	6.17	8.928	6.391	6.137	0.15	0.011	0.086
	117.6	294.6	61.9	9.16	5.72	9.181	6.371	5.774	0.15	0.006	0.167
	116.3	285.5	61.9	9.51	5.37	9.474	6.262	5.408	0.22	0.009	0.223
	116.3	275.5	61.9	9.81	4.95	9.836	6.043	4.995	0.20	0.009	0.263

Table 5.18: Brillouin scattering data for single crystals of methane I at 25.0 K.

Crystal	Euler Angles in degrees			Observed frequency shifts in GHz			Calculated best-fit frequency shifts in GHz			Observed intensity ratios		Calculated intensity ratios	
	θ	ϕ	χ	L	T_2	T_1	L	T_2	T_1	I_{T_2}/I_L	I_{T_1}/I_L	I_{T_2}/I_L	I_{T_1}/I_L
3	117.5	333.6	61.2	9.57	5.81	9.622	6.415	5.732	0.31	0.033	0.303
	117.5	323.6	61.2	9.23	6.17	9.287	6.550	6.118	0.044	0.203
	117.1	313.4	61.1	9.12	6.23	9.093	6.566	6.387	0.12	0.099	0.099
	116.4	304.3	61.5	9.13	6.40	9.136	6.564	6.328	0.11	0.098	0.124
	117.6	294.6	61.9	9.37	6.03	9.375	6.545	5.989	0.26	0.041	0.243
	116.3	285.5	61.9	9.69	5.53	9.656	6.441	5.646	0.32	0.042	0.290
	116.3	275.5	61.9	10.07	5.29	10.004	6.233	5.260	0.27	0.049	0.334

fit was considered satisfactory because almost all the measured intensity ratios were reproduced to within 10%. The ratios of the Pockel's coefficients and their estimated absolute values as a function of temperature are given in Table 5.20.

*
Table 5.20. Temperature dependence of the ratios of the Pockel's coefficients and their estimated absolute values.

Temperature (°C)	r_{11}/r_{33}	r_{22}/r_{33}	r_{42}/r_{33}	r_{51}/r_{33}	r_{61}/r_{33}	r_{11} (esu)	r_{22} (esu)	r_{42} (esu)	r_{51} (esu)	r_{61} (esu)
25	1.00	0.98	0.95	0.92	0.90	1.00	0.98	0.95	0.92	0.90
50	1.00	0.98	0.95	0.92	0.90	1.00	0.98	0.95	0.92	0.90
75	1.00	0.98	0.95	0.92	0.90	1.00	0.98	0.95	0.92	0.90
100	1.00	0.98	0.95	0.92	0.90	1.00	0.98	0.95	0.92	0.90

Table 5.19: Temperature dependent data for methane I single crystals

Temperature (K)	Density (g/cm ³)	Refractive index	C_{11} (kbar)	C_{12} (kbar)	C_{44} (kbar)	A	B (kbar)
72.8	0.4960	1.329	23.58±0.11	16.60±0.16	11.23±0.05	3.21	18.93
50.9	0.5027	1.334	27.28±0.18	18.14±0.27	12.90±0.09	2.84	21.16
38.5	0.5134	1.342	28.75±0.20	20.15±0.40	15.48±0.15	3.60	23.02
25.0	0.5202	1.347	30.40±0.31	19.57±0.61	16.41±0.23	3.03	23.18

Table 5.20: Temperature dependent data for Pockel's ratios and coefficients for methane I single crystals

Temperature (K)	P_{12}/P_{11}	P_{44}/P_{11}	P_{11}	P_{12}	P_{44}
72.8	1.09±0.19	0.08±0.05	0.29	0.32	0.02
50.9	0.95±0.12	0.16±0.01	0.32	0.30	0.05
38.5	0.94±0.69	0.31±0.11	0.33	0.31	0.10
25.0	0.94±0.65	0.30±0.11	0.33	0.31	0.09

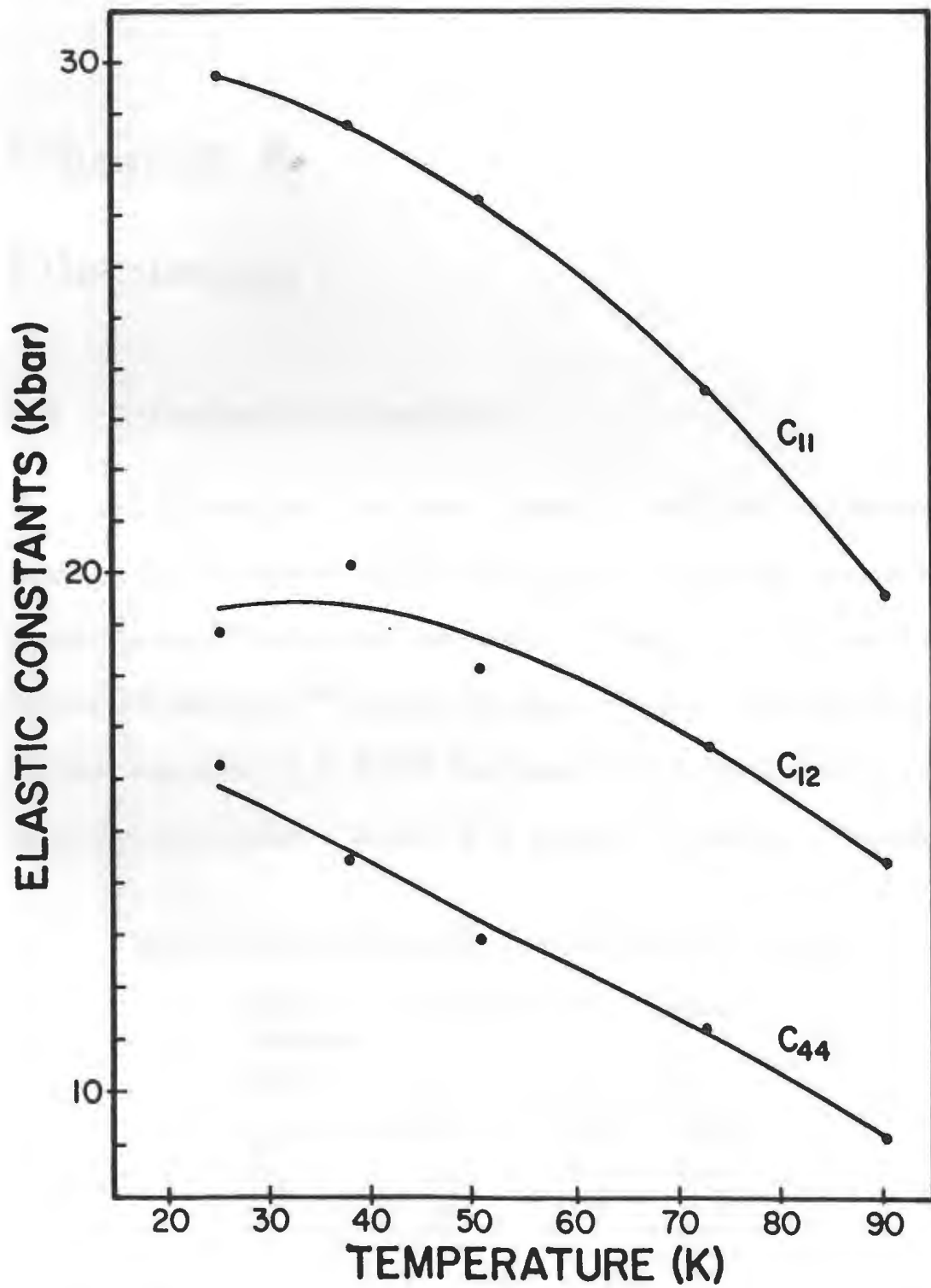


Figure 5.8: Temperature dependence of the elastic constants of methane I

Chapter 6

Discussion

6.1 α -carbon monoxide

The role of RT coupling in the lattice dynamics of α -CO can be understood by comparing the α -CO elastic constants with those of α -N₂ and the rare gas solids, particularly argon. By using the theoretically calculated elastic constants of argon between 15 K and 60 K [113], the elastic constants of α -N₂ as determined by neutron scattering experiments at 15 K [114] were scaled to 60 K. The approximate scaled values of elastic constants of α -N₂ at 60 K are shown in Table 6.1. The similarity

Table 6.1: Elastic constants of fcc phases of CO, N₂ and argon

Elastic Constants (kbar)	α -CO	α -N ₂	Argon
	60.9 K	60 K	82.3 K
C_{11}	24.1	22.0	23.8
C_{12}	14.4	16.0	15.6
C_{44}	10.6	10.0	11.2

with the elastic constants of α -CO is apparent. The elastic constants of argon at the

triple point of 82.3 K are also shown in Table 6.1 and are very close to those of α -CO. The similarity is also evident when comparing the ratios of acoustic velocities in high symmetry directions of α -CO, SF_6 [48], rare gas solids [35] and CH_4 [90] as shown in Table 6.2.

Table 6.2: Ratios of acoustic velocities in the high symmetry directions of SF_6 , CH_4 , and rare gas solids near their triple points as compared to those of α -CO

	$\langle 100 \rangle$ $V_L/V_{T_2}(=V_L/V_{T_1})$	$\langle 111 \rangle$ $V_L/V_{T_2}(=V_L/V_{T_1})$	$\langle 110 \rangle$ V_L/V_{T_2}	$\langle 110 \rangle$ V_L/V_{T_1}
Rare gas solids				
Ne, Ar, Kr, Xe [35]	1.44	2.24	1.65	2.71
SF_6 [48]	1.60	2.29	1.76	2.64
CH_4 [90]	1.47	2.46	1.70	3.23
α -CO	1.51	2.17	1.68	2.48

The ratios of acoustic velocities for different high symmetry directions were calculated from the following relations:

$$\text{in the } \langle 100 \rangle \text{ direction, } V_L/V_{T_2} = V_L/V_{T_1} = [C_{11}/C_{44}]^{1/2},$$

$$\text{in the } \langle 111 \rangle \text{ direction, } V_L/V_{T_2} = V_L/V_{T_1}$$

$$= [(C_{11} + 2C_{12} + 4C_{44})/(C_{11} - C_{12} + C_{44})]^{1/2},$$

$$\text{in the } \langle 110 \rangle \text{ direction, } V_L/V_{T_2} = [(C_{11} + C_{12} + 2C_{44})/2C_{44}]^{1/2},$$

$$\text{and } V_L/V_{T_1} = [(C_{11} + C_{12} + 2C_{44})/(C_{11} - C_{12})]^{1/2}.$$

As pointed out in the Chapter 2, the anomalously high value (3.23) of V_L/V_{T_1} in the $\langle 110 \rangle$ direction for methane is due to a slow or softened transverse T_1 mode

propagating in the $\langle 110 \rangle$ direction and can be interpreted as indicative of RT coupling^[90]. This was consistent with theoretical calculations of the elastic constants of methane which include RT coupling terms in the molecular potential^[91]. There is no significant anomaly* in the ratios of acoustic velocities of α -CO in the high symmetry directions as compared to rare gas solids (or α -N₂). This is somewhat surprising in view of the theoretical predictions concerning the role of RT coupling in α -CO as explained in Chapter 2. The results of the present experiment indicate that the coupling to the acoustic modes is negligible as far as the $q = 0$ wavevector regime is concerned and α -CO appears to behave much like a rare gas solid. The anomalies observed in the ratios of acoustic velocities V_L/V_T in the hexagonal phase of solid N₂ and CO as noted in Chapter 2 are not observed in α -CO. It should, of course, be remembered that strong coupling was predicted at intermediate wavevectors of the acoustic branch in α -CO^[6] and the small wavevector regime may therefore not be affected very much by this coupling. The other factor that should be considered is that α -CO is an ordered system and RT coupling may not necessarily be strong for the CO molecules which are librating around the diagonals of the cubic unit cell and do not possess the same degree of rotational freedom as in plastic crystals.

The mechanism of the α - β phase transition in CO has been discussed elsewhere^[32] in detail and a comprehensive comparison with the hcp-fcc phase transition in other molecular crystals and metals has been presented. The earlier results on three other single crystals of α -CO performed in this laboratory indicated that the phase tran-

sition was martensitic and the basal planes of the hcp phase seem to transform to planes of the form $\{110\}$ of the fcc phase. In one case specifically, the hcp planes transformed exactly to fcc planes of the form $\{111\}$ but then spontaneously (overnight) moved away from it and reoriented to become the $\{110\}$ planes. This is not inconsistent with the simulation studies of the β phase of nitrogen by Powell *et al.* [115] in that they did not seem to indicate a transformation of the c-axis to the cubic $[111]$ direction. It appeared that there is some kind of competition in transforming to either of the $\{111\}$ and $\{110\}$ planes. Present x-ray results are consistent with the previously published results that the hexagonal basal planes prefer to transform to planes of the form $\{110\}$ of the cubic structure although the cubic $\{111\}$ planes are also a possibility.

There were competing factors that contributed to the lack of a more well defined correlation between the parent hcp and daughter fcc phase. in the above x-ray results. In addition to the orientation of the parent crystal at the top from which the daughter phase is born, the walls of the cell are boundary conditions imposing constraints on the transition. The possible presence of a tiny particle or sharp edges at the bottom of the cell could influence the growth of the daughter phase.

6.2 Comparison of γ -oxygen and cyclooctane I

As pointed out in Chapter 2, the unusual features in the Brillouin spectrum of γ - O_2 could be either related to a magnetic coupling to the acoustic phonons or to the role of RT coupling in the peculiar structure of this cubic phase. It was expected that

the magnetic fields of up to 0.45 T would be sufficient to alter the possible magnetic coupling and produce some noticeable changes in the Brillouin spectrum of γ - O_2 . This assumption was further supported by the theoretical predictions of the effect of the magnetic fields (5-30 T) on lowering libron frequencies of β - O_2 [72]. The magnetic susceptibility of γ - O_2 is higher than that of β - O_2 by a factor of 3 [73] and hence a field of 0.45 T was deemed adequate to measurably influence possible magnetic coupling effects. The results of the magnetic studies of the Brillouin spectrum of γ - O_2 near the triple point and the phase transition temperature failed to result in any measurable changes. The possibility of higher magnetic fields effecting the nature of phonon excitations is worth investigating. It is, therefore, of value to compare γ -oxygen and cyclooctane I as noted in Section 2.3.

The Brillouin spectra of γ -oxygen and cyclooctane I single crystals have several similar features that are quite different from the spectra of other cubic crystals. These features include:

i) Both of these crystals are quite isotropic with respect to the propagation of hyper-sonic waves. The anisotropy factor A is 1.00 for γ -oxygen [65] and 0.90 for cyclooctane I at their respective triple points. The isotropy is quite clear from the observed frequency shifts near the triple point of these crystals. The variations in the frequency shifts with orientation were 1% and 2% for the longitudinal and transverse shifts in γ -oxygen, and 2% and 8% in cyclooctane I. The variation increases to 3% and 20% for γ - O_2 near the phase transition. Cyclooctane I, however, showed an almost constant

A value down to 224.2 K. The rotor-nonrotor phase transition occurs 50 K lower than this temperature and was not studied due to the development of a bubble-like space inside the crystal as explained in Section 5.3.2.

ii) Only one transverse acoustic mode was observed in the Brillouin spectra of both γ -oxygen and cyclooctane I for all the orientations and temperatures studied in the present experiments. This is a direct result of the acoustic isotropy. That the transverse acoustic modes are basically degenerate is clear from the elastic constants measurements (and calculated transverse frequency shifts in all the appropriate Tables). The elastic constants obtained by assuming all transverse shifts to be T_1 or T_2 agree within the quoted relative uncertainties.

iii) The transverse components are quite slow (soft) in both cases i.e. $V_T/V_L \sim 0.25 - 0.30$.

iv) The elastic constants C_{11} and C_{12} increase with the decrease in temperature whereas C_{44} remains almost constant as seen in Fig. 5.4 and Fig. 5.6. The rates of change of elastic constants with respect to temperature for C_{11} are -0.10 kbar/K and -0.14 kbar/K and for C_{12} are -0.25 kbar/K and -0.15 kbar/K for γ -oxygen and cyclooctane I, respectively.

v) The ratios of acoustic velocities for γ -oxygen and cyclooctane I are much higher than the ratios for rare gas solids, with those of cyclooctane I being the largest and are shown in Table 6.3. The acoustic velocity ratios in the $\langle 110 \rangle$ and $\langle 111 \rangle$ directions of γ - O_2 single crystals at 44.0 K are 14% and 10% higher than their triple

point values, respectively, and indicates a further decrease or softening in the slow

Table 6.3: Ratios of acoustic velocities in the high symmetry directions of several molecular crystals

	$\langle 100 \rangle$ $V_L/V_{T_2}(=V_L/V_{T_1})$	$\langle 111 \rangle$ $V_L/V_{T_2}(=V_L/V_{T_1})$	$\langle 110 \rangle$ V_L/V_{T_2}	$\langle 110 \rangle$ V_L/V_{T_1}
Rare gas solids				
<i>Ne, Ar, Kr, Xe</i> ^[35]	1.44	2.24	1.65	2.71
<i>SF₆</i> ^[48]	1.60	2.29	1.76	2.64
<i>CH₄</i> ^[90]	1.47	2.46	1.70	3.23
γ - <i>O₂</i> (54.4 K) ^[65]	3.07	3.09	3.07	3.10
γ - <i>O₂</i> (49.0 K)	3.06	3.21	3.08	3.27
γ - <i>O₂</i> (46.5 K)	3.02	3.28	3.06	3.11
γ - <i>O₂</i> (45.6 K)	3.00	3.39	3.05	3.59
γ - <i>O₂</i> (44.0 K)	2.97	3.52	3.03	3.83
cyclooctane I (284.2 K)	3.49	3.35	3.48	3.29
cyclooctane I (274.2 K)	3.54	3.42	3.53	3.38
cyclooctane I (254.2 K)	3.74	3.75	3.46	3.76
cyclooctane I (234.2 K)	3.94	3.94	3.94	3.95
cyclooctane I (224.2 K)	4.26	4.16	4.26	4.12

transverse velocity V_{T_1} as the phase transition is approached. This point is even clearer when the acoustic velocity V_{T_1} is calculated for the $\langle 111 \rangle$ and $\langle 110 \rangle$ directions as a function of temperature as shown in Table 6.4. The decrease in acoustic velocity on approaching the phase transition, particularly in the $\langle 110 \rangle$ direction, is noted. A similar trend is also noted for cyclooctane I (whereas normally an increase in velocity with crystal hardening on cooling is expected). The increasing role of RT coupling on approaching the phase transition can, therefore, be inferred from these data. In addition, from Fig. 5.4, it is clear that $C_{11} - C_{12}$ decreases as γ -*O₂*

Table 6.4: Acoustic transverse velocity of slow T_1 mode as a function of temperature between the triple point and the γ - β phase transition in O_2

Temperature (K)	$\langle 111 \rangle$ m/sec	$\langle 110 \rangle$ m/sec
54.4	448	447
49.0	436	427
46.5	424	404
45.6	419	395
44.0	406	371

single crystals are cooled to the phase transition temperature. Such a trend is consistent with Eq. (3.43) for $C_{11} - C_{12}$ as the RT coupling effect increases. Without detailed and exhaustive theoretical calculations, it is not possible to comment more quantitatively on the magnitude of RT coupling effects.

As explained in Section 2.3, RT coupling effects are expected to be strong in the cyclooctane I rotor phase because the molecular reorientation frequency of 10^{-9} s (as determined by NMR studies [74] [75]) is of the order of the frequency of the transverse acoustic mode in plastic crystals. The similarity between the Brillouin spectra of γ -oxygen and cyclooctane I therefore implies that RT coupling effects are also strong in oxygen. This is perhaps also suggested by noting that the frequency of molecular vibrational relaxation (probably via environmental fluctuation i.e. rotational coupling) in γ - O_2 estimated from the Raman linewidths [69] are about 3 GHz and 5 GHz for the disc-like and spherically rotating molecules, respectively, and are of the order of the frequency shifts due to the acoustic waves. The results of Michel support the above observation with regard to the role of symmetry in RT coupling. Oxygen is

centrosymmetric and of low symmetry ($l = 2$) hence coupling between the rotational variables and the acoustic modes near the $q = 0$ wavevector regime is favoured. This coupling manifests itself in the form of soft acoustic phonons T_1 .

In γ -oxygen and cyclooctane I, the elastic isotropy can perhaps be explained by noting that the rotation of the disc-like molecules on the faces of the unit cell occur in three mutually perpendicular directions and will somehow average out spherically. In any case the isotropy would be expected to be greatest near the triple point since greater rotational freedom exists at the higher temperatures. This is indeed as observed for γ - O_2 and is therefore consistent with the proposed RT coupling effect.

The depolarized background in the Brillouin spectra of γ -oxygen persisted even after appropriate filtering and suggests a relatively broad Rayleigh wing contribution which may be caused by the rotational motion of the molecules [116] as discussed for liquids in Section 1.2. A similar background was present in the Brillouin spectra of cyclooctane I. Appropriate filtering, however, reduced the background significantly and improved the contrast ratio of the longitudinal intensity to the background by a factor of 7 or 8:1. Much of this background is probably due to Raman scattering.

Another material that exhibits somewhat similar elastic properties to γ -oxygen and cyclooctane I is succinonitrile, introduced earlier in Chapter 1. Ultrasonic measurements in succinonitrile have indicated a high degree of elastic isotropy near the triple point with respect to sound propagation at GHz frequencies [38], and a low value of 0.2 for the Cauchy ratio although the ratios of V_L/V_T are not as large being

2.80, 2.60, 2.77 and 2.55 for different symmetry directions corresponding to those of Table 6.3. Dielectric studies in succinonitrile have indicated very little change in the nature of molecular reorientation between the liquid and the plastic phase [37]. RT coupling is strong enough to give a resonance lineshape to the transverse acoustic mode in succinonitrile. A theoretical model describing the coupling between the reorientational motion and the acoustic phonons is in excellent agreement with the observed experimental data and correctly reproduces the ultrasonic values of the elastic constants of succinonitrile [41]. A depolarized background was also present in the Brillouin spectra of succinonitrile whose origin was considered unknown [117] [38] [39]. This background is probably due to the rotational motion of the molecules.

A distinguishing feature of the Brillouin spectra of γ -oxygen which is different from cyclooctane I or succinonitrile is the strong intensity of the transverse acoustic mode. The intensity ratio I_L/I_T for cyclooctane varies from 0.02 to 0.07 at the triple point to 0.07 to 0.23 at 234.2 K. In general the intensity of the transverse component decreases with temperature. This ratio is unusually high in γ -O₂ and varies from 0.4 to 1.9 at the triple point to 0.49 to 2.9 near the phase transition at 44.0 K. Such unusual strength in the intensity of the transverse component is also observed in the Brillouin spectra of *KCN* and *NaCN* single crystals but only very close to the phase transition [17]. The authors explained the strong intensity of transverse components by noting that the intensity is given by [8]

$$I = C \frac{P_{44}^2}{C_{44}}$$

where C is a proportionality constant. The decrease in C_{44} as the phase transition is approached resulted in the increasing intensity of the transverse acoustic modes in KCN and $NaCN$. Generally then, a large value of the intensity for the transverse component can be expected in $\gamma-O_2$ due to its small values of C_{44} . The difference in the transverse intensities between γ -oxygen and cyclooctane I is then reflected in the different elasto-optic coefficients as measured by P_{44} . A possibility here is that the molecules on the faces of the cube, which are arranged in the form of long mutually orthogonal chains and are rotating about the $\langle 100 \rangle$ axes, are capable of sustaining strong transverse or soft longitudinal acoustic vibrations independent of the rest of the solid. This effect (and hence the elasto-optic coupling) would be greater in γ -oxygen than cyclooctane I since the molecular weight ratio is 1:4 and is also consistent with isotropic nature of both systems.

Theoretical values of the three Pockel's coefficients can be obtained from a recently developed dipole-induced dipole theory ^[118] for the rare gas solids. For cyclooctane I, the calculated Pockel's coefficients are almost independent of temperature and are: $P_{11} = 0.37, P_{12} = 0.34$ and $P_{44} = 0.09$. Except for P_{44} , these values are in good agreement with those measured and presented in Table 5.14. The theoretical values of the Pockel's coefficients for $\gamma-O_2$ are: $P_{11} = 0.29, P_{12} = 0.28$ and $P_{44} = 0.04$. The large difference between the values of P_{11} and P_{12} in $\gamma-O_2$ as seen in Table 5.7 is particularly noted and represents a significant discrepancy with respect to the rare gas solids.

6.3 Methane I

RT coupling plays a very important role in the dynamics of solid methane I. It was mentioned in Chapter 2 that the results of Brillouin scattering studies in single crystals of methane near the triple point indicate a soft acoustic T_1 phonon mode in $\langle 110 \rangle$ direction [90]. Molecular dynamics calculations [89] of the elastic constants of methane failed to reproduce the measured values of Rand *et al.* due to neglect of the molecular orientation of methane (i.e. point masses were assumed). Further theoretical calculations which included RT coupling effects in the intermolecular potential of CD_4 resulted in the determination of the elastic constants in good agreement with the Brillouin results [91].

Table 6.5 includes the temperature dependence of the ratios of acoustic velocities V_L/V_T for high symmetry directions of the cubic lattice. It is noted that by 72.8 K, the ratio of V_L/V_{T_1} has dropped by nearly 7% and at 50.9 K, this ratio is almost equal to that of the rare gas solids. RT coupling appears to decrease as the temperature is lowered. This is expected as the rotational motion decreases on approaching the orientational order-disorder phase transition at 20.6 K.

The elastic constants of methane at 72.8 K, 50.9 K, 38.5 K and 25.0 K are comparable to those of argon, krypton, and xenon as shown in Table 6.6. However, decreasing of C_{12} was observed near 25.0 K which might be related to the onset of the phase transition (see Fig. 5.8). It was hoped that the phase transition temperature could be detected by cooling the crystal and looking for possible critical effects near

Table 6.5: Ratios of acoustic velocities in the high symmetry directions of several molecular crystals

	$\langle 100 \rangle$ $V_L/V_{T_2}(=V_L/V_{T_1})$	$\langle 111 \rangle$ $V_L/V_{T_2}(=V_L/V_{T_1})$	$\langle 110 \rangle$ V_L/V_{T_2}	$\langle 110 \rangle$ V_L/V_{T_1}
Rare gas solids				
Ne, Ar, Kr, Xe ^[35]	1.44	2.24	1.65	2.71
SF_6 ^[48]	1.60	2.29	1.76	2.64
$CH_4(90.4\text{ K})$ ^[90]	1.47	2.46	1.70	3.23
$CH_4(72.8\text{ K})$	1.45	2.36	1.67	2.99
$CH_4(50.9\text{ K})$	1.45	2.29	1.66	2.79
$CH_4(38.5\text{ K})$	1.36	2.33	1.61	3.05
$CH_4(25.0\text{ K})$	1.36	2.23	1.59	2.76

Table 6.6: Elastic constants of methane I as a function of temperature along with those of the rare gas solids near their triple points.

	C_{11} (kbar)	C_{12} (kbar)	C_{44} (kbar)
$Ar(82.3\text{ K})$ ^[35]	23.8	15.6	11.2
$Kr(115.6\text{ K})$ ^[35]	26.57	17.25	12.61
$Xe(156\text{ K})$ ^[35]	29.8	19.0	14.8
$CH_4(90.4\text{ K})$ ^[90]	19.57	14.46	9.20
$CH_4(72.8\text{ K})$	23.58	16.60	11.23
$CH_4(50.9\text{ K})$	27.28	18.14	12.90
$CH_4(38.5\text{ K})$	28.75	20.15	15.48
$CH_4(25.0\text{ K})$	30.40	19.57	16.41

the order-disorder phase transition. However, no noticeable increase in the intensity of scattered light characteristic of critical opalescence was observed. The adiabatic bulk modulus at 72.8 K was 18.93 kbar and agrees well with the value of 18.3 kbar at 77 K from the compressibility measurements [119].

In the present work the results of the temperature dependence of elastic constants for one sample were quite inconsistent (C_{11} and $C_{12} \sim 5\%$ lower and $C_{44} \sim 4\%$ higher) with the results presented in Section 5.4. This could be due to spin conversion effects. It must be noted that methane exhibits three spin species corresponding to the nuclear spin $I = 2, I = 1, I = 0$ labeled as A, T, E species [1]. NMR studies of the spin lattice relaxation time in the plastic phase of methane revealed interesting results [120]. It was found that this relaxation time can be different depending on the history of the sample. If the sample is cooled very quickly from 77 K to 50 K, the spin lattice relaxation time was about two orders of magnitude smaller than if the cooling was done very slow. The authors concluded that the differences observed in the relaxation times is related to the rate at which the sample is cooled down from 77 K to 50 K, and that the fast cooling might produce a higher structural disorder than in the case of slow cooling. The time to equilibrate at a particular temperature on cooling is clearly important. It is suspected that the inconsistency in the elastic constants for the particular sample in question may be related to the rate at which the various samples were cooled, the time allowed between each cooling process and hence the rate of spin conversion.

As noted above, the importance of RT coupling in the dynamics of CD_4 has been theoretically and experimentally demonstrated. The elastic constants for CD_4 have been determined by various techniques at different temperatures. A summary of the results are presented in Table 6.7. The elastic constants of the phase I determined

Table 6.7: Elastic constants of CD_4 determined by various theoretical and experimental techniques

	C_{11} (kbar)	C_{12} (kbar)	C_{44} (kbar)
CD_4 I(89.2 K) ^[90]	20.04	15.00	9.15
CD_4 I(85.57 K) ^[121]	20.56	15.42	9.39
CD_4 I(85.57 K) ^[91]	20.97	15.22	11.32
CD_4 I(32.5 K) ^[90]	27.0	19.2	14.0
CD_4 I(32.5 K) ^[88]	30.8	21.4	15.8
CD_4 II(22.8K) ^[88]	34.6	23.9	16.9

by Brillouin scattering experiment at the triple point^[90] are consistent with the ultrasonic results at 10 MHz^[121]. Elastic constants extrapolated to 32.5 K from the Brillouin spectroscopic results^[90] are however inconsistent with the neutron scattering results^[88] at the same temperature. It should be recognized that Brillouin spectroscopy determines the first-sound elastic constants whereas neutron scattering determines the zero-sound elastic constants which are generally not similar^[53]. The neutron scattering studies indicated no dramatic change in the low frequency phonons between phases I and II. The elastic constants seem to show no anomaly in both phases near the phase transition. The errors associated with the neutron measurements are,

however, about 10%. The anomaly observed in the value of C_{12} as the phase transition temperature in CH_4 is approached is apparently not evident in the above mentioned neutron scattering studies of CD_4 . Further studies on the behaviour of the elastic constants near the phase transition in CH_4 and CD_4 are needed.

The theoretical values of the Pockel's coefficients are ^[118]: $P_{11} = 0.32, P_{12} = 0.30$ and $P_{44} = 0.06$. The agreement with the experimental values (Table 5.20) is noted particularly near 50.9 K (and lower) where RT coupling effects are becoming less significant and methane single crystals begin to behave like rare gas solids near the $q = 0$ regime.

6.4 Concluding remarks

Studies of acoustic properties of van der Waals solids, particularly close to their order-disorder phase transition temperatures have not previously been performed due to difficulties in cooling such single crystals. The present work makes the first systematic attempt to cool simple single molecular crystals of CO , O_2 , and CH_4 (and C_8H_{16}) consistently and successfully and determine their elastic constants (and elastooptic coefficients).

The behaviour of acoustic phonons was probed as the order-disorder phase transition temperatures were approached. No anomaly in the elastic constants indicative of RT coupling was observed in $\alpha-CO$ in the $q = 0$ wavevector regime and the $\alpha-CO$ single crystals effectively behaved like a rare gas solid in this regime.

The Brillouin spectrum of $\gamma-O_2$ was unique in that it exhibited almost exact elas-

tic isotropy (at the triple point) and the transverse components were very intense. Magnetic field studies showed that this was not due to magnetic coupling effects. γ -oxygen (and cyclooctane I) showed significant softening in the transverse acoustic velocity as the phase transition temperature was approached i.e. the transverse (T_1) acoustic velocity was found to decrease in both the $\langle 110 \rangle$ and $\langle 111 \rangle$ directions. Cyclooctane I was studied since it had the same structure as γ -oxygen and RT coupling was known to be strong in this solid. Cyclooctane I was also quite isotropic with respect to the propagation of hypersonic waves. Comparison of γ -oxygen and cyclooctane I, therefore, provides the explanation of the unique Brillouin spectrum of γ - O_2 and indicated that these features are associated with strong RT coupling.

The results for methane I indicated significant RT coupling effect near the triple point and that they become less dominant as the sample is cooled. Further studies are needed to understand the elastic behaviour of methane I and possible spin conversion effects associated with fast cooling between 70 K and 50 K and possible critical effects associated with the phase transitions. A comparative study of the temperature dependence of the elastic constants of CD_4 as compared to CH_4 is in process in this laboratory.

Bibliography

- [1] N. G. Parsonage and L. A. K. Staveley, *Disorder in Crystals* (Clarendon, Oxford, 1978).
- [2] L. A. K. Staveley, *J. Phys. Chem. Solids* **18**, 46 (1961).
- [3] J. N. Sherwood, *The plastically crystalline state* (Chichester:Wiley, 1979).
- [4] J. Timmermans, *J. Phys. Chem. Solids* **18**, 1 (1961).
- [5] K. H. Michel and J. M. Rowe, *Phys. Rev* **B32**, 5818 (1985).
- [6] P. F. Fracassi and M. L. Klein, *Chem. Phys. Lett.* **108**,359 (1984).
- [7] S. M. Rytov, *Sov. Phys. JETP* **6**,130,401,513 (1958).
- [8] I. L. Fabelinskii, *Molecular scattering of light* (Plenum, NewYork, 1968).
- [9] G. I. A. Stegeman and B. P. Stoicheff, *Phys. Rev.* **A7**, 1160 (1973).
- [10] K. H. Michel and J. Naudts, *Phys. Rev. Lett.* **39**,212 (1977).
- [11] K. H. Michel and J. Naudts, *J. Chem. Phys.* **67**,547 (1977).
- [12] K. H. Michel and J. Naudts, *J. Chem. Phys.* **68**, 216 (1978).

- [13] J. C. Raich and R. D. Etters, *J. Chem. Phys.* **55**, 3901 (1971).
- [14] W. Krasser, U. Buchenan and S. Haussuhl, *Solid State comm.* **18**, 287 (1976).
- [15] J. M. Rowe, J.J. Rish, N. Vagelatos, D. L. Price, D. G. Hinks and S. Susman, *J. Chem. Phys.* **62**,4551 (1975).
- [16] S. Haussuhl, *Solid State Comm.* **13**, 147 (1973).
- [17] C. H. Wang and S. K. Satija, *J. Chem. Phys.* **67**, 851 (1977).
- [18] C. J. Bradley and A. P. Cracknel, *The mathematical theory of symmetry in solids* (Clarendon, Oxford 1972).
- [19] R. M. Lynden-Bell, I. R. McDonald and M. L. Klein, *Mol. Phys.* **48**,1093 (1983).
- [20] M. T. Dove, *Orientalional disorder in crystals* **6**, 6 (1987).
- [21] M. T. Dove and R. M. Lynden-Bell, in *Dynamics of molecular crystals*, J. Lascombe, Ed. (Elsevier, Amsterdam 1987).
- [22] J. O. Fossum, C. W. Garland and A. Wells, *Orientalional disorder in crystals* **6**, 14 (1987).
- [23] Y. Yamada, H. Takatera and D. Huber, *J. Phys. Soc. Japan* **36**, 641 (1974).
- [24] C. H. Wang, *J. Chem Phys.* **70**, 3796 (1979).
- [25] D. Sahu and S. D. Mahanti, *Phys. Rev* **B26**, 2981 (1982).

- [26] A. Huller and J. C. Raich, *J. Chem. Phys.* **77**, 2038 (1982).
- [27] J. C. Raich, H. Yasuda and E. R. Bernstein, *J. Chem. Phys.* **78**, 6209 (1983).
- [28] A. Yoshihara, W. D. Wilber, E. R. Bernstein and J. C. Raich, *J. Chem. Phys.* **76**, 2064 (1982).
- [29] G. F. Gignorini, P. F. Fracassi, R. Righini and R. G. Della Valle, *Chem. Phys.* **100**, 315 (1985).
- [30] V. V. Goldman and M. L. Klein, *J. Chem. Phys.* **64**, 5121 (1976).
- [31] H. Kiefte and M. J. Clouter, *J. Chem. Phys.* **64**, 1816 (1976).
- [32] V. Askarpour, H. Kiefte and M. J. Clouter, *Can. J. Chem.* **66**, 541 (1988).
- [33] P. H. Gammon, H. Kiefte and M. J. Clouter, *J. Chem. Phys.* **70**, 810 (1979).
- [34] S. F. Ahmad, H. Kiefte, M. J. Clouter and M. D. Whitmore, *Phys. Rev.* **B26**, 4239 (1982).
- [35] B. P. Stoicheff, in *Rare gas solids Vol II*, M. L. Kein and J. A. Venables Ed. (Academic, London 1976).
- [36] A. P. Jansen, W. J. Briels and A. van der Avoird, *J. Chem. Phys.* **81**, 3648 (1984). A. van der Avoird, W. J. Briels and A. P. Jansen, *J. Chem. Phys.* **81**, 3658 (1984). W. J. Briels, A. P. Jansen and A. van der Avoird, *J. Chem. Phys.* **81**, 4118 (1984).

- [37] D. E. Williams and C. P. Smyth, *J. Am. Chem. Soc.* **84**, 1808 (1962).
- [38] M. J. Bird, D. A. Jackson and H. T. A. Pentecost, in *Proc. 2nd Int. Conf. on Light Scattering in Solids*, M. Balkanski, Ed. (Flammarion, Paris, 1971).
- [39] L. Boyer, R. Vacher, M. Adam and L. Cecchi, in *Proc. 2nd Int. Conf. on Light Scattering in Solids*, M. Balkanski, Ed. (Flammarion, Paris, 1971).
- [40] T. Bischofberger and E. Courtens, *Phys. Rev. Lett.* **35**, 1451 (1975).
- [41] E. Courtens, *J. Phys. (Paris)* **37**, L-21 (1976).
- [42] M. More, J. Lefebvre and R. Fouret, *Acta Crystallogr.* **A33**, 3862 (1977).
- [43] G. Dolling, B. M. Powell and V. F. Sears, *Mol. Phys.* **37**, 1859 (1979).
- [44] M. More and R. Fouret, *Discuss. Faraday Soc.* **69**, 75 (1980).
- [45] M. T. Dove and R. M. Lynden-Bell, *J. Phys.* **C19**, 3343 (1986).
- [46] J. Zuk, D. M. Brake, H. Kiefte and M. J. Clouter, *J. Chem. Phys.* **91**, 5285 (1989).
- [47] J. Zuk, H. Kiefte and M. J. Clouter, *J. Chem. Phys.* **92** (1990).
- [48] H. Kiefte, R. Penney and M. J. Clouter, *J. Chem. Phys.* **88**, 5846 (1988).
- [49] R. Rudman and B. Post, *Science* **154**, 1009 (1966).
- [50] I. R. McDonald, D. G. Bounds and M. L. Klein, *Mol. Phys.* **45**, 521 (1982).

- [51] M. T. Dove, G. S. Pawley, G. Dolling and B. M. Powell, *Mol. Phys.* **57**, 865 (1986). M. T. Dove and G. S. Pawley, *J. Phys.* **C16**, 5969 (1983). M. T. Dove and G. S. Pawley, *J. Phys.* **C17**, 6581 (1984).
- [52] N. Rich, M. J. Clouter, H. Kiefte and S. F. Ahmad, *Bull. Amer. Phys. Soc.* **27**, 633 (1982).
- [53] M. L. Klein and J. A. Venables, *Rare gas solids, Vol. I and II* (Academic, London 1976).
- [54] R. L. Mills, B. Olinger and D. T. Cromer, *J. Chem. Phys.* **84**, 2837 (1986).
- [55] E. Fukushima, A. A. V. Gibson and T. A. Scott, *J. Low Temp. Phys.* **28**, 157 (1977).
- [56] W. E. Streib, T. H. Jordan, H. W. Smith and W. N. Lipscomb, *J. Chem. Phys.* **41**, 756 (1964).
- [57] A. Anderson, T. S. Sun and M. C. A. Dunkersloot, *Can. J. Phys.* **48**, 2265 (1970).
- [58] L. H. Bolz, M. E. Boyd, F. A. Mauer and H. B. Peiser, *Acta Crystallog.* **12**, 247 (1959).
- [59] J. A. Venables and C. A. English, *Acta Crystallog.* **B30**, 929 (1974).
- [60] A. I. Katz, D. Schiferl and R. L. Mills, *J. Phys. Chem.* **88**, 3176 (1984).
- [61] B. O. Hall and H. M. James, *Phys. Rev* **B13**, 3590 (1976).

- [62] V. V. Nauchitel and I. B. Golovanov, *Sov. Phys. Cryst.* **30**, 27 (1985).
- [63] J. J. Weis and M. L. Klein, *J. Chem. Phys.* **63**, 2869 (1975).
- [64] O. Schnepp and A. Ron, *Disc. Farad. Soc.* **48**,26, (1969).
- [65] H. Kiefte and M. J. Clouter, *J. Chem. Phys.* **62**, 4780 (1975).
- [66] Bart Olinger, R. L. Mills and R. B. Roof, Jr., *J. Chem. Phys.* **81**, 5068 (1984).
- [67] T. H. Jordan, W. E. Streib, H. W. Smith and W. N. Lipscomb, *Acta Crystallogr.* **17**, 777 (1964).
- [68] J. E. Cahill and G. E. Leroi, *J. Chem. Phys.* **51**, 97 (1969).
- [69] H. Kiefte, M. J. Clouter, N. H. Rich and S. F. Ahmad, *Chem. Phys. Lett.* **70**, 425 (1980).
- [70] M. L. Klein, D. Levesque and J. J. Weis, *Phys. Rev* **B21**, 5785 (1980).
- [71] K. Kobashi, M. L. Klein and V. Chandrasekharan, *J. Chem. Phys.* **71**, 843 (1979).
- [72] A. P. J. Jansen and A. van der Avoird, *J. Chem. Phys.* **86**, 3597 (1987).
- [73] G. DeFotis, *Phys. Rev.* **B23**, 4714 (1981).
- [74] R. C. Keller, M. S. Coffey, M. J. Lizak and M. S. Conradi, *J. Phys. Chem.* **93**, 3832 (1989).

- [75] M. J. Lizak, R. C. Keller, M. S. Coffey and M. S. Conradi, *J. Phys. Chem.* **94**, 992 (1990).
- [76] H. L. Finke, D. W. Scott, M. E. Gross, J. F. Messerly and G. Waddington, *J. Am. Chem. Soc.* **78**, 5469 (1956).
- [77] D. E. Sands and V. W. Day, *Acta Crystallogr.* **19**, 278 (1965).
- [78] Y. Huang, I. S. Butler and D. F. R. Gilson, Unpublished results.
- [79] R. Rudman and B. Post, *Mol. Cryst.* **3**, 325 (1968).
- [80] W. Press, *J. Chem. Phys.* **56**, 2597 (1972).
- [81] J. H. Colwell, E. K. Gill and J.A. Morrison, *J. Chem. Phys.* **39**, 635 (1963).
- [82] H. M. James and T. A. Keenan, *J. Chem. Phys.* **31**, 12 (1959).
- [83] W. Press and A. Kollmar, *Solid State Commun.* **17**, 405 (1975).
- [84] M. Bloom and J. A. Morrison, *Surface and defect properties of solids, Vol. II.*
- [85] M. Sprik and M. L. Klein, *J. Chem. Phys.* **80**, 1988 (1984).
- [86] R. Savoie and R. P. Fournier, *Chem. Phys. Lett.* **7**, 1 (1970).
- [87] M. Blumenfeld, *Natl. Bur. Stand. spec. publ.* **301**, 441 (1969).
- [88] W. G. Stirling, W. Press and H. Stiller, *J. Phys.* **C10**, 3959 (1977).
- [89] D. G. Bounds, M. L. Klein and G. N. Patey, *J. Chem. Phys.* **72**, 5348 (1980).

- [90] S. C. Rand and B. P. Stoicheff, *Can. J. Phys.* **60**, 287 (1982).
- [91] S. Wonneberger and A. Huller, *Z. Phys.* **B66**, 191 (1987).
- [92] A. Huller and W. Press, *Phys. Rev. Lett.* **29**, 266 (1972).
- [93] L. D. Landau and E. M. Lifshitz, *Theory of elasticity* (Pergamon, Oxford 1970).
- [94] G. B. Benedek and K. Fritsch, *Phys. Rev.* **149**, 647 (1966).
- [95] J. F. Nye, *Physical properties of crystals* (Clarendon, Oxford 1957).
- [96] W. Hayes and R. Loudon, *Scattering of light by crystals* (Wiley, New York 1978).
- [97] H. Goldstein, *Classical Mechanics* (Addison-Wesley, Cambridge 1950).
- [98] P. Jacquinet, *Rep. Prog. Phys.* **23**, 267 (1960).
- [99] J. R. Sandercock, in *Proc. 2nd int. conf. on light scattering in solids*, M. Balkanski Ed. (Paris 1971).
- [100] I. E. Morgan, M. Sc. Thesis, Memorial University of Newfoundland, St. John's Newfoundland 1976 (Unpublished).
- [101] Burleigh Instruments Inc. Tech. Memo for Fabry-Perot Interferometry, No. FP140475.
- [102] S. F. Ahmad, Ph. D. Thesis, Memorial University of Newfoundland, St. John's Newfoundland 1980 (Unpublished).

- [103] H. Kiefte, S. W. Breckon, R. Penney and M. J. Clouter, *J. Chem. Phys.* **83**, 4738 (1985).
- [104] J. C. Brice, *The growth of crystals from the melt* (North-Holland, Amsterdam 1965).
- [105] P. H. Gammon, M. Sc. Thesis, Memorial University of Newfoundland, St. John's Newfoundland 1978 (Unpublished).
- [106] B. D. Cullity, *Elements of X-ray diffraction* (Addison-Wesley, Ma. 1967).
- [107] R. A. McLaren, Ph. D. Thesis, University of Toronto 1974 (Unpublished).
- [108] I. N. Krupskii, A. I. Prokhvatilov, A. I. Erenburg and L. D. Yantsevich, *Phys. Status Solidi* **A19**, 519 (1973).
- [109] C. S. Barrett, L. Meyer and J. Wasserman, *Phys. Rev.* **163**, 851 (1967).
- [110] D. W. Oxtoby and V. Chandrasekaran, *Phys. Rev.* **B16**, 1706 (1977).
- [111] A. F. Prikhotko, Y. G. Pikus and L. I. Shanskii, *Opt. Spectrosc.* **54**, 277 (1983).
- [112] A. M. Tolkachev and V. G. Manzhelii, *Sov. Phys. Solid State* **5**, 2506 (1964) **7**, 1711 (1966).
- [113] S. Gewurtz and B. P. Stoicheff, *Phys. Rev.* **B10**, 3487 (1974).
- [114] J. K. Kjems and G. Dolling, *Phys. Rev.* **B11**, 1639 (1975).
- [115] B. M. Powell and G. S. Pawley, *J. Chem. Phys.* **91**, 7877 (1989).

- [116] R. S. Krishnan in *The Raman Effect Vol. I*, A. Anderson, Ed. (New York, 1971).
- [117] M. Adam, L. Boyer, R. Vacher, P. Berge and L. Cecchi J. de Phys. **32** C5a, 233 (1971).
- [118] V. Mazzacurati, G. Signorelli and G. Ruocco Europhys. Lett. **2**, 877 (1986).
- [119] J. W. Stewart, J. Phys. Chem. Solids **12**, 122 (1959).
- [120] G. Briganti, P. Calvani F. De Luca and B. Maraviglia, Can. J. Phys. **56**, 1182 (1978).
- [121] S. V. Marx and R. O. Simmons, J. Chem. Phys. **81**, 944 (1984).

